

Designer Heterogeneous Nano-Catalysts Using Covalent Organic Frameworks

A Thesis

Submitted in Partial Fulfillment of the Requirements

for the Degree of

Doctor of Philosophy

By

Mullangi Dinesh

ID: 20143296



Indian Institute of Science Education and Research (IISER), Pune 2019

Dedicated to

My family



भारतीय विज्ञान शिक्षा एवं अनुसंधान संस्थान, पुणे
INDIAN INSTITUTE OF SCIENCE EDUCATION AND RESEARCH (IISER), PUNE
(An Autonomous Institution, Ministry of Human Resource Development, Govt. of India)
Dr. Homi Bhabha Road, Pune – 411 008

Dr. R. Vaidhyanathan
Associate Professor

Certificate

This is to certify that the work incorporated in the thesis entitled “*Designer Heterogeneous Nano-Catalysts Using Covalent Organic Frameworks*” submitted by **Mullangi Dinesh** has been carried out by the candidate at the Indian Institute of Science Education and Research (IISER), Pune, under my supervision. The work presented here or any part of it has not been included in any other thesis submitted previously for the award of any degree or diploma from any other University or Institution.

Date:

Dr. R. Vaidhyanathan
(Thesis Supervisor)

Declaration

I declare that this written submission represents my ideas in my own words and where others' ideas have been included; I have adequately cited and referenced the original sources. I also declare that I have adhered to all principles of academic honesty and integrity and have not misrepresented or fabricated or falsified any idea/data/fact/source in my submission. I understand that violation of the above will be cause for disciplinary action by the Institute and can also evoke penal action from the sources which have thus not been properly cited or from whom proper permission has not been taken when needed.

Date:

Mullangi Dinesh

Roll No. 20143296

Acknowledgments

I, with deep sense of gratitude, wish to express my thanks to my research supervisor Dr. R. Vaidhyanathan, for his generous support and giving me the opportunity to fulfill the dream of pursuing doctoral studies at IISER-Pune. I'm thankful to him for the unlimited time and efforts that he has extended to me, analyzing and solving the problems which I have faced, without his support and enthusiasm this journey would have been an extremely difficult one for me. I'm glad to say under your guidance I have acquired not only how to complete scientific projects thoroughly, but also learned how to present and communicate them effectively to international standards. Working under your supervision has been very enjoyable and one of the great journeys in my life. I sincerely thank you for being such a wonderful mentor, I feel fortunate to have him as my supervisor. I thank Indian Institute of Science Education and Research (IISER), Pune and the director Prof. Jayant B. Udgaonkar and former Director Prof. K. N. Ganesh for providing excellent research facilities and an amazing and an outstanding research atmosphere. I am extremely thankful to SERB and Infosys for their travel support to attend the conferences.

I am also grateful to the Research Advisory Committee members Dr. R. Boomishankar (IISER-Pune) and Dr. C.P. Vinod (NCL-Pune) for their valuable suggestions and advice. I am also thankful to my collaborators Dr. Sreekumar Kurungot (CSIR-NCL Pune), Dr. C.P. Vinod, (CSIR-NCL Pune), Dr. Tom Woo, (University of Ottawa Canada), Dr. Sunil Nair, (IISER Pune), Dr. Samir Chikkali (CSIR-NCL Pune) for their research inputs. I am extremely grateful to all the faculty members of IISER Pune and the chair of the Chemistry Department for their kind assistance.

I thank my lab mates Aparna, Debanjan, Himan, Pragalb, Rahul, Rinku, Sattwick, Shalini, Shyama, and Vamshi, for their help. I would also like to acknowledge project fellows (IISER- BS-MS) Datta, Anu, Anita, Bhavin, and Nidhi. I am thankful to Dr. Gopala Krishna, Dr. Kiran Reddy, Dr. Channa Reddy, Subhramanyam from IISER-Pune and Dr. Vishal M. Dhavale, Dr. Vijay, Dr. Santosh K. Singh, from CSIR-NCL Pune for carrying out some of the measurements for my projects.

I am grateful to my first research supervisor Dr. Swadhin K Mandal (Associate Professor, IISER-Kolkata), the careful supervision of whom had given me an impeccable research exposure during my M.Sc. days, in the IAS summer research fellowship program, 2011. It was in his

group that I got the first taste for experimental chemistry and catalysis. I am also grateful to Dr. Sujith. K Ghosh (Associate Professor, IISER-Pune), for the opportunity given to work in his group as a project fellow in his group I had great exposure on porous materials and developed many skills.

I thank Dr. Umeshareddy Kacherki (deputy librarian) and Anuradha for library support and all other technical staff (Mr. Parveen Nasa, Ms. Archana, Mr. Yathish, Mr. Sandeep, Mrs. Megha Mr. Nilesh Dumbre, Ms. Nayana, Mr. Nitin, Mr. Anil, Mr. Mahesh, Mr. Neeraj Maheshwari, to name a few), as well as all the IISER Pune non-teaching staff members, especially Mr. Mayuresh, Mr. Tushar, Ms. Nayana, Ms. Vrushali, Mr. Suresh, Mr. Prabhas, Mr. Sandeep, Ms. Mariamma John, for their generous support at a number of times. I thank Ms. Neeta Deo, Mr. Suresh, Mr. Sachin and Mr. Sailesh for IT support. I thank all my friends and colleagues at IISER Pune for making my stay comfortable and memorable.

No words can ever convey my sense of gratitude felt for my parents, adopted parents, brothers, sister and their families for selfless love and support throughout my career. It wouldn't have been possible for me to achieve all that without their support. It is to them that I dedicate this work. Finally, I would be signing off by thanking all of the amazing teachers who have directly or indirectly helped me along the way. Good teachers are the reason why ordinary students dream to do extraordinary things. Thank you.

-Mullangi Dinesh

Table of contents

Synopsis.....	vii
List of Acronyms.....	xii
Research Publications.....	xiii
Patents.....	xiv

1. Use of covalent organic frameworks in the development of heterogeneous nanocatalysts

1.1. Catalysis.....	2
1.1.1 Homogeneous catalysis.....	3
1.1.2 Heterogeneous catalysis.....	3
1.1.3 Nanocatalysis	3
1.1.3.1. Capping-agent stabilized nanocatalysis.....	3
1.1.3.2. Porous materials supported nanocatalysis.....	5
1.2. Choices of porous materials for nanocatalysis-a brief introduction.....	6
1.3. Covalent organic frameworks and its advantages in nanocatalysis.....	7
1.4. Covalent organic frameworks supported nanocatalysis-recent literature.....	9
1.5. References.....	21

2. Synthesis and catalytic studies of Pd(0) loaded N-rich triazine COF for multi-fold Heck couplings, Suzuki couplings and CO oxidation reactions

2.1. Introduction	26
2.2. Experimental details	27
2.2.1 Materials and measurements.....	27
2.2.2 Synthesis of trialdehyde monomer.....	28
2.2.3. Synthesis of IISERP-COF1.....	28
2.2.4. Synthesis of Pd@IISERP-COF1	29
2.2.5. General procedure for the Heck reaction.....	30
2.2.6. General procedure for the Ullmann type homo (C-C) coupling reaction.....	31
2.2.7. General procedure for the Suzuki coupling reaction.....	31
2.2.8. CO to CO ₂ oxidation experimental conditions.....	31
2.3. Structure solution and description	32
2.4. Results and discussion	34
2.5. Catalytic studies of Pd@IISERP-COF1 catalyst	37
2.5.1. Suzuki-Miyaura coupling.....	37

Table of contents

2.5.2. Heck coupling.....	37
2.5.3 Multi-fold Heck coupling.....	38
2.5.4 CO Oxidation reaction	40
2.5.5 Recyclability and durability studies.....	40
2.6. Summary	43
2.7. References	44
2.8. Appendix	46
3. Enhancing the stability of Schiff-bonded COF for use as support for catalytic cobalt nanoparticles and their activity in releasing H₂ gas from solid hydride sources under harsh aqueous conditions and the in-situ reduction of C≡N/NO₂ to amines	
3.1. Introduction	49
3.2. Experimental details	51
2.2.1 Materials and Measurements.....	51
2.2.2 Synthesis of ligands.....	52
2.2.3. Synthesis of IISERP-COF5.....	53
2.2.4. Synthesis of Co@IISERP-COF5 composite.....	54
2.2.5. General procedure for catalytic H ₂ evolution from chemical hydrides	56
2.2.6. General procedure for the nitrile compounds reduction reactions	57
2.2.7. General procedure for the nitro compounds reduction reactions.....	58
3.3. Structure solution and description	59
3.4. Results and discussion	59
3.5. Catalytic studies of Co@IISERP-COF5	65
2.5.1. Hydrogen evolution from chemical hydrides.	65
2.5.2. Hydrogenation of nitro compounds	66
2.5.3 Hydrogenation of cyano compounds	67
2.5.4 Recyclability and durability studies.....	68
3.6. Computational modeling	69
3.7. Summary	72
3.8. References	72
3.9. Appendix	75

4. Low-overpotential electrocatalytic water splitting with noble-metal-free nanoparticles supported in an sp^3 N-rich flexible COF

4.1. Introduction	80
4.2. Experimental details	80
4.4.1 Materials and measurements.....	80
4.4.2 Synthesis of ligand.....	81
4.4.3. Synthesis of IISERP-COF2.....	82
4.4.4. Synthesis of homometallic $Co_x(OH)_2$ or $Ni_y(OH)_2@IISERP-COF2$ composite...	83
4.4.5. Synthesis of heterometallic $Co_x(OH)_2Ni_y(OH)_2@IISERP-COF2$ composite.....	84
4.4.6. General procedure for the electrochemical studies.....	86
4.3. Structure solution and description	87
4.4. Results and discussion	89
4.5. Electrochemical studies	96
4.6. Computational modeling	99
4.7. Summary	99
4.8. References	100
4.9. Appendix	103
5.0. Copyrights	104

In recent years, research on nanocatalyst development has surged due to the fundamental understanding that at nano-dimensions the catalysts tend to exhibit high surface area resulting in excellent activity enhancement. Another, important task in catalysis has been on developing stable, durable solid-state catalysts (heterogeneous) that can replace the homogeneous catalysts. Such solid-state catalysts would bring advantage in terms of ease of separation, recyclability and scalability. However, imparting high catalytic activity comparable to the homogeneous catalysts is challenging. This is where engineering the catalysts to nano-dimensions serves as an excellent approach. Metals and metal-based compounds represent a large class of stable catalyst for a variety of chemical reactions. It is well-established that their catalytic activity can be tuned by manipulating their size and shapes, which is typically achieved by the utilization of suitable capping agents. Unfortunately, these capping agents which stabilize the nanoparticles (nps) bring a negative contribution by diminishing the accessibility to the nanoparticle surfaces and if they are removed, the nanoparticles tend to aggregate. To overcome this, as an alternate approach the catalytic nps can be grown on high surface area porous supports- "capping-agent free" method. This is a prominent way to synthesize specific sized metal nanoparticles (nano-confined) and they inherently form as homogenous dispersions. However, the stability, durability and compatibility of the porous support embedded with the nps under harsh reaction conditions pose a severe challenge. Therefore synthesis of stable and novel functional organic supports for nps construction is highly desired.

Chapter 1: Use of Covalent Organic Frameworks in the Development of Heterogeneous Nanocatalysts

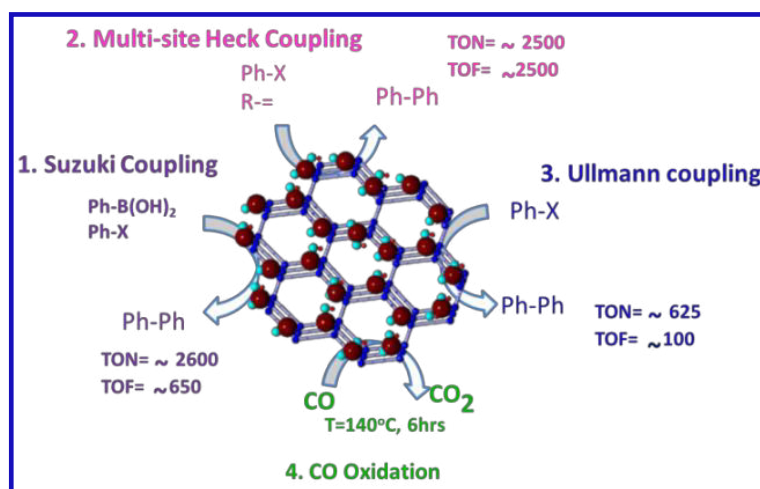
Covalent organic frameworks (COFs) are a new class of ordered crystalline porous organic polymers that can serve as an excellent porous host for growing small uncapped nanoparticles. The major advantages of COFs are its designable modular architectures and pores. The functional tunability and uniform pores make COFs as admirable support for growing nanoparticles of metal with controlled sizes. The reversible nature of Schiff bonds are known to hydrolyze under basic media, thus constructing stable COFs under strong acidic/basic conditions is a major challenge. Additionally, nanoparticle leaching, durability and compatibility of COF with nps are other key challenges for the reusable heterogeneous catalyst. The main objective of my Ph. D. work is the synthesis of stable basic pyridyl N- rich COFs for selective heterogeneous nanocatalysis. In Chapter 1, an introduction is provided to the different class of porous supports

Synopsis

used for growing catalytic nanoparticles. Then a special emphasis is given to the literature on COF-nanoparticle composites used in catalysis.

Chapter 2: Synthesis and Catalytic Studies of Pd(0) loaded N-rich Triazine COF for Multi-fold Heck Couplings, Suzuki Couplings and CO Oxidation Reactions

Suzuki and Heck cross-coupling reactions are powerful synthetic tools to create new C-C bonds. But till date, most (> 90%) of the routine Heck/Suzuki reactions are catalyzed by Pd or palladium compounds. Also, synthesis of industrially useful multi-site Heck coupled products (the products of which can serve as monomer in polymer synthesis or as ligands in coordination polymer or MOF making and even in COF synthesis) is rare and needs exploring. Selectivity and activity of catalysts are key challenges for multi-site coupling reaction as they typically yield multiple products which are quite difficult to isolate.



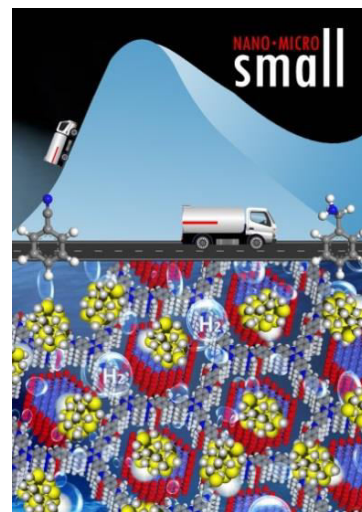
In this chapter, we synthesized a stable nitrogen-rich mesoporous triazine COF, loaded it with Pd(0) nanoparticles (size of nps 5-10nm) via a facile single-step method and studied its catalytic activity for coupling reactions. Just < 0.05 mol% of nano-Pd@IISERP-COF1 gives high activity and excellent selectivity for simultaneous *multiple-site Heck and Suzuki couplings* and homo C-C coupling reactions in the open air with a high TON (up to 2500). Further cycling studies showed their ready recyclability with no sign of catalyst leaching even after 4 consecutive cycles. Also, our Pd@IISERP-COF1 catalyst shows excellent activity for the conversion of poisonous CO to CO₂ (100%) at 150^oC without any loss of activity over 6hrs. The structure was modeled and the experimental PXRD was refined against the model using *Pawley*

Synopsis

refinement techniques and excellent fits were observed for $P6/mcc$ space group ($GOF R_p = 2.64\%$; $wR_p = 3.36\%$), Further dispersion-corrected DFT modeling studies reveal that basic triazine units in the framework are highly active sites to hold Pd(0) nps without leaching. Presence of uniform mesoporous and readily accessible Pd(0) nps in Pd@IISERP-COF1 offers excellent selectivity for multi-site heck coupling products.

Chapter 4: Enhancing the Stability of Schiff-Bonded COF for use as Support for Catalytic Cobalt Nanoparticles and their Activity in Releasing H₂ Gas from Solid Hydride Sources under Harsh Aqueous Conditions and the In-Situ Reduction of C≡N/NO₂ to Amines

Catalytic decomposition of chemical hydrides (NaBH₄, NH₂NH₂ and BH₃NH₃) is another convenient way to obtain clean hydrogen and also a prominent way to store hydrogen at a high volumetric density (up to ~63 g H₂/L). These being solids bring in enormous advantage in the form being a safe and mobile H₂ source. This released H₂ can be used in the synthesis of various organic/drug molecule synthesis. However, the best catalysts capable of releasing hydrogen from these solid hydrides are based on expensive noble metals. Hence, it is imperative to develop cost-effective and stable noble metal-free heterogeneous catalysts.



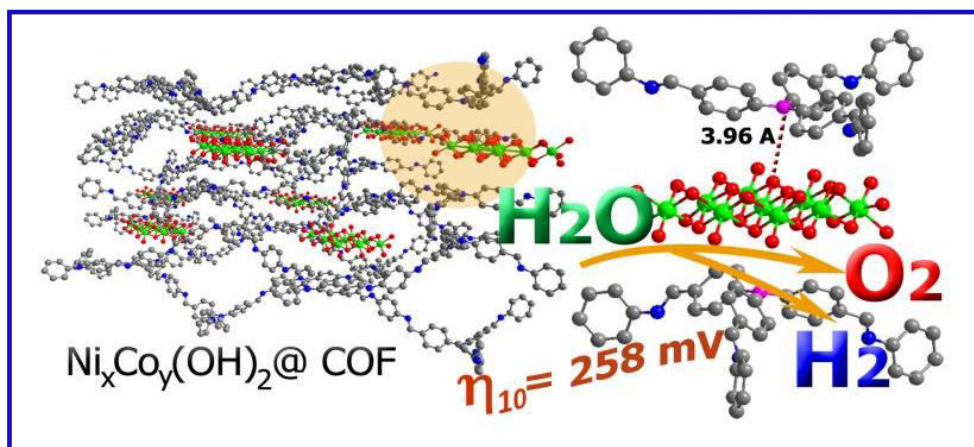
In this work, the COF by choice is built from “methoxy” functionalized dialdehydes which is crucial in enabling the complete retention of the COF structure under the strong reduction conditions of the catalysis, where the regular Schiff bonds would have hydrolyzed. The N-rich binding pockets in the COF ensure strong np-COF interactions and provide high stability to the catalyst without any leaching of the nps. Here, the synthesized Co@IISERP-COF5 composite having about 16 wt% of cobalt (< 6 nm sized) catalysts shows excellent activity for H₂ evolution (releases the theoretical equivalents in < 18 min) from the readily available safe and cheap NaBH₄, NH₂NH₂ and BH₃NH₃ at room temperature. Furthermore, this released H₂ is utilized for the hydrogenation of nitrile (-C≡N) and nitro (-NO₂) compounds to amines under ambient conditions in a facile one-pot reaction. The Co@IISERP-COF5 catalyst shows excellent activity (up to 99% yield) and good selectivity for primary amines over other products. Kinetics studies show that the Co@IISERP-COF5 catalyst has a low activation energy (48 kJ/mol) for H₂

Synopsis

evolution from chemical hydrides. This activation energy is comparable to well-studied noble-metal supported catalysts. The DFT simulation studies reveal the crucial role played by the COF in exposing the active facets and thereby in controlling the activation of the reducing agent.

Chapter 3: Low-overpotential Electrocatalytic Water Splitting with Noble-Metal-Free Nanoparticles Supported in an sp^3 N-Rich Flexible COF

To solve the energy and environmental crisis brought by the huge consumption of fossil fuels, alternative fuels are required. Hydrogen is a clean-burning energy-rich fuel. It is produced in large scales by energy-intensive steam-reformation procedures. Electrocatalytic water splitting offers an alternate energy-efficient approach for hydrogen (H_2) production. The water splitting is a thermodynamically demanding process and requires a catalyst to bring down the potential required for the hydrogen and oxygen evolution reactions. Till date, the highest performing and state-of-the-art catalysts were noble-metal-containing Pt/Ru/Ir catalysts. Cheaper and commercially available non-noble metal electrocatalysts with comparable performance to noble metal catalysts are rare and is in demand.



In this Chapter, we have designed building units with highly flexible tetrahedral sp^3 nitrogen-rich centers; because, the presence of sp^3 nitrogen lone pairs can not only bind strongly to the metal nps but can be expected to give good electronic activity between the nps and COF, which can improve their catalytic performance. The synthesized IISERP-COF2 forms a flexible pseudo-3D lattice structure in $P6_3$ space group. In the optimized structure each framework layer of the COF is buckled and stacked, this generates uniform 20 Å pores. This IISERP-COF2 is loaded with non-noble-metal nanoparticles ($Co_xNi_y(OH)_2$, < 2 nm sized). This

Synopsis

composite has been employed as a catalyst in electrocatalytic Oxygen Evolution Reaction (OER). The optimized nanocomposite (4%Co:12%Ni@IISERP-COF2 β) showed excellent activity for OER from alkaline water with an overpotential of 258 mV at a current density of 10 mAcm⁻². The overpotential observed in the COF-nanoparticle system is the best in class and is close to the current record of ~200 mV for any noble-metal-free electrocatalytic water splitting system the Fe-Co-Ni metal-oxide-film composite. Also, it possesses outstanding kinetics (Tafel slope of 38.9 mV dec⁻¹) reflected in high TOF of 0.186170s⁻¹, which is six-fold higher than Ir/C catalyst. DFT modeling studies reveal that in the optimized configuration of the composite, the Co/Ni(OH)₂ nanosheets are sandwiched between COF layers and are oriented to interact with the sp³ nitrogens of the framework. These interactions could be playing a crucial role in lowering the overpotential with fast kinetics for water oxidation reactions.

List of Acronyms

1	COF: Covalent Organic Frameworks	21	mol: moles
2	PCP : Porous Coordination Polymer	22	K: Kelvin
3	MOF: Metal Organic Framework	23	°C : Degree Celsius
4	CP: Coordination Polymer	24	TOF: Turnover Frequency
5	DFT: Density Functional Theory	25	TON : Turnover Number
6	DMF: N, N-Dimethyl formamide	26	mmol: Milli moles
7	DMSO-D6: Dimethyl Sulphoxide -duterated	27	µL : Micro liter
8	CDCI3: Deuterated Chloroform	28	µm: micrometer
9	O-DBC: Ortho-Dichlorobenzene	29	mL: Milliliter
10	FE-SEM: Field Emission-Scanning Electron	30	nm : nanometer
11	FT-IR: Fourier Transform Infra-red-spectra	31	hrs: hours
12	AFM : Atomic Force Microscopy	32	min: Minutes
13	XPS: X-ray Photoelectron Spectroscopy	33	MHz: Megahertz
14	TGA: Thermogravimetric analysis	34	gm: Gram
15	PXRD: Powder X-Ray Diffraction	35	mg: Milligram
16	BET: Brunauer Emmett Teller	36	Å : Angstrom
17	CD: Circular-Dichroism	37	Anal: Analysis
18	EtOAc : Ethyl acetate	38	Calc: Calculated
19	ACN: Acetonitrile	39	AcOH: Acetic acid
20	HR-TEM: High Resolution-Transmission Electron Microscope		

Included in Thesis:

1. Pd loaded amphiphilic COF as catalyst for multi-fold Heck reactions, C-C couplings and CO oxidation.
Mullangi, D.; Nandi, S.; Shalini, S.; Sreedhala, S.; Vinod, C. P.; Vaidhyanathan, R. *Scientific Reports*. **2015**, 5, 10876.
2. Highly Stable COF-Supported Co/Co(OH)₂ Nanoparticles Heterogeneous Catalyst for Reduction of Nitrile/Nitro Compounds under Mild Conditions.
Mullangi, D .; Dhavale, V.; Shalini, S.; Nandi, S.; Collins, S.; Woo, T.; Kurungot, S.; Vaidhyanathan, R. *Advanced Energy Materials*. **2016**, 1600110.
3. Low-Overpotential Electrocatalytic Water Splitting with Noble-Metal-Free Nanoparticles Supported in a sp³ N-Rich Flexible COF.
Mullangi, D.; Chakraborty, D.; Pradeep, A.; Koshti, V.; Vinod, C.P.; Panja, S, p.; Nair, S.; Vaidhyanathan, R.; *Small* **2018**, 1801233.

Not Included in Thesis:

4. Super-hydrophobic Covalent Organic Frameworks for Chemical Resistant Coatings, Hydrophobic Paper and Textile Composites.
Mullangi, D.; Shalini, S. Nandi, S, Choksi,B. Vaidhyanathan, R. *J. Mater.Chem. A* **2017**, 5, 8376-8384.
5. Highly-Stable COF-Supported Palladium Nanoparticles- A robust Heterogeneous Catalyst for Dehydrogenation of Formic Acid at Room Temperature.
Mullangi, D.; Jain, P; Chakraborty, D.; Rinku, K; Vamsi, K;, Haldar, S.; Vinod, C. P.; Vaidhyanathan, R. *Manuscript Submitted*
6. N-Rich Flexible Chiral Covalent Organic Frameworks for Heterogeneous Asymmetric Catalysis.
Mullangi, D.; Vamsi, K.; Sen, A.; Rinku, K.; Chakraborty, D.; Chikkali, S. H.; Vaidhyanathan, R. *under preparation*
7. Anthracene-Resorcinol Derived Covalent Organic Framework as Flexible White Light Emitter.
Haldar, S.; Debanjan, C.; Roy, B.; Banappanavar, G.; Rinku, R.; **Mullangi, D.**; Hazra, P.; Kabra, D.; Vaidhyanathan, R. *J. Am. Chem. Soc.* **2018**, 140 (41), pp 13367–13374.

8. Low Band Gap Benzimidazole COF Supported Ni₃N as Highly Active OER Catalyst
Nandi, S.; Kumar, S, S.; **Mullangi, D.**; Illathvalappil, R.; George, L; Vinod, C. P.; Kurungot, S.; Vaidhyanathan, R. *Advanced Energy Materials*. **2016**, 61601189.

Patents:

1. Amphiphilic Micro-Mesoporous Covalent Organic Frameworks and its Metal Loaded Phases for C-H Activation and C-C Couplings, and Oxidation of CO
Mullangi, D and Vaidhyanathan R. Patent Appl. No. 2692/MUM/2015, Published on 7/04/2017.
2. Covalent Organic Frameworks as Porous Supports for Non-Noble Metal based Water Splitting Electrocatalysts
Mullangi, D, Nandi.S and Vaidhyanathan.R. (Patent Appl. No. No.4301/MUM/2015).

Chapter-1

Use of Covalent Organic Frameworks in the Development of Heterogeneous Nanocatalysts



1.1. Catalysis

A catalyst is a substance or a compound that participates in the chemical reaction to enhance the rate of the reaction by lowering the activation energy without altering the equilibrium state and thermodynamics of the chemical reaction.¹ An ideal catalyst does not get consumed and gets regenerated to its pristine state at the end of the catalyzed reaction, Hence can be recycled. Typically, only small amounts of catalysts are employed in a reaction. Research in the catalysis has grown exponentially in the last two decades.² Catalysts play vital role in various fields such as drug synthesis, food processing, energy conversion, environmental and automobile applications etc.³ According to *Global Catalyst Market's* report (2014), the global demand on catalysts was US\$34 billion per year and it is expected to grow rapidly in the coming years.⁴ To meet the growth of global market demand and to control the rising raw material prices, many industries and academics are focused on carrying research in the field of nanocatalysis and material science for cheaper bulky scale synthesis. The main aim of modern nanocatalysis is atom-efficiency, step simplification, easy synthesis, cost reduction, long-life, large-scale production, and environment-friendly nature. Therefore, depending on the type of catalyst and reaction medium, catalysis is classified into homogeneous and heterogeneous catalysis.

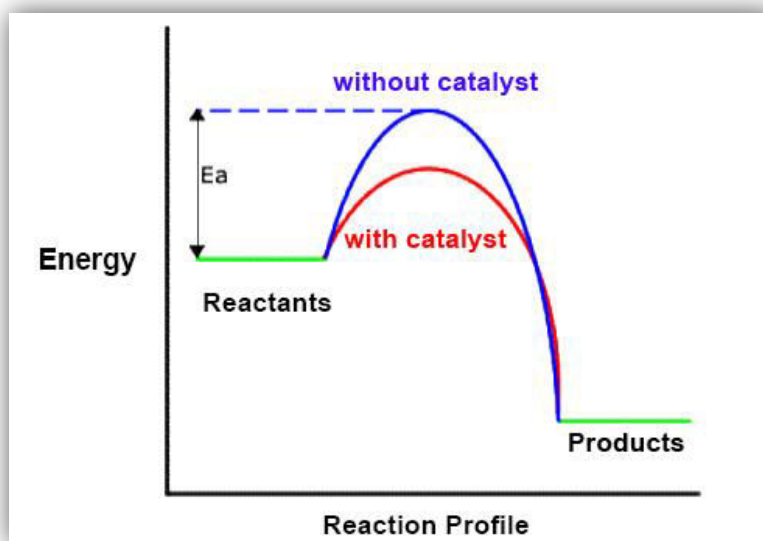


Figure 1. Schematic representation shows the potential energy diagram of the catalytic process and their activation energy profile in the presence and absence of the catalyst.

1.1.1. Homogeneous catalysis

In the homogeneous catalysis, both the reactants and the catalyst are in the same phase (liquid or gas or solid) and thus distributes uniformly in the reaction medium⁵. As a result, the molecular collisions between the reactants and the catalyst takes place easily without any strain. This reaction proceeds with faster kinetics and more efficiency than the typical heterogeneous catalysis^{1,5}. However, separation, complication of handling and regeneration of the catalyst from the reaction medium are the main challenges in the homogenous catalysis. Thus, replacement of homogeneous catalysis with heterogeneous catalysis is highly encouraged for bulk scale industrial applications.

1.1.2. Heterogeneous catalysis

In the heterogeneous catalysis, both the reactants and the catalyst are present in distinct phase or medium^{1, 2} (gas-solid or gas-liquid or liquid-solid etc). Heterogeneous catalysts are more stable and have several advantages over homogeneous counterparts^{1, 6}. In heterogeneous catalysis, a spent catalyst can be effectively and easily recovered by simple filtration or centrifugation and if made into an easy to handle solid form like a membrane, it can even be pulled out of the reaction medium. This recoverability is an important concern for the industrial manufacturing processes. However, the major drawback for the heterogeneous catalysis is poor selectivity, slow kinetics and long reaction time⁶. However, the disadvantages of heterogeneous catalysis are outweighed by its advantages. Moreover, recent reports demonstrate that these difficulties can be addressed by utilizing a new class of heterogeneous nanocatalysts.

1.1.3. Heterogenous Nanocatalysis

1.1.3.1. Capping-agent Stabilized Nanocatalysis

If the catalyst can be rendered with nano dimensions, it enhances its activity due to enhanced surface areas. Reactions that employ such nano-sized catalyst can be termed as nanocatalysis⁷. Developing heterogeneous nanocatalysts could bring all the advantages over homogeneous counterparts as stated above. Metals and metal-based compounds represent a large class of stable catalyst for a variety of chemical reactions. It is well-established that their catalytic activity can be tuned by manipulating their size and shape, which is typically achieved by the utilization of suitable capping agents⁸. Unfortunately, these capping agents which stabilize

the nanoparticles (nps) bring a negative contribution by reducing the accessibility to the nanoparticle surfaces⁹ For example, PVA-protected Pd nanocatalyst¹⁰ prepared by sol immobilization method (capping-agent route) does not show any considerable activity and selectivity for benzaldehyde decarbonylation compared with conventional Pd/Al₂O₃¹⁰. In this system, though the selectivity is high, the activity is low, this is attributed to the blocking of the Pd(111) facets by the PVA capping agent¹⁰.

Typically the following representative capping agents are used in nanoparticle synthesis, such as (i) oleic acid (OA), (ii) oleylamine (OAm), (iii) poly(Nvinyl-2-pyrrolidone) (PVP), (iv) trioctylphosphine (TOP), (v) cetyltrimethylammonium bromide (CTAB), (vi) dodecanethiol (vii) poly(Nvinyl-2-pyrrolidone) (PVP), (viii) poly(amido amine) (PAMAM), (ix) polyvinyl alcohol (PVA), and (x) chitosan etc. Depending on type of surfactant and reaction condition, typically these capping ligands produces 10-50 nm sized nanoparticles¹¹, where the particle shape and distribution depend on the concentrations of the starting materials and reaction conditions¹¹. Even when these capping agents are employed, the synthesis of stable and monodispersed non-noble metal (Fe, Co, Ni, and Cu) nanoparticles is quite challenging because of the propensity of metal nanoparticles to oxidize and due to the poor stability of capping ligands in acids/bases¹⁰. While in noble metals (Pt, Pd and Au) the virtue of stable oxidation states allow them to prepare in aqueous and non- aqueous methods¹⁰. In many cases, the surfactant molecules while operating as a capping agent around the nanoparticles could decompose under the operating conditions and thereby destabilizes the nanoparticle, this minimizes the durability of the nanoparticle dispersions^{10,12}. Further, removal of capping agents from the surfaces of metal nanoparticles after immobilization or before catalysis is not always successful for most of the capping agents and the role of surfactants on particle growth remains unquantified^{8,13}.

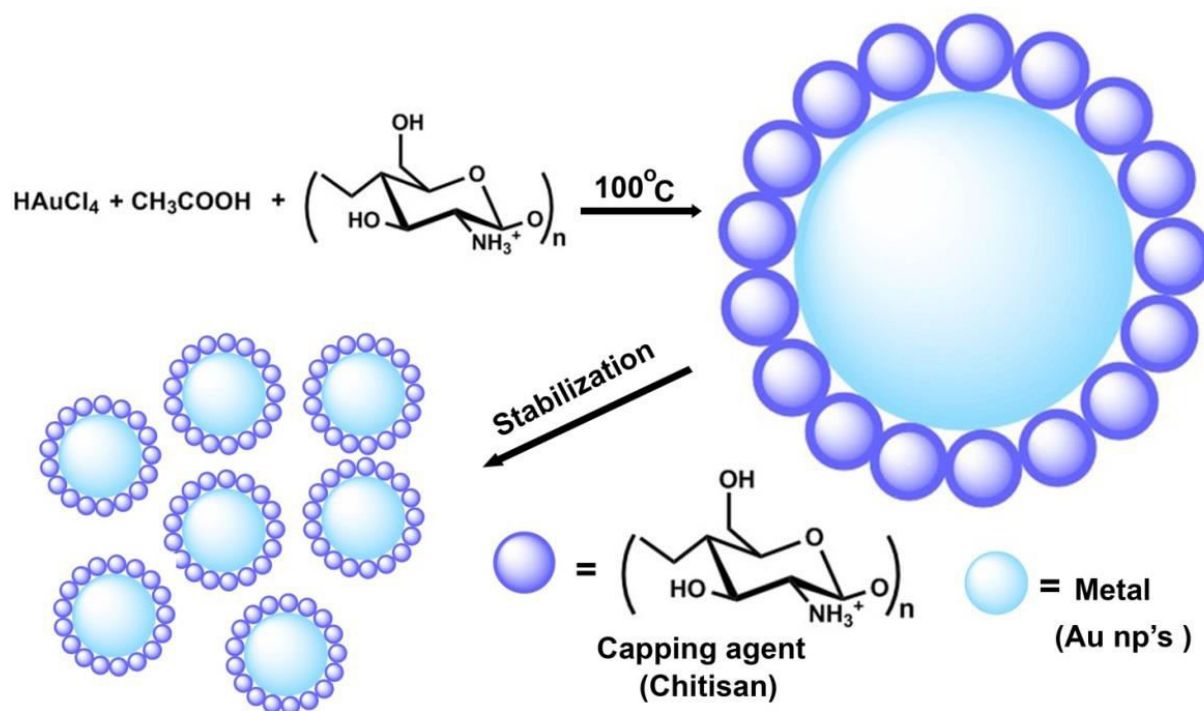


Figure 2. Schematic illustration of metal (Au) nanoparticle synthesis using capping agent method. This figure demonstrates how capping-agent is blocking the active surface of the metal nanoparticles. Note: Removal of the capping-agent would make the nps aggregate into bulky clusters owing to their high surface energy.

1.1.3.2. Porous Materials Supported Nanocatalysis

An alternate approach to overcome this is to grow the catalytic nanoparticles on high surface area porous supports- "capping-agent free" method¹⁴. This is a prominent way to synthesize specific sized metal nanoparticles where they inherently form homogenous dispersions. Meanwhile, the micro-mesopores in these supports can offer suitable nanoconfinement to the growth of extremely small-sized nanoparticles. The porous structure would provide enhanced catalyst accessibility. However, the stability, durability and compatibility of these porous supports and their np composites, under harsh reaction conditions, pose a severe challenge¹⁴. Importantly, different reactants come with different steric requirements, hence the porous material needs to be designed to have pore sizes and shapes capable of accommodating the sterics. Also, the selectivity of the products can heavily be influenced by the size and geometry of these pores^{8,15}. In special cases, the pores can even control the selectivity between two

intermediates and thereby decide the final product¹⁵. Therefore synthesis of stable and novel functional organic supports for nps construction is highly desired.

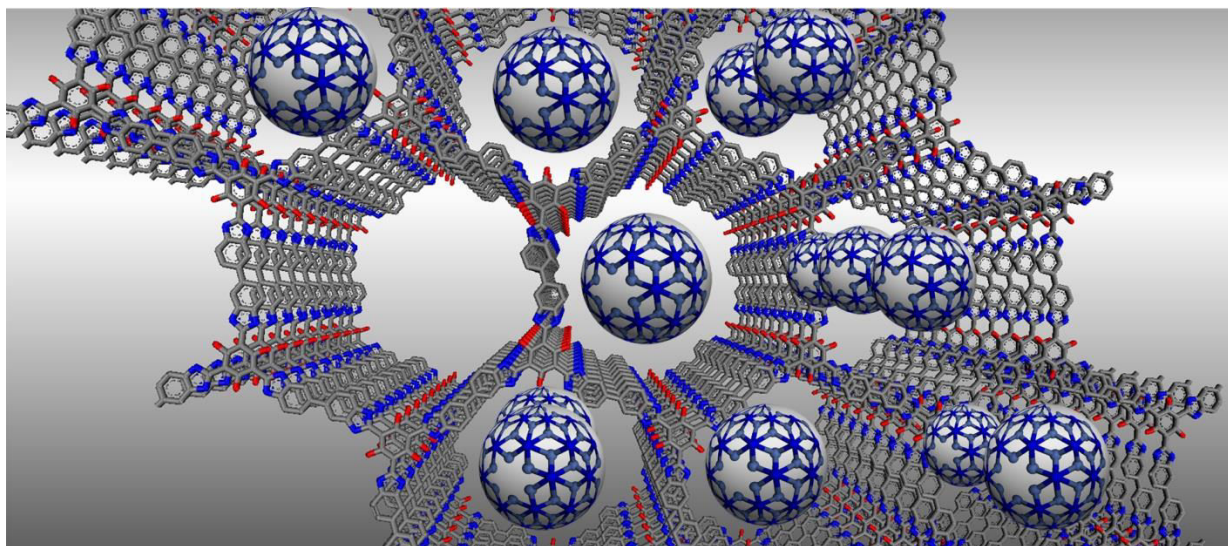


Figure 3. Confined growth of metal nanoparticle in a porous Covalent Organic Framework. Here the metal nanoparticles reside in the large pores of the framework, as a result their active surfaces become accessible to the reactants. This enables smoother reactions with rapid kinetics.

1.1. Choices of Porous Materials for Nanocatalysis

Solid substrates that contain pores or channels or cavities deeper than the average width of the material are called porous materials¹⁶. Depending on their pore size, porous materials are classified into various types i) ultra-microporous (3-6 Å), (ii) microporous (pore size 6-20 Å), (iii) Mesoporous (pore size > 20 Å) iv) Macroporous (pore size > 500 Å.). The well-known porous materials like Zeolites, Porous Carbon, Porous Coordination Polymers (PCPs) or Metal Organic Frameworks (MOFs), and Porous Organic Polymers (POPs) have been widely studied. Many of them are considered as promising supports for a variety of catalytically active particles which find application in varied areas^{16, 17}. However, owing to their poor hydrolytic stability and lack of acid/base stability, these pristine materials are considered unprivileged as a host for nanoparticle synthesis and heterogeneous nanocatalysis. Therefore, synthesis of novel and stable, functional porous supports for nanoparticle synthesis is desirable.

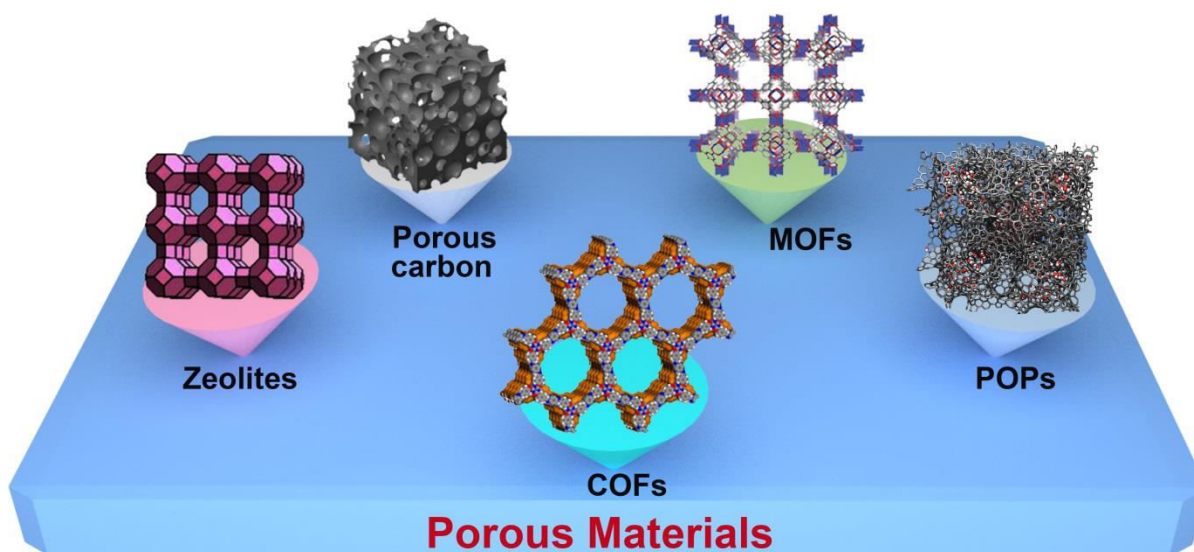


Figure 4. Well-known high surface porous materials used for the wide range of catalytic applications.

1.2. Covalent Organic frameworks (COFs)

Among the family of porous materials, Covalent Organic Frameworks (COFs) form a new class of crystalline porous polymers constructed with lightweight elements (H, B, C, N, and O) connected through strong covalent bonds¹⁸.

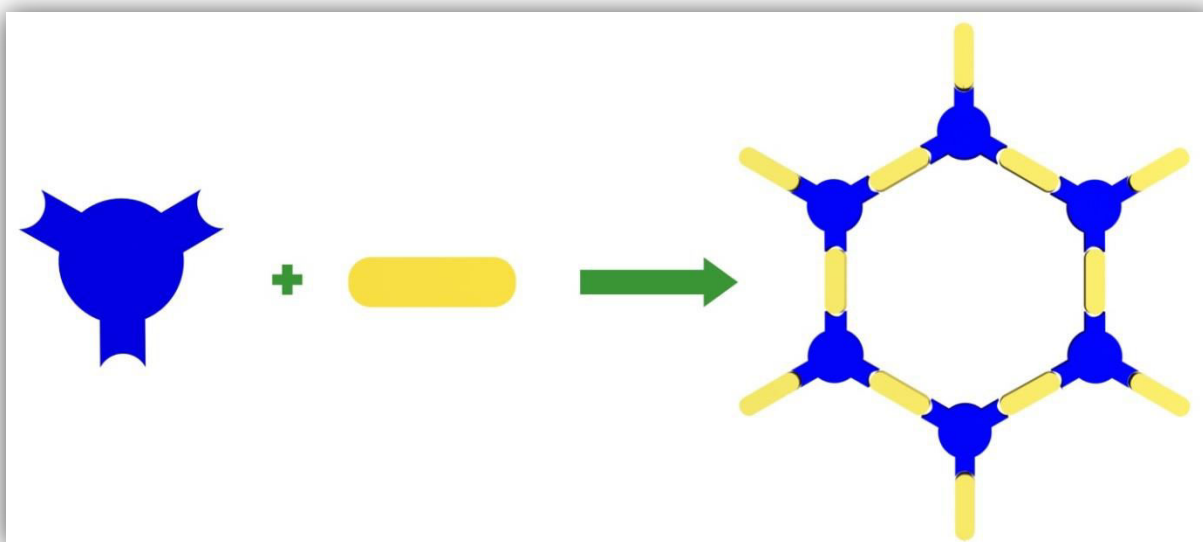


Figure 5. Schematic representation of the covalent organic frameworks construction and its topology.

In COFs, organic monomers or building units are self-condensed into polymers, which precipitate as a crystalline solid. They have extended polymeric structure possessing ordered pores and a periodic skeleton. Over the past decade, COFs have attracted tremendous interest because of the availability/accessibility of an expansive library of functional monomeric building blocks. Coupled with their designability into diverse topologies, they present limitless possibilities.

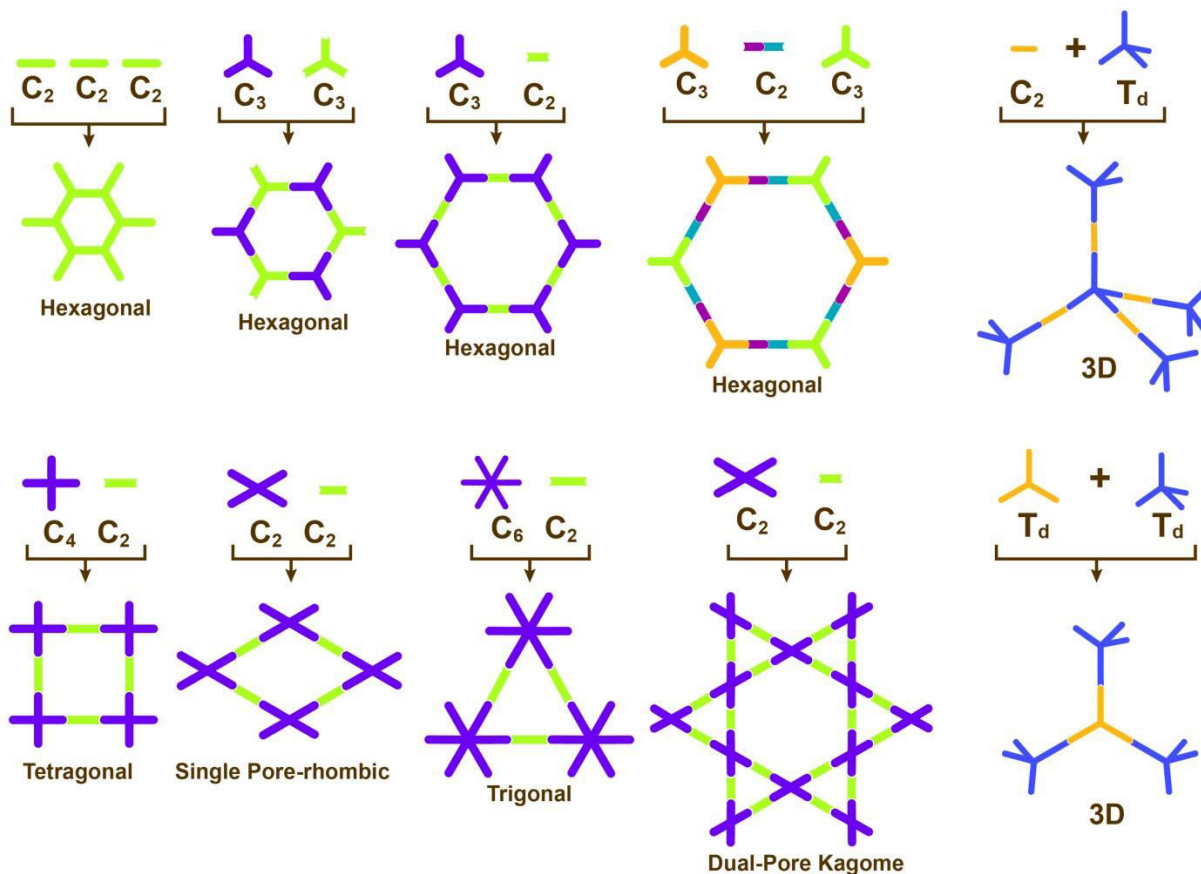


Figure 6. Topology diagrams showing the general synthetic strategies to design various structures of COFs skeletons from their respective building units.

The major advantage of COFs is designable architectures, topology, pore size and dimensions (2D or 3D) of the frameworks which completely depends on the geometry of molecular building blocks or monomeric unite employed in the reaction¹⁹. Figure 6 illustrates the various symmetric strut assemblies ($C_1+C_1+C_1$, C_2+C_3 , C_3+C_3 , C_6+C_6 ...ect) yielding different lattice structures. Furthermore, COFs have inherent uniform porosity, tunable functionality,

structural regularity, chemical diversity, high thermal and chemical stability²⁰. These advantages make COFs as ideal candidate or host for a wide range of applications such as gas storage, drug delivery, sensing, proton-conduction, energy storage and heterogeneous catalysis²¹. In the recent times, reports on COFs based heterogeneous catalysts are surging and given the synthetic variations, a wide range of chemical availability, there is a huge scope to design and develop new catalysts for a variety of small molecule transformations with enhanced catalytic activity and durability²². The progress in the synthesis and catalytic applications of COFs will be discussed briefly in the following sections

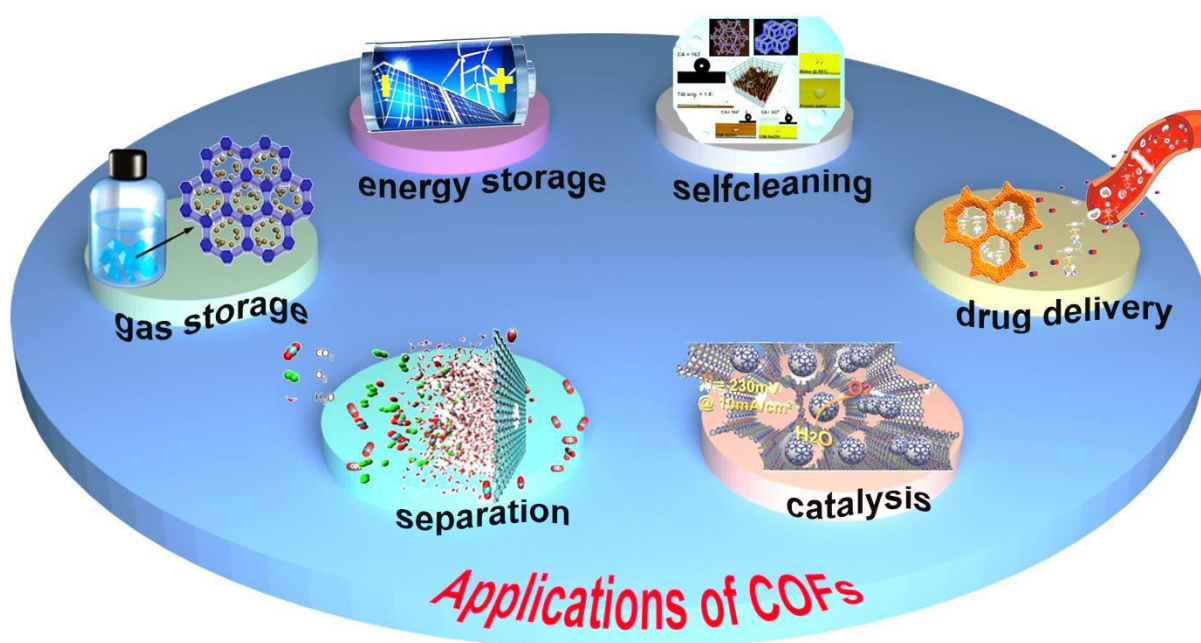


Figure 7. Schematic representation illustrates various potential applications of covalent organic frameworks.

1.3. Covalent Organic Frameworks Supported Nanocatalysis-Recent literature

The integration of noble metal nanoparticles with covalent organic frameworks has become an efficient strategy in designing heterogeneous catalysts. Heterogeneous nature of COFs benefits easy recovery and recycling, while the presence of large mesopores supports facile diffusion of the reactants towards the active metal surface.

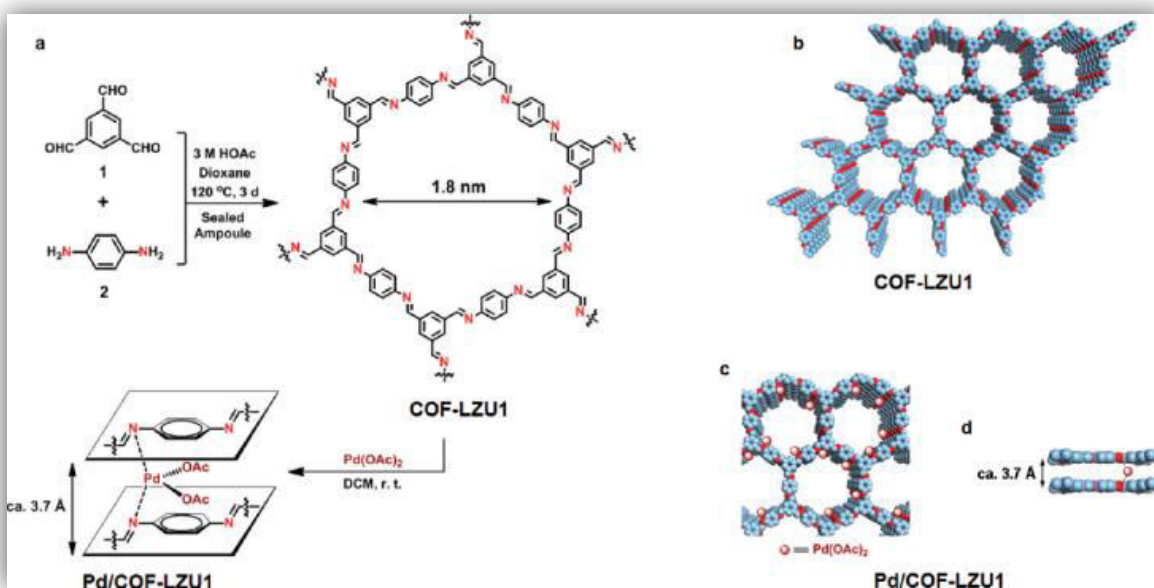


Figure 7. Schematic illustrations show, (a) the synthetic procedure of COF-LZU1 and Pd/COF-LZU1 (d) interlayer distance between two adjacent layers of COF-LZU1 and Pd nps intercalation. Color code: C: blue, N: red, and brown spheres represent the incorporated Pd(OAc)₂. (b) simulated COF-LZU1 structure shows regular microporous (pore diameter of ~1.8 nm) with 2D eclipsed layered-sheet arrangement (c) schematic illustration of palladium nps loaded Pd/COF-LZU1. (Adopted from the reference no 23).

Wang and coworkers, in 2011, demonstrated the use of Covalent Organic Frameworks (named COF-LZU1) constructed from Schiff bonds as a support for Palladium nanoparticles²³. In this paper, they have synthesized a COF-LZU1 using condensation of 1,3,5-Triformylbenzene with 1,4-diaminobenzene in a 1,4-dioxane at 120⁰C for three days. Then metal loading was carried out via a post-synthetic treatment; Pd(II) acetate was embedded into the COF-LZU1 to get Pd/COF-LZU1 catalyst. The resulting Pd/COF-LZU1 catalyzes the Suzuki-Miyaura coupling reactions with 96-98% yields. It is noteworthy that Pd/COF-LZU1 catalyst does not show any drop in activity even after four cycles. In comparison with the other crystalline porous materials (zeolites, MOFs, polymers), the unique structure of COF-LZU1 and strong Pd-nitrogen interactions in Pd/COF-LZU1 gave superior catalytic activity and good recyclability.

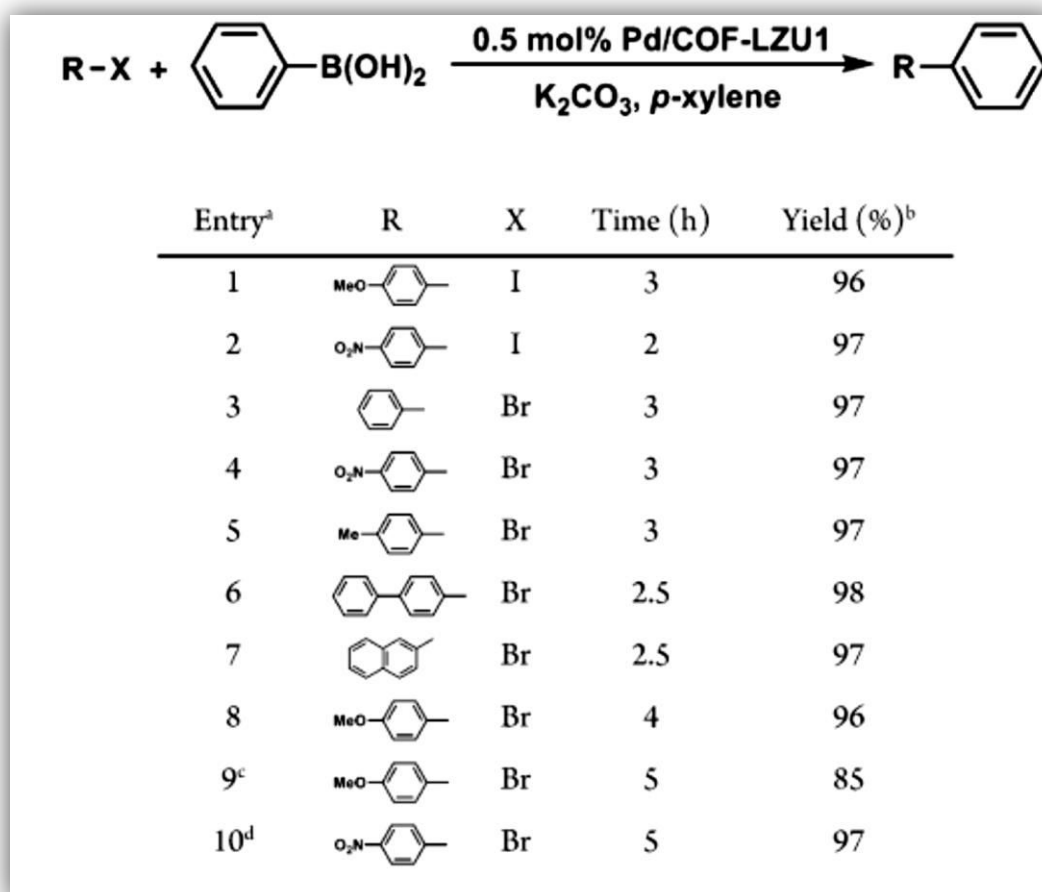


Table 1. Library of Suzuki Miyaura coupling reaction catalyzed by Pd/COF-LZU1 nanocatalyst Reaction condition: phenylboronic acid (1.5 mmol), aryl halide (1.0 mmol), K₂CO₃ (2.0 mmol), Pd/COF-LZU1 (0.5 mol %), and 4 mL of p-xylene at 150°C. (Adopted from the reference no 23).

Later in 2014, Banerjee and co-workers²⁴ synthesized a robust multifunctional COF (TpPa-1) and investigated their catalytic activity by incorporating both Pd(II) and Pd(0) nanoparticles (Pd(0)@TpPa-1, Pd(II)@TpPa-1). Their COF loaded with Palladium nanoparticles Pd(0)@TpPa-1, (Pd nps size 4-10nm) exhibited good activity towards Cu free Sonogashira, Heck reaction and sequential one-pot Heck–Sonogashira cross-coupling reactions. Whereas Pd(II)@TpPa-1 (Pd nps size 15-40nm) displayed moderate activity for the intramolecular oxidative biaryl synthesis. The authors relate the virtue of loading small Pd nanoparticles in the COF show superior performance than commercially available Pd/C (10 wt%) under highly acidic and basic conditions. Interestingly, both their catalysts exhibit a good turnover number (TON, 305-275) and turnover frequency (TOF, 51-32h⁻¹). However, these

catalysts (Pd(0)@TpPa-1, Pd(II)@TpPa-1) did not show any appreciable activity when recycled. Also a considerable amount of nanoparticle leaching and aggregation of palladium nps on COF surface was observed after the catalysis. Soon after, another similar strategy of triazine-functional Pd(II)/COF-SDU1 was reported for the one-pot silicon-based cross-coupling reactions of silanes and various aryl iodides²⁵ Herein, these triazine-based COFs acted as an efficient support for the immobilizing Pd nanoparticles (size 3-4 nm) and Pd(II)/COF-SDU1 catalyst. They shown no loss of activity over four cycles for the organosilanol coupling C-C bond formation reactions. Later, a 3D microporous Pd(OAc)₂@COF-300 catalyst²⁶ was used for the phosphine-free Suzuki–Miyaura, Heck, and Sonogashira cross-coupling reactions under continuous-flow conditions. (average diameter of 5±1 nm)

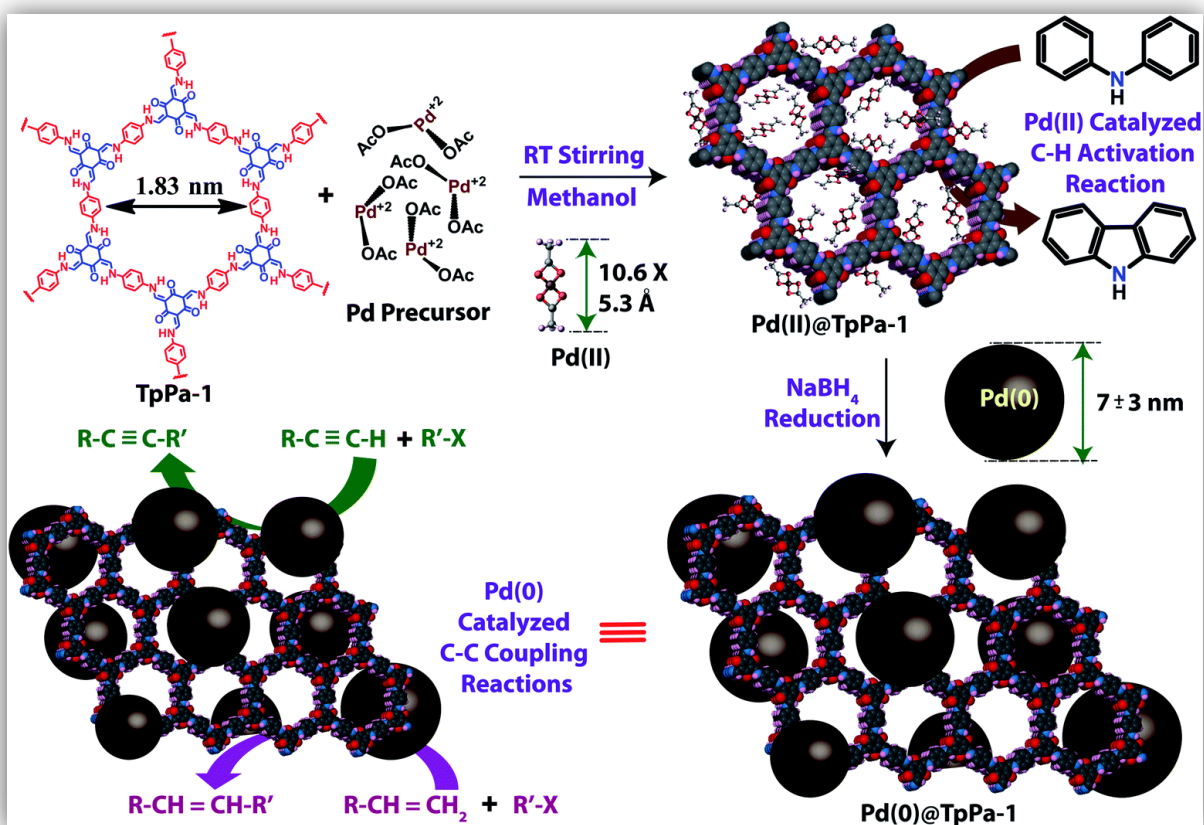


Figure 8. The schematic illustration shows a synthetic procedure for the palladium nanoparticle loading to the TpPa-1 COF (Pd(II)@TpPa-1 and Pd(0)@TpPa-1) and their catalytic activity in Heck, Sonogashira and oxidative biaryl couplings. (Adopted from the reference no 24).

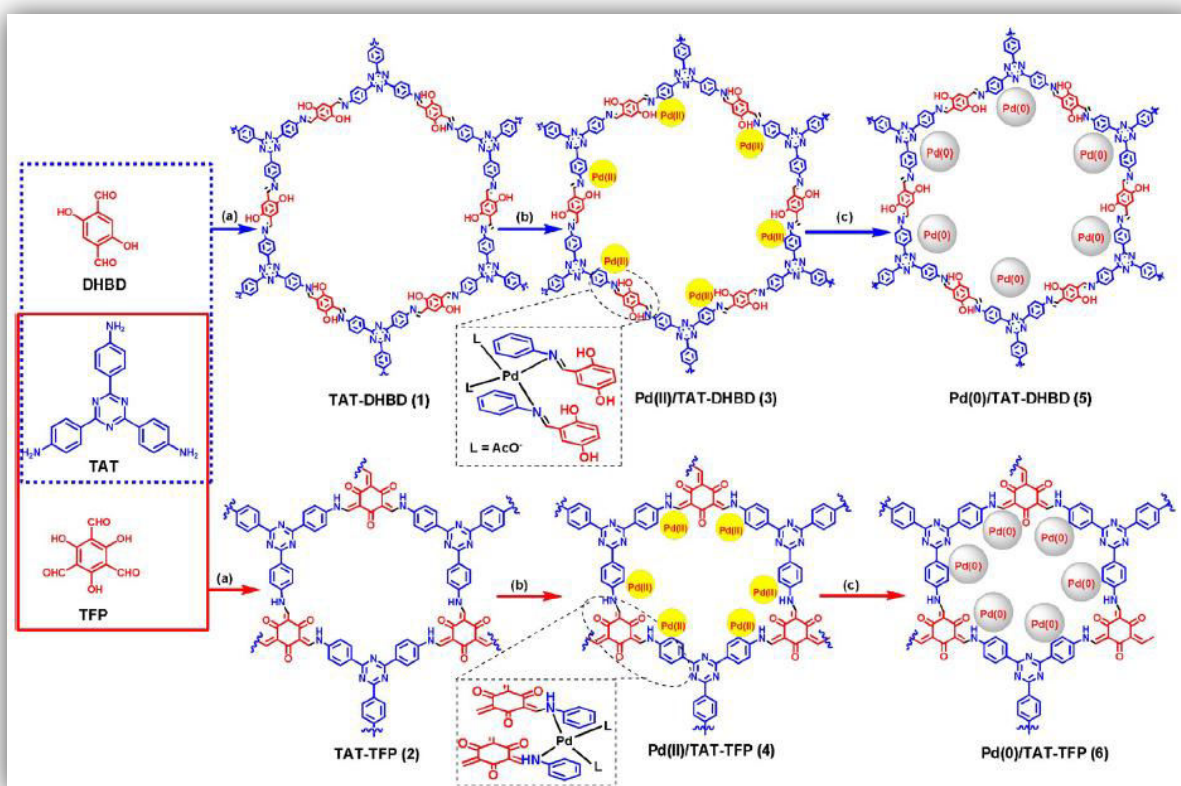


Figure 9. Illustration of the synthesis procedure for the TAT-DHBD (1), TAT-TFP (2) and their palladium loading procedures COFs Pd^{II}/TAT-DHBD (3), Pd^{II}/TAT-TFP (4) Pd⁰/TAT-DHBD (5) and Pd⁰/TAT-TFP (6) (a) both the monomers were dissolved in dioxane and mesitylene, 6M CH₃COOH at 120 °C for 3 days; (b) Post-treatment of COFs 1 and 2 with Pd(OAc)₂ in presence of CH₂Cl₂ at room temperature for 24 hrs. c) Pd^{II}/TAT-DHBD (3), Pd^{II}/TAT-TFP salts were reduced with NaBH₄ in the presence of MeOH at room temperature for 48 hrs. (Adopted from the reference no 27).

In continuation with these studies, Murugavel and co-workers synthesized a family of novel nitrogen-rich triazine-based COFs (Pd^{II}/TAT-DHBD (3), Pd^{II}/TAT-TFP (4) Pd⁰/TAT-DHBD (5) and Pd⁰/TAT-TFP (6)) and studied their catalytic activity for Suzuki–Miyaura coupling reactions²⁷. Interestingly they found that the reaction with Pd⁰/TAT-TFP catalyst exhibits 100% substrate conversion for the 4-cyano-bromobenzene coupling reaction within 4 hrs (Figure 9). They also state that the compounds 3–6 show a substantial loss in catalytic activity and a meager leaching of the Pd nanoparticles after three catalytic cycles. These results are superior than some of the earlier reports²⁴. Additionally, they demonstrated that the Pd loaded COFs have better efficiency for CO₂ adsorption. Pd^{II}/TAT-TFP (4) showed 11.0 wt% CO₂ uptake whereas Pd⁰/TAT-TFP (6) exhibited 5.8 % CO₂ uptake at 273K. These CO₂ uptake amounts surpassed the Pd-loaded polymer Azo-CPP-1-Pd (9.17 wt% at 273 K and 1 bar).

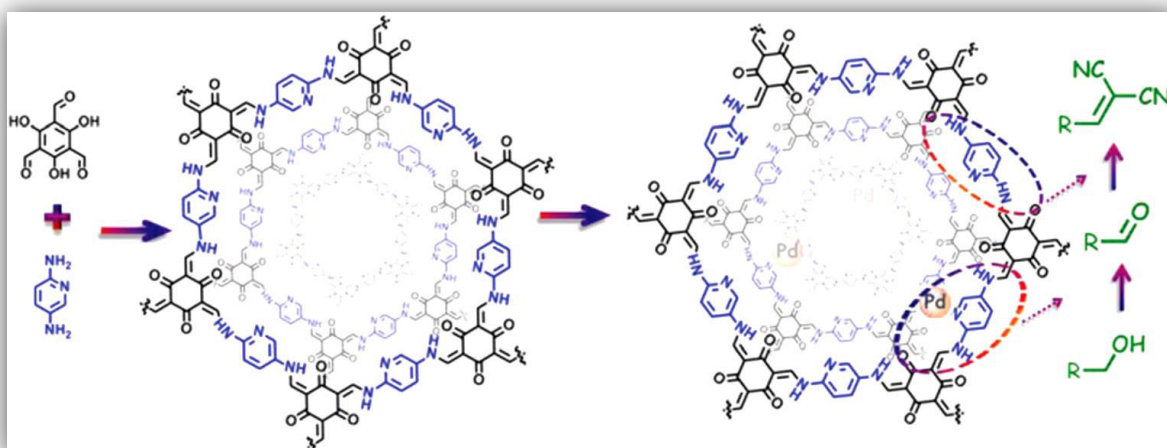


Figure 10. Schematic representation illustrates the synthetic procedure for the Pd/COF-TpPa-Py catalyst and one-pot cascade aerobic (alcohols to α,β -unsaturated dinitriles) Oxidation–Knoevenagel condensation reactions. Reaction condition: a mixture of alcohol (1 mmol), and Pd/COF-TpPa-Py were stirred in the presence of toluene (10 mL) at 80°C under O₂ (1 atm) for 1 hr. Then malononitrile (1.05 mmol) was added to the mixture and the overall reaction was stirred for 12hrs to obtain α,β -unsaturated dinitriles. (Adopted from the reference no 28).

Ma and co-workers adopted a similar strategy employing pyridyl-rich COF for anchoring Pd nanoparticles (Pd/COF-TpPa-Py). They utilized it for catalyzing the bifunctional cascade reactions²⁸. The basic pyridyl functional groups in their COF interacts strongly with the Pd nanoparticles (confirmed by XPS) (Figure 10). The resulting Pd@COF-TpPa-Py catalyst showed excellent catalytic activity (98% yield) for the two step Oxidation–Knoevenagel condensation reaction converting alcohols to α,β -unsaturated dinitriles. Notably, the Pd/COF-TpPa-Py catalyst outperforms the corresponding homogeneous counterparts (Pd(OAc)₂ + pyridine or Pd(OAc)₂) and the heterogeneous porous organic polymer supported Pd nanocatalyst (Pd/POP-Py). Furthermore, recyclability studies indicate no loss of activity over six consecutive reactions and they retain over 95% yield. The Pd nanoparticle leaching was just below the detection limit of 0.1 ppm as ascertained from the ICP-OES analysis.

In 2017, Banerjee and co-workers designed another strategy for loading Pd nanoparticles into COFs²⁹. They have introduced a predesigned Pd-anchored pyridyl amine monomeric building unit and synthesized COF through in-situ loading of 2,2'-bipyridine-5,5'-diamine

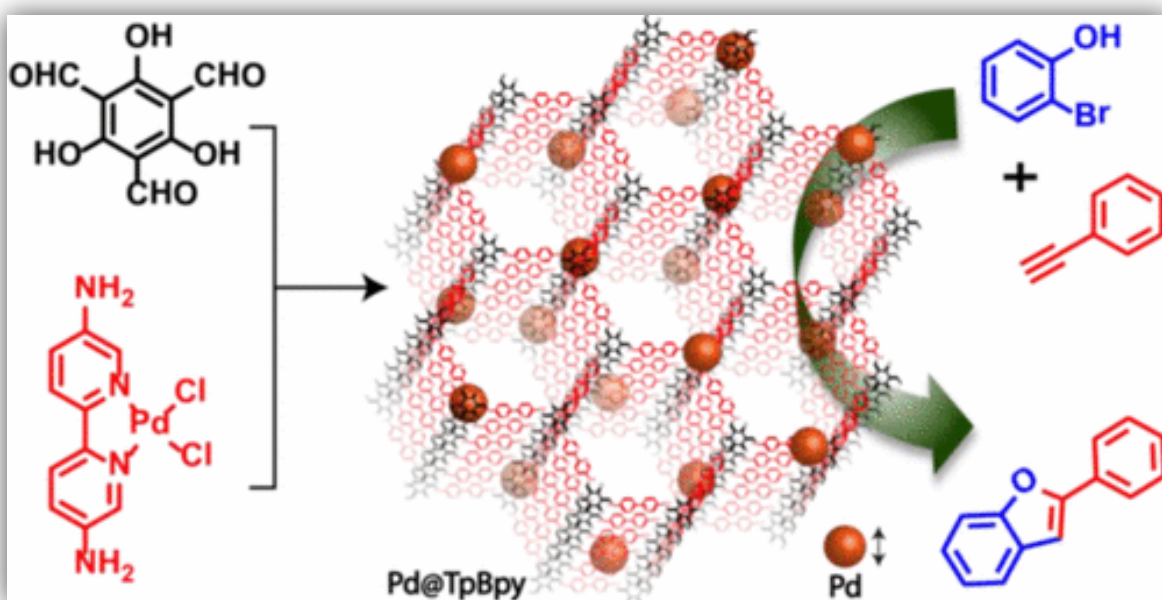


Figure 11. Schematic representation and synthetic procedure for the in-situ loading of Pd nanoparticles (Pd@TpBpy) and their tandem catalytic reactions. Reactions were carried out with 2-bromophenol (0.5 mmol), phenylacetylene (0.6 mmol), 0.6 mol % of Pd@TpBpy catalyst and K₂CO₃ (0.5 equiv) in DMF at 150 °C. (Adopted from the reference no 29).

palladium chloride (Bpy-PdCl₂) and 1,3,5-triformylphloroglucinol (Tp) at 90⁰C for 3 days (Figure 11). The In-situ generated of Pd nanoparticles (Pd@TpBpy) showed good catalytic activity towards the synthesis of biologically and pharmaceutically important 2-substituted benzofurans from 2-bromophenols and terminal alkynes. This tandem catalytic method yields a notable turnover number (TON up to 1101) and turnover frequency (TOF up to 495h⁻¹) for a heterogeneous nanocatalysis. Additionally, this hybrid composite Pd@TpBpy material has shown superior catalytic performance than the commercially available homogeneous catalysts such as PdCl₂, Bpy-PdCl₂, TpBpy and the heterogeneous Pd/C catalyst under similar reaction conditions. But recyclability studies displayed substantial loss in activity just after the initial cycle and exhibited only ≤60 % activity after four cycles. This loss of activity indicates that the majority of nps were deposited on the surface rather than encapsulated in the pores. This leached Pd particles contribute significantly towards the high activity in the former cycles which gradually decreases in the later ones. From the TEM, they noticed that the sizes of the Pd nanoparticles are 5-25nm in range, which are substantially bigger than the pore size of the COF

support ~ 2.3 nm. Similarly, TEM images of post catalyst further stated that Pd nps are aggregated into bulk assemblies. These results strongly indicate that the TpBpy COF support and Pd nanoparticles have weak interactions between them. Therefore all these results demonstrate, the predesigned Pd-anchored loading method does not have great control over the particle size and distribution of nps as a result poor recyclability was obtained.

More recently, Zhang and co-workers reported another strategy for the confined growth of ultrafine metal Pd and Pt nanoparticles in COFs through metal-sulfur binding interactions³⁰. Here, Pt or Pd loaded COFs (Pt@COF and Pd@COF) were prepared through a double solvent method³¹. Typical procedure involves dispersion of 4mg of thio-COF in 3 mL of methanol to which 2.0mL of aqueous K_2PdCl_4 (4 mg, 1.2×10^{-2}) or K_2PtCl_4 (5 mg, 1.2×10^{-2} mmol) solution is added, The resulting mixture is then brought to dryness and redispersed in the same mixture of solvents and finally reduced with $NaBH_4$ to produce fine dispersions of Pt or Pd nanoparticles PtNPs@COF and PdNPs@COF (Figure 12). The unique synthetic procedure and

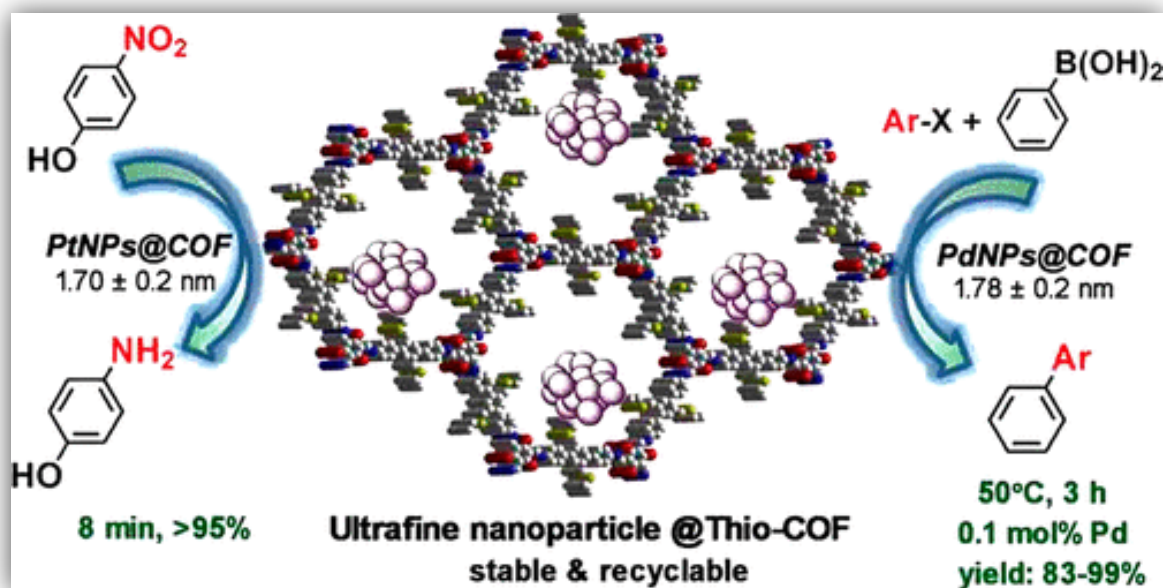


Figure 12. Schematic representation of the nanoparticle loaded thio-COFs (PdNPs@COF and PtNPs@COF) and their catalytic modeled reactions (a) Suzuki–Miyaura coupling reaction: phenylboronic acid (1.1 mmol), arylhalide (1 mmol), PdNPs@COF (0.5 mol %), K_2CO_3 (1.5 mmol), and DMF/ H_2O (1.5 mL/1.5 mL) at 50 °C. (b) Nitro reduction: 4-nitrophenol (1.0×10^{-3} M, 0.3 mL), PtNPs@COF (0.5 mg/mL, 25 or 50 μ L) and aqueous solution of $NaBH_4$ (0.5 M, 1 mL) stirred at room temperature. (Adopted from the reference no 30).

thioether functional groups in COF offer immobilization of ultrafine nanoparticles within the pores. The average size of the Pd or Pt nanoparticles was found to be 1.7 ± 0.2 nm which are smaller than the pore size (2.4 nm) of the COF.

These nanoparticles are smallest in size among all noble metal loaded COFs reported till date. The obtained PtNPs@COF and PdNPs@COF catalysts show excellent catalytic activity for the nitrophenol reduction and Suzuki–Miyaura coupling reaction with low catalyst loading. Remarkably, the catalyst does not lose its activity ($\geq 98\%$) even after five cycles, as the protecting thioether alkyl shell is preventing the aggregation of metal nps. The interaction between Pd and S is further investigated by X-ray photoelectron spectroscopy (XPS) analysis. The binding energy of the Pt(0) species in the PtNPs@COF has a higher value compared to that of pure Pt nps while the binding energy of S 2p in PtNPs@COF has a negative shift compared to that of sulfur in Thio-COF. These shifts are caused by metal-ligand interactions and the charge transfer from platinum (Pt) nanoparticles to sulfur (S) atoms. Thus resulting catalyst do not leach out during the catalysis and displays high activity.

In addition to the traditional coupling reactions, COFs supported nanocatalysts were also used for the various functional group transformation reactions. In 2014, Banerjee and coworkers developed Au(0)@TpPa-1 catalyst for the nitro to amine functional group hydrogenation reaction³². In this paper, they incorporated Au(0) nanoparticles into COF TpPa-1 by solution infiltration method. Resulting Au(0)@TpPa-1 (1.20 wt% of Au nps) catalyst showed superior catalytic activity ($\sim 5.35 \times 10^{-3} \text{ s}^{-1}$) and faster reaction kinetics than the pristine $\text{HAuCl}_4 \cdot 3\text{H}_2\text{O}$ ($\sim 3.01 \times 10^{-3} \text{ s}^{-1}$) for the 4-nitrophenol to 4-aminophenol hydrogenation reaction in the presence of excess NaBH_4 in the aqueous medium (Figure 13). Remarkably, recyclability studies on time-dependent UV-Vis spectra displayed no considerable loss of activity ($\sim 95\%$) even after six conjugative cycles indicating truly heterogeneous reusable heterogeneous nanocatalyst. Later in 2017, another report appeared on the nitro functional group reduction reaction using Au@TAPBDMTP-COF³³. Unlike earlier report³² here, Guang Lu and co-worker loaded polyvinylpyrrolidone (PVP) surface functionalized Au nanoparticles into TAPB-DMTP-COF and studied for the 4-Nitrophenol reduction reactions (yield 98%). They observed that the PVP encapsulation method produces different sizes (3.5nm, 50nm, 100nm) and shapes (rod, spherical) of Au nanoparticles with different concentrations of gold loadings. This encapsulation method does not alter the crystallinity and stability of the COF. Additionally, this method

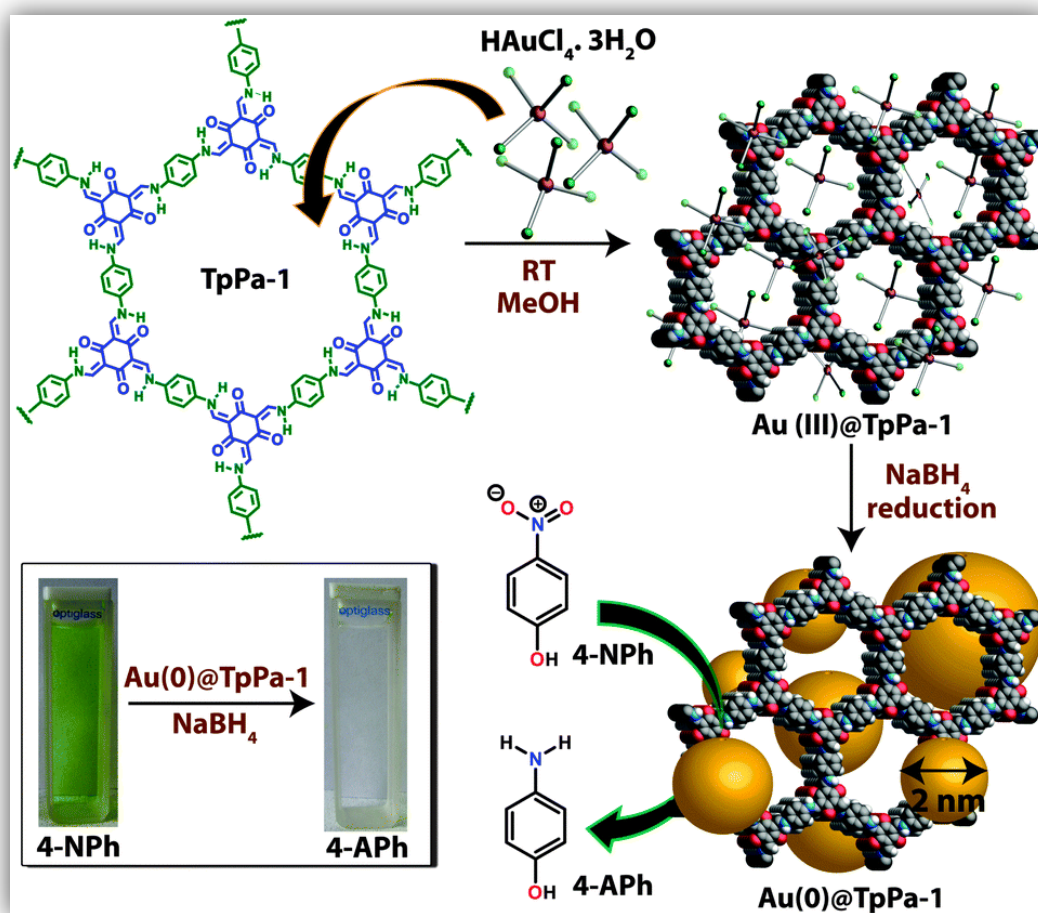


Figure 13. Schematic illustration of Au nanoparticles loading into a TpPa-1COF Au(0)@TpPa-1 and its catalytic reduction of 4-nitrophenol to 4-aminophenol (Adopted from the reference no 32).

exposes highly active Au nano sites in catalysis, as a result of which good recyclability (95% yield even after five cycles) with sustained high activity is obtained.

In addition to the Au@COF catalysis, Li and co-workers³⁴ used a palladium loaded COF derived carbon catalyst (Pd@NHCS) for the hydrogenation of nitrobenzene and oxidation of cinnamyl alcohol reactions in the presence of 1atm hydrogen gas (Figure 14). Here, a one-step in-situ synthetic strategy was adopted for the fabrication of Pd embedded nitrogen doped hollow carbon spheres (Pd@NHCS). The resulting Pd@NHCS500 composite showed significantly enhanced catalytic activity (98% yield) and good selectivity (primary NH_2) for the hydrogenation of nitrobenzene and oxidation of cinnamyl alcohol reactions than the commercially available Pd/N-C , $\text{Pd}^{\text{II}}\text{-LUZ1}$ and Pd/C catalysts. They stated the Pd(OAc)_2

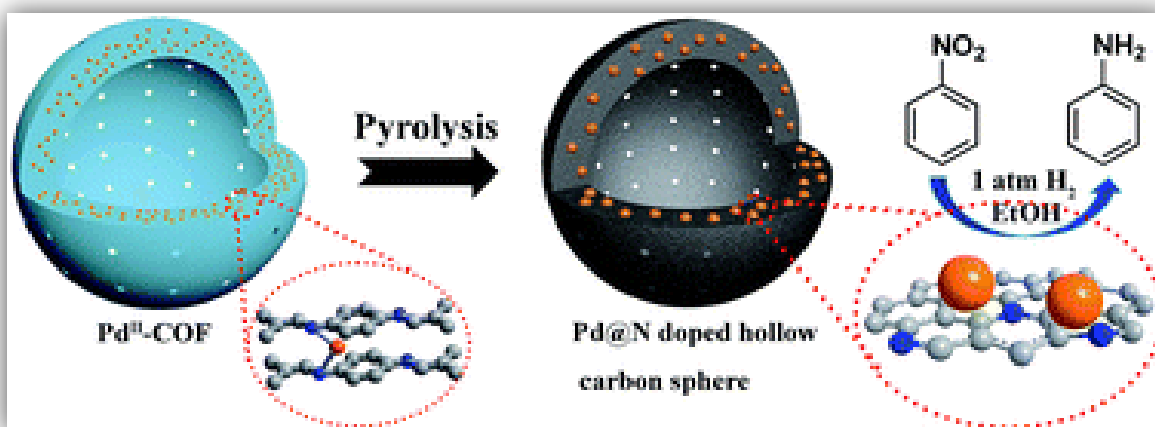


Figure 14. Schematic representation illustrates Pd embedded nitrogen doped hollow carbon spheres Pd@NHCS synthesis and its catalytic hydrogenation of nitrobenzene to aniline (Adopted from the reference no 34).

encapsulated COF (Pd@NHCS) carbonized at different temperatures gave different Pd loadings (2.4%, 3.6%, and 5.0%) and nanoparticle sizes (6-19nm) This could be due to lose/ evaporation of lightweight carbon or nitrogen elements at higher temperature leading to an increase overall in palladium weight percentage. However, all the catalysts offered similar catalytic activities indicating that the overall amount of active sites (total no of Pd nps) remain same in all the catalysts. This high activity is attributed to the synergistic effect between nitrogen doped porous hollow carbon and highly dispersed Pd nanoparticles. In addition to the Pd, Au based catalysis, Yu-Bin Dong and coworkers recently reported³⁵ Ru nanoparticles-loaded COFs (size of the Ru nps 2-5nm) for solvent-free one-pot tandem synthesis of imine compounds from the benzyl alcohols and corresponding amines under solvent-free conditions in air. The Ru@COF-ASB catalyst showed good activity, TOF- 0.75 h⁻¹ and recyclability for the all the reactions.

Table1: Various organic transformation reactions catalyzed by COF supported nanocatalysts.

Catalyst	Metal	Catalytic reaction	Reference
Co@IISERP-COF5	Co	NO ₂ and CN Hydrogenation	<i>Small</i> , 2018 , 1801233
Pd@PPPP-1 Pd@PPPP-2	Pd	Suzuki–Miyaura	<i>Polym. Chem.</i> , 2018 , 9, 1430
Ru@COF-ASB	Ru	Benzyl Alcohols Oxidation	<i>Inorg. Chem.</i> 2018 , 57, 2678
PtNPs@ thio-COF, PdNPs@ thio-COF	Pt, Pd	nitrophenol reduction and Suzuki–Miyaura	<i>J. Am. Chem. Soc.</i> 2017 , 139, 17082
PdII/Pd0TAT-DHBD	Pd	Suzuki–Miyaura	<i>ChemPlusChem</i> 2017 , 82, 1253

Pd/COF-TpPa-Py	Pd	Knoevenagel condensation	<i>Mater. Chem. Front.</i> , 2017 , 1, 1310
Pd@TpBpy	Pd	Tandem Catalysis	<i>ACS Appl. Mater. Interfaces</i> 2017 , 9, 13785
Au@TAPB-DMTP-COF	Au	NO ₂ reduction	<i>ACS Appl. Mater. Interfaces</i> 2017 , 9, 7481
Pd(OAc) ₂ @COF-300	Pd	Suzuki–Miyaura	<i>ChemCatChem.</i> 2016 , 8, 743
Pd@NHCS	Pd	NO ₂ reduction	<i>Chem. Sci.</i> , 2016 , 7, 6015
Pd@IISERP-COF1	Pd	multi-fold Heck, homo C-C coupling Suzuki–Miyaura and CO oxidation	<i>Scientific Reports</i> 2015 , 5:10876
Pd(II)/COF-SDU1	Pd	Silicon-based cross-coupling	<i>RSC Adv.</i> , 2015 , 5, 41017
Au(0)@TpPa-1	Au	NO ₂ reduction	<i>Chem. Commun.</i> , 2014 , 50, 3169
Pd(0)@TpPa-1, Pd(II)@TpPa-1	Pd	Heck–Sonogashira	<i>J. Mater. Chem. A</i> , 2014 , 2, 7944
Pd/COF-LZU1	Pd	Suzuki–Miyaura	<i>J. Am. Chem. Soc.</i> 2011 , 133, 19816

Apart from the organic catalytic transformations, COF-based solid electrocatalysts drew major attention in the recent times. In 2016, Vaidhyanathan and co-workers^{14(a)} designed a novel conducting benzimidazole COF (IISERP-COF3, $\sigma=1.70 \text{ E}^{-05} \text{ S/cm}$) supported by Ni₃N as active OER catalyst for the electrocatalytic water oxidation ($2\text{H}_2\text{O} (\text{l}) \rightarrow \text{O}_2 (\text{g}) + 4 \text{H}^+ (\text{aq}) + 4\text{e}^-$) reaction. Herein, a Ni₃N@IISERP-COF3 showed excellent catalytic activity ($\text{TOF} = 0.52 \text{ s}^{-1}$)

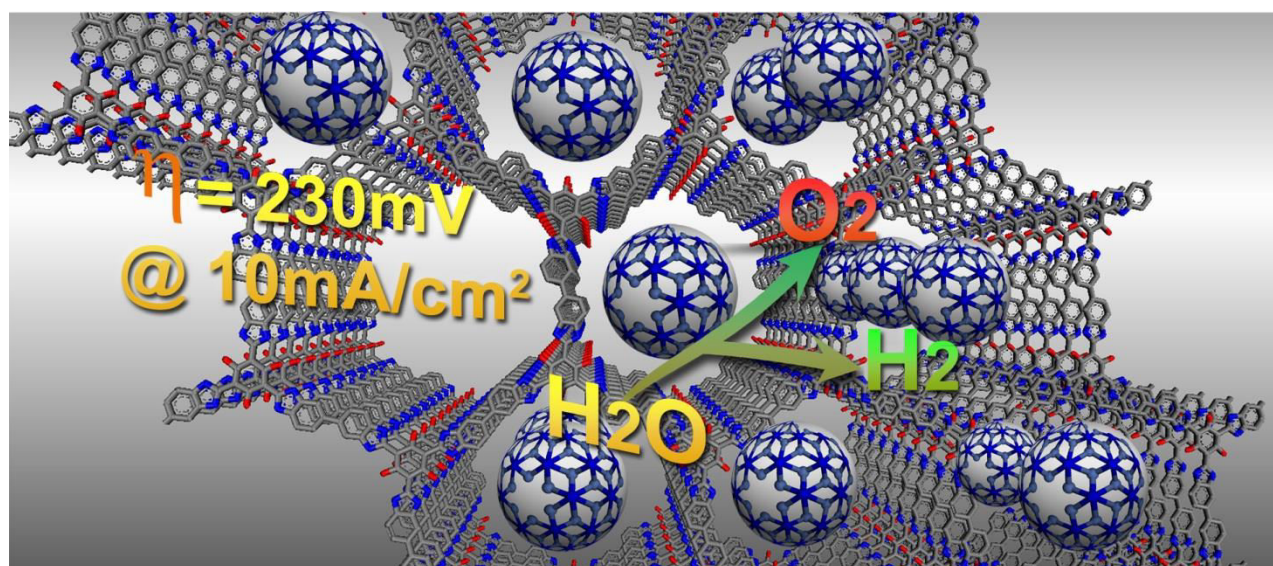


Figure 15. Schematic representation illustrates Ni₃N embedded nitrogen-rich benzimidazole COF (Ni₃N@IISERP-COF3) catalyst catalyzes the electrocatalytic water oxidation reactions (Adopted from the reference no 14a).

with the onset potential of 1.43 V and overpotential (η) of 230 mV at 10 mA cm⁻² current density (Figure 15). Also the catalyst showed remarkable activity at a wide range of current densities, overpotential (η_{10}) 230 mV @ 10 mA cm⁻², 250 mV @ 20 mA cm⁻², 290 mV @ 50 mA cm⁻² and $\eta < 300$ mV @ of 50 mA cm⁻². The electrochemical stability studies from chronoamperometry measurements revealed as stable current generation for over 20 hrs with a Faradaic efficiency of 98% @ 1 mA cm⁻². Additionally, the superiority of the catalyst support (IISERP-COF3) was demonstrated by loading the NiN₃ nps into other porous IISERP-COF1 ($\eta = 280$ @ 10 mA cm⁻² and commercially available amorphous carbon ($\eta = 275$ @ 10 mA cm⁻²). Therefore, the excellent catalytic activity of Ni₃N@IISERP-COF3 is ascribed to synergy bonding between the conducting benzimidazole COF (band gap 1.49eV) and fine dispersion of Ni₃N nanoparticles within the pores. Similarly, in 2016, Banerjee and co-workers³⁶ delivered Cobalt (II) based COF (Co-TpBpy) OER catalyst. Herein the Co-TpBpy catalyst shows an overpotential of 400 mV at 1 mA/cm² current density at pH =7 with TOF of 0.23/s. Further catalyst does not lose its activity and retains 94% yields even after 1000 cycles. All these studies clearly demonstrate that the COFs supported nanocatalysts acts as a truly heterogeneous industrial catalyst.

1.4. References

1. Ross, J. Heterogeneous Catalysis Fundamentals and Applications. *Volume 1; Elsevier .B.* V, Oxford OX5 IGB, UK, **2011**.
2. Hagen, J. Industrial Catalysis a practical Approach, *Volume 3; WILEY-VCH*, Weinheim, **2015**.
3. Ralphs, K.; Hardacre, C.; James, S. L. *Chem. Soc. Rev.* **2013**, *42*, 7701-7718.
4. Global Catalyst Market, Acmite Market Intelligence Ratingen: Market Research Reports, *Ratingen, Germany* Volume 3, **2015**.
5. Van Leeuwen, P. W. N. M. and Chadwick, J. C. "Homogeneous Catalysts: Activity - Stability - Deactivation" *Wiley-VCH*, Weinheim, **2011**.
6. Ranga, S. Comparative Analysis of Homogeneous and Heterogeneous Catalysis *IJETSR*, Volume 4, Issue 9, **2017** 2394 – 3386.

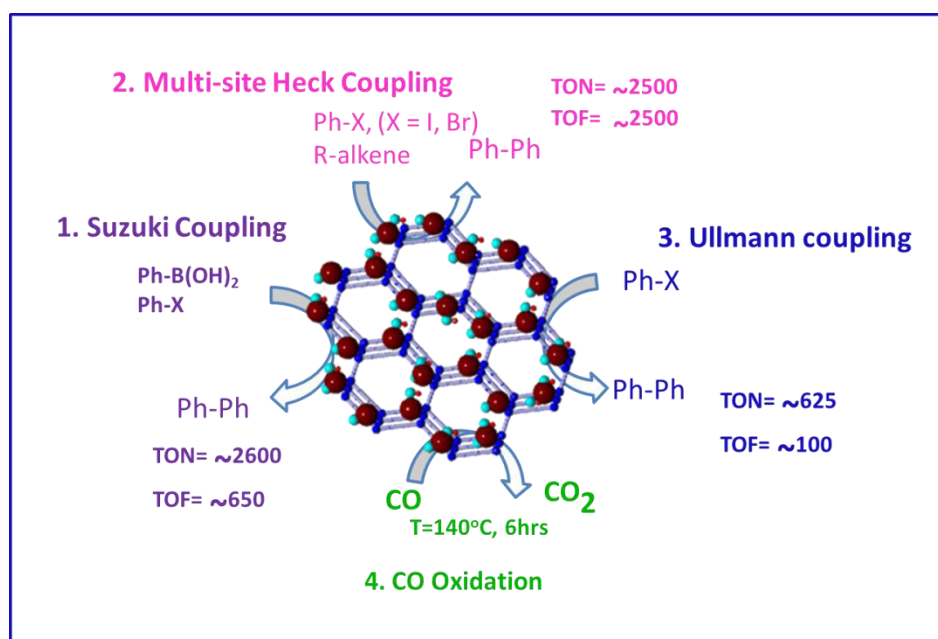
7. Gawande, M. B.; Zboril, R., Malgrasb, V.; Yamauch, Y. *J. Mater. Chem. A*, **2015**, 3, 8241.
8. (a) Bhumkar, D. R.; Joshi, H. M.; Sastry, M.; Pokharkar, V. B. *Pharm. Res.* **2007**, 24, 1415-26. (b) Stowell, C. A.; Korgel, B. A. *Nano Lett.*, **2005**, 5, 1203–1207. (c) Wang, C.; Wang, C.; Xu, L.; Cheng, H.; Lin, Q.; Zhang, C. *Nanoscale*, **2014**, 6, 1775-1781. (d) Phan, C. M.; Nguyen, H. M. *J. Phys. Chem. A* **2017**, 121, 3213–3219.
9. Rossi, L. M.; Fiorio, J. L.; Garcia, M. A. S.; Ferraz, C. P. *Dalton Trans*, **2018**, 47, 5889-5915.
10. Campisi, S.; Ferri, D.; Villa, A.; Wang, W.; Wang, D.; Kröcher, O.; Prati, L.; *J. Phys. Chem. C*, **2016**, 120, 14027–14033.
11. Yamamoto, M.; Kashiwagi, Y.; Nakamoto, M. *Z. Naturforsch.* **2009**, 64, 1305 -1311.
12. Chen, X.; Cai, Z.; Chen, X.; Oyama, M.; *J. Mater. Chem. A*, 2014, 2, 5668-5674.
13. Niu, Z.; Li, Y. *Chem. Mater.* **2014**, 26, 72–83 (b) Mott, D.; Galkowski, J.; Wang, L.; Luo, J.; Zhong, C. J. *Langmuir* **2007**, 23, 5740-5745.
14. Nandi, S.; Singh, S. K.; Mullangi, D.; Illathvalappil, R.; George, L.; Vinod, C. P.; Kurungot, S.; Vaidhyanathan, R. *Adv. Energy Mater.* **2016**, 6, 1601189. (b) Doonan, C. J.; Sumbly, C. J.; *CrystEngComm*, **2017**, 19, 4044-4048 (c) Zhu, L.; Liu, X. Q.; Jiang, H. L.; Sun L. B.; *Chem. Rev.*, **2017**, 117 (12), 8129–8176 (d) Cao, Y.; Mao, S.; Li, M.; Chen, Y.; Wang, Y. *ACS Catal.*, **2017**, 7, 8090–8112.
15. Mullangi, D.; Chakraborty, D.; Pradeep, A.; Koshti, V.; Vinod, C. P.; Panja, S.; Nair, S.; Vaidhyanathan, R. *Small*, **2018**, 1801233. (b) Fang, Q.; Gu, S.; Zheng, J.; Zhuang, Z.; Qiu, S.; Yan, Y. *Angew. Chem.* **2014**, 126, 2922 –2926.
16. Bruce, D. W.; Hare, D. O.; Walton, R. I. *Porous Materials*; John Wiley & Sons, Ltd **2011**.
17. Breck, D. W. *Zeolite Molecular Sieves*; Wiley & Sons: New York, **1984**.
18. (a) Cote, A. P.; Benin, A. I.; Ockwig, N. W.; O'Keeffe, M.; Matzger, A. J.; Yaghi, O. M. *Science* **2005**, 310, 1166-70. (b) Feng, X.; Ding, X.; Jiang, D. *Chem. Soc. Rev.* **2012**, 41, 6010. (d) Colson, J. W.; Dichtel, W. R. *Nat. Chem.* **2013**, 5, 453. (d) Kandambeth, S.; Mallick, A.; Lukose, B.; Mane, M. V.; Heine, T.; Banerjee, R. *J. Am. Chem. Soc.*, **2012**, 134, 19524–19527.
19. Huang, N.; Wang, P.; Jiang, D. *Nat. Rev. Mat.* **2016**, 1 16068.

20. Waller, P. J.; Gandara, F.; Yaghi, O. M. *Acc. Chem. Res.*, **2015**, *48*, 3053-3063.
21. Ding, S. Y.; Wang, W. *Chem. Soc. Rev.* **2013**, *42* (2), 548-68. (b) Chandra, S.; Kundu, T.; Kandambeth, S.; BabaRao, R.; Marathe, Y.; Kunjir, S. M.; Banerjee, R. J. *Am. Chem. Soc.*, **2014**, *136*, 6570–6573. (c) Vyas, V. S.; Haase, F.; Stegbauer, L.; Savasci, G.; Podjaski, F.; Ochsenfeld, C.; Lotsch, B. V. *Nat. Commun.* **2015**, *6*, 9508. (d) Mullangi, D.; Nandi, S.; Shalini, S.; Sreedhala, S.; Vinod, C. P.; Vaidhyanathan, R. *Sci. Rep.* **2015**, *5*, 10876.
22. Rogge, S. M. J.; Bavykina, A.; Hajek, J.; Garcia, H.; Olivos-Suarez, A. I.; Sepulveda-Escribano, A.; Vimont, A.; Clet, G.; Bazin, P.; Kapteijn, F.; Daturi, M.; Ramos-Fernandez, E. V.; Llabres, I. X. F. X.; Van Speybroeck, V.; Gascon, J. *Chem. Soc. Rev.* **2017**, *46*, 3134-3184.
23. Ding, S. Y.; Gao, J.; Wang, Q.; Zhang, Y.; Song, W. G.; Su, C. Y.; Wang, W. *J. Am. Chem. Soc.* **2011**, *133*, 19816-22.
24. Pachfule, P.; Panda, M. K.; Kandambeth, S.; Shivaprasad, S. M.; Díaz, D. D.; Banerjee, R. *J. Mater. Chem. A* **2014**, *2*, 7944-7952.
25. Lin, S.; Hou, Y.; Deng, X.; Wang, H.; Sun, S.; Zhang, X. *RSC Adv.* **2015**, *5*, 41017-41024.
26. Gonçalves, R. S. B.; de Oliveira, A. B. V.; Sindra, H. C.; Archanjo, B. S.; Mendoza, M. E.; Carneiro, L. S. A.; Buarque, C. D.; Esteves, P. M. *ChemCatChem* **2016**, *8*, 743-750.
27. Kaleeswaran, D.; Antony, R.; Sharma, A.; Malani, A.; Murugavel, R. *ChemPlusChem* **2017**, *82*, 1253 – 1265.
28. Sun, Q.; Aguila, B.; Ma, S. *Mater. Chem. Front.*, **2017**, *1*, 1310.
29. Bhadra, M.; Sasmal, H. S.; Basu, A.; Midya, S. P.; Kandambeth, S.; Pachfule, P.; Balaraman, E.; Banerjee, R. *ACS Appl. Mater. Interfaces* **2017**, *9*, 13785-13792.
30. Lu, S.; Hu, Y.; Wan, S.; McCaffrey, R.; Jin, Y.; Gu, H.; Zhang, W. *J. Am. Chem. Soc.* **2017**, *139*, 17082-17088.
31. Mullangi, D.; Dhavale, V.; Shalini, S.; Nandi, S.; Collins, S.; Woo, T.; Kurungot, S.; Vaidhyanathan, R. *Adv. Energy Mater.* **2016**, *6*, 1600110.
32. Pachfule, P.; Kandambeth, S.; Diaz, D.; Banerjee, R. *Chem. Comm.* **2014**, *50*, 3169-72.
33. Shi, X.; Yao, Y.; Xu, Y.; Liu, K.; Zhu, G.; Chi, L.; Lu, G. . *ACS Appl. Mater. Interfaces* **2017**, *9*, 7481-7488.

34. Chen, L.; Zhang, L.; Chen, Z.; Liu, H.; Luque, R.; Li, Y. *Chem. Sci.* **2016**, 7, 6015-6020
35. Chen, G. J.; Li, X. B.; Zhao, C. C.; Ma, H. C.; Kan, J. L.; Xin, Y. B.; Chen, C. X.; Dong, Yu. B. *Inorg.Chem.* **2018**, 57, 2678-2685.
36. Aiyappa, H. B.; Thote, J.; Shinde, D. B.; Banerjee, R.; Kurungot, S. *Chem. Mat.* **2016**, 28, 4375-4379.

Chapter-2

Synthesis and Catalytic Studies of Pd(0) loaded N-rich Triazine COF for Multi-fold Heck Couplings, Suzuki Couplings and CO Oxidation Reactions



2.1. Introduction

Covalent Organic Frameworks (COFs) are being researched widely as candidate materials for applications requiring high surface areas and porosities¹. Condensation reactions between a variety of functional groups have resulted in a number of COFs². Some of the earliest reported COFs are based on Schiff bases³, formed by reacting amines with aldehydes. They form ideal targets for ready reactions under relatively mild conditions and tend to form well-defined hexagonal honeycomb layers and also high symmetry three-dimensional structures depending on the geometry of the building units. Presence of organic backbones in the COFs favors the introduction of specific functionalities by design. Moreover, it has been well demonstrated in coordination chemistry that the imine type (Schiff base) ligands are versatile in incorporating a variety of metal ions. However, the Schiff bonds need to be proximal to each other for efficient interaction with metals⁴. This requirement poses a constraint in using longer or bulkier molecules in forming the COF, as they would naturally space out the Schiff bonds. There are two solutions to overcome this, one comes from structural part: the bulkier and longer units in the COF could find efficient packing when coupled with flexible functional groups (e.g ether, ester, amide), thus favoring Schiff bonds from adjacent layers to orient proximally. Another is from introducing any N-rich monomers such as triazine derivatives, which could serve as strong interactions sites for the metal nanoparticles. Amorphous polymers built from triazine cores are known to interact well with catalytically active noble metals, thus preventing catalyst leaching⁵.

The possibility of forming a variety of products based on a general synthetic methodology has made the metal-catalyzed Heck couplings and boronic acid based C-C bond formations (Suzuki coupling) two of the most important organic reactions⁶. Polymeric solids based on ion-exchange resins⁷, polystyrene⁸, polymethylacrylate derivatives⁹, covalent organic frameworks^{4,10}, and metal organic frameworks¹¹ have recently been explored as supports for catalytic metal nanoparticles. Yet, the commercial productions still predominantly utilize homogeneous molecular Pd²⁺ based catalysts, owing to their ability to provide and operate in non-polar solvent environment required which favor formation of products in high yields. In fact, many of the above referred polymers are rich in sp² carbon capable of providing apolar environment and stabilizing geometries of the catalyst and transition states. An inherent compromise that is being made during the use of C-rich supports is the creation of weaker

interactions with the catalyst nanoparticles, particularly in the case of Pd⁰. This could have immediate implications on the catalyst leaching from the support¹². Thus, there is a need for developing a heterogeneous catalyst that can provide sp² center rich environments and have strong interactions with both Pd²⁺ and Pd⁰ and at the same time be optimally polar. Stronger Pd⁰ triazine interactions could be crucial to preventing the Ostwald ripening of the nanoparticles. In fact, triazine based polymer has been shown to interact well with Palladium^{5, 13}.

Here, we have synthesized a Nitrogen rich, triazine based covalent organic framework (IISERP-COF1) pre-disposed for 'single-step' loading of Pd⁰ nanoparticles. Triazine mimics basic pyridyl groups capable of assisting Pd²⁺ to Pd⁰ reduction in an alcoholic medium and also creates strong interactions with Pd nanoparticles. These pyridyl centers can bind equally well with Pd²⁺ as well as Pd⁰ species. Additionally, the ether bonds along with the sp² rich non-polar phenyl framework and Schiff linkages serve as an apolar matrix mimicking the environment present typically in homogeneous molecular catalysts. Pd@IISERP-COF1 exhibits good hydrolytic stability, facile handling and recovery and excellent recyclability for a vast library of Heck type reactions and C-C bond formation reactions. Specifically, we have studied the simultaneous or multi-fold Heck couplings on a substrate (up to six-fold substitution) which is generally quite difficult to achieve¹³. Also studied the ability of Pd@IISERP-COF1 to mimic a truly industrial catalyst, it was employed as a catalyst in the widely studied CO oxidation reaction. This CO to CO₂ oxidative conversion finds application in air cleaning, automobile catalytic converters, and in the cleaning of fuel cell feeds¹⁴. Considering the mere cost of noble metal catalysts still there is a need to bring down the catalyst concentration in reactions and also increase its durability and recyclability.

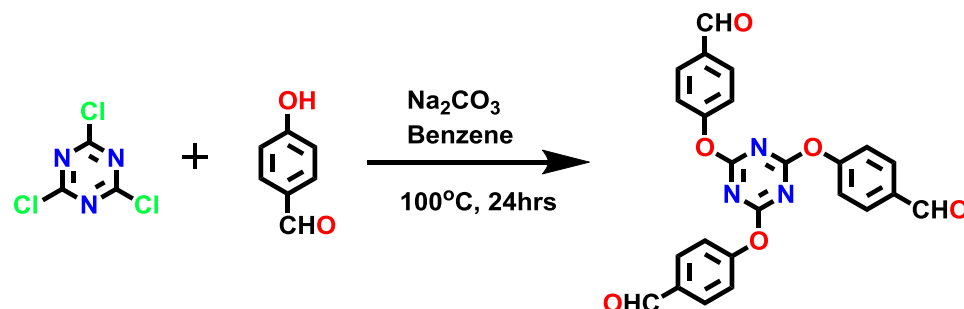
2.2. Experimental details

2.2.1 Materials and Measurements

X-ray powder diffraction (XRD) is carried out using a Rigaku Miniflex-600 instrument and processed using PDXL software and for some cases Bruker Discover. Thermogravimetry was carried out on NETSZCH TGA-DSC system. The routine TGAs were done under N₂ gas flow (20ml/min) (purge + protective) and samples were heated from RT to 500°C at 2K/min. FEI (model Tecnai F30) high resolution transmission electron microscope (HRTEM) equipped

with field emission source operating at 300 KeV was used. X-Ray photoelectron spectroscopic (XPS) measurements were carried out on a VG Micro Tech ESCA 3000 instrument at a pressure of $>1 \times 10^{-9}$ Torr (pass energy of 50 eV, electron take-off angle of 60° , and an overall resolution was 0.1 eV). Field Emission Scanning Electron Microscope with integral charge compensator and embedded EsB and AsB detectors. Oxford X-max instruments 80mm^2 . (Carl Zeiss NTS, Gmbh), Imaging conditions: 2kV, WD=2mm, 200kX, Inlens detector. FT-IR spectra were recorded on NICOLET6700 FT-IR Spectrophotometer using KBr Pellets.

2.2.2. Synthesis of Trialdehyde Monomer



2,4,6-Tris(p-formylphenoxy)-1,3,5-triazine was synthesized with slight modification to the reported procedure¹⁵. 1.5 g of Cyanuric chloride and 4g of p-hydroxybenzaldehyde were added to a suspension of Na_2CO_3 (30 g) in 150 mL of benzene. The resulting mixture was refluxed at 100°C for 24 hrs. After 24hrs, the hot reaction mixture was filtered and washed with an excess of hot ethylacetate and filtrate was extracted with 10% Na_2CO_3 . The subsequent organic layer was dried with anhydrous Na_2SO_4 and evaporated using rota evaporator to obtain a white powder of the desired compound (72%). The product was characterized using NMR, HRMS and the characterization results were found to be are consistent with the literature reports. All p-Phenylenediamine and organic chemicals were purchased from Sigma Aldrich and used without any further purification.

2.2.3. Synthesis of IISERP-COF1

2,4,6-Tris(p-formylphenoxy)-1,3,5-triazine (TRIPOD aldehyde) (100 mg, 0.23mmol) 1,4-diaminobenzene (48 mg, 0.46mmol) were dissolved in 1,4-dioxane (5.0 mL) in a Pyrex tube. To this mixture, mesitylene (5.0mL) was added and the contents were homogenized by stirring. Following this, about 0.5 mL of 3M aqueous acetic acid was added. Then the Pyrex tube was flash-frozen in a liquid nitrogen bath, the free space was evacuated and the tube was closed

under a blanket of nitrogen. The tube was placed in an oven at 120 °C for 3 days. A brown solid was obtained, which was washed with DMF, dioxane, acetone and THF to remove any unreacted monomers or oligomers. The reaction yielded 110 mg (87%) of IISERP-COF1. Activation of the sample for gas adsorption was done by soaking the sample in THF for 3 days with three time replenishment of the solvent. (CHN Analysis: Observed. C = 66.9; H = 3.74; N = 17.38. Calculated. 70.9; H = 5.41; N = 15.04, (Note: the CHN values have been calculated using a COF unit constructed with a trialdehyde monomer and phenylenediamine with a ratio of 2:3.

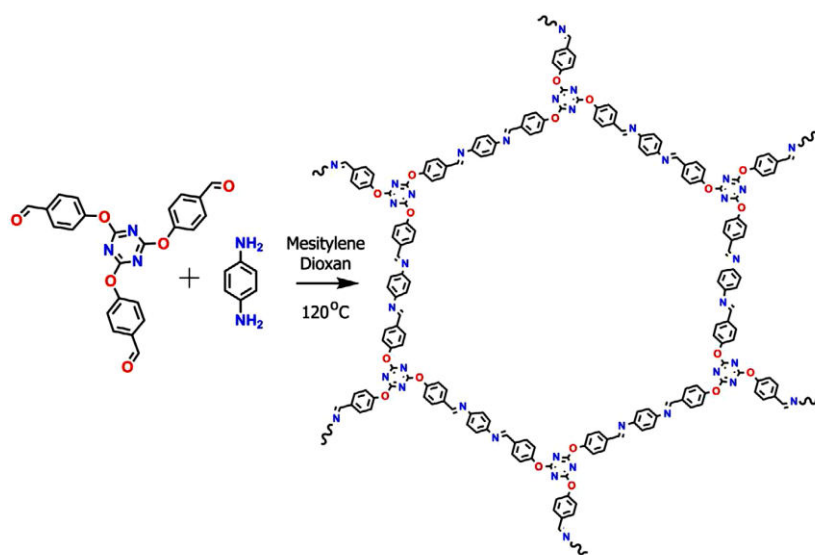


Figure 2.1. Schematic representation of the IISERP-COF1 synthesis and proposed topology.

2.2.4. Synthesis of Pd@IISERP-COF1

Palladium acetate (36 mg) is dissolved in 10 mL of Acetone and the IISERP-COF1 (100 mg) dispersed in 20mL of ethanol. To this ethanolic suspension of IISERP-COF1, an acetic solution of Pd(OAc)₂ was added using a syringe needle over 30mins. A rigorous stirring was maintained throughout the addition. The mixture was allowed to stir for 24 hrs at room temperature. The resulting black solid was filtered and washed with acetone, ethanol and THF, then dried over vacuum for 12hrs. From the CHN analysis we observed that ~3.6wt% of Pd(0) is presented in the Pd@IISERP-COF1 (CHN Analysis: Observed. C = 43.3; H = 2.6; N = 11.6. Calculated. (Formula: Pd@IISERP-COF1.(Pd)_{3.6}: 42.3; H = 3.06; N = 9.1). now onwards palladium nanoparticles loaded on the COF has been named as Pd@IISERP-COF1.

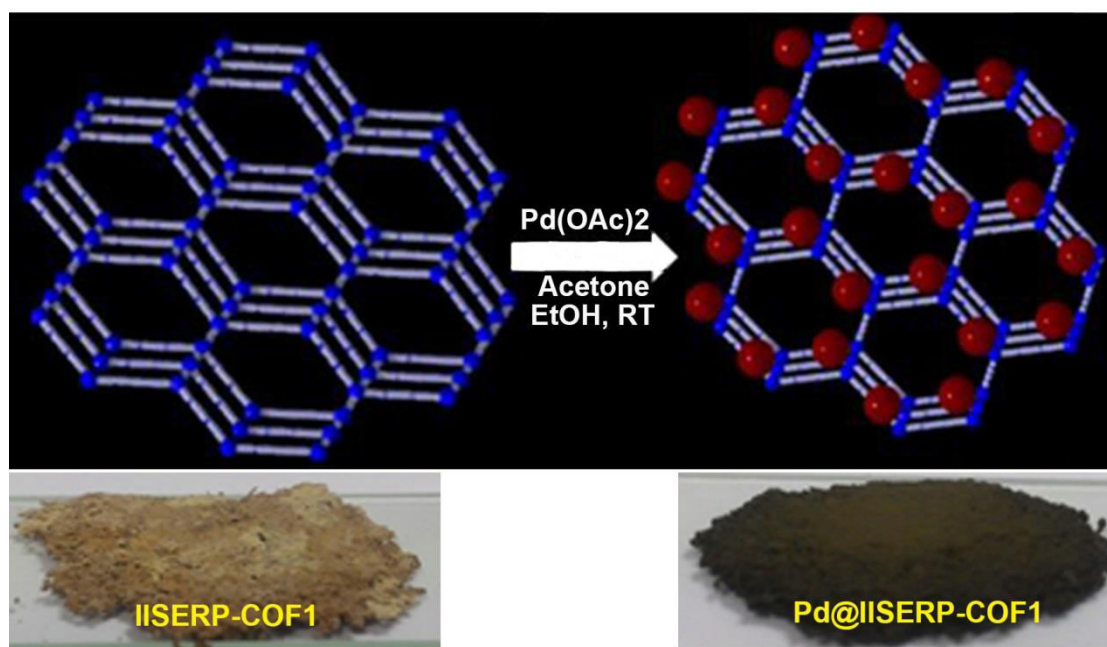
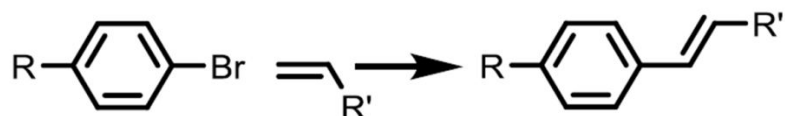


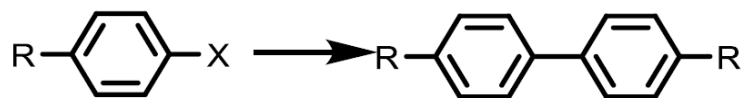
Figure 2.2. Schematic illustration of Pd nanoparticle loading and their photographic images before and after loading of Pd nanoparticles.

2.2.5. General Procedure for the Heck Reaction



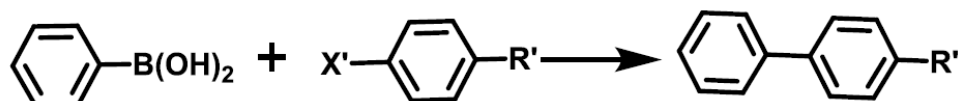
Aryl halide (1.0 mmol), butyl acrylate or styrene (1.1 mmol), sodium acetate (1.2 mmol), and Pd@IISERP-COF1 (1mg) were added to 3ml of N-Methyl-2-pyrrolidone (NMP). The reaction mixture was stirred at 120°C for 1hr in the open air, whereas in the case of di to hexabromo coupling, the reactions were carried out over 6-10 hrs and 3 to 5mg of the catalyst was used. At the end of the reaction (monitored from TLC), the reaction mixture was poured into water and extracted with dichloromethane and evaporated under reduced pressure. Products were purified by column chromatography and characterized by using NMR spectroscopy. For the recyclability tests, a reaction involving p-nitrobromobenzene (101 mg, 0.5 mmol), n-butylacrylate (74 mg, 0.575 mol), sodium acetate (51mg, 0.625 mmol), and Pd@IISERP-COF1 (0.5 mg) in 3mLof NMP was considered. In the recyclability studies, the reaction mixture was centrifuged and the catalyst was recovered used directly without any further treatment.

2.2.6. General Procedure for the Ullmann type (C-C) Coupling



Aryl halide (0.5mmol), Potassium Carbonate (0.6mmol), and Pd@IISERP-COF1 (2mg.) were added to 3ml of dimethylformamide. The reaction mixture was stirred at 120°C for 6hrs in an open atmosphere. After completion of the reaction (monitored by TLC), the reaction mixture was poured into water and extracted with dichloromethane (DCM). The DCM was evaporated under reduced pressure. Products were purified by column chromatography and characterized by using NMR spectroscopy, HRMS. Some of them were isolated as single crystals and characterized using SC-XRD.

2.2.7. General Procedure for the Suzuki Coupling Reaction



Aryl halide (1.0 mmol), phenylboronic acid (1.1 mmol), sodium hydroxide (NaOH) (1.2 mmol), Tetra-n-butylammonium bromide (TBAB) (1.2 equiv), 1mg of Pd@IISERP-COF1 were added to 3mL of water. The reaction mixture was stirred at 65°C for 4hrs in the open air. After completion of the reaction, the reaction mixture was poured into water and extracted with DCM and the organic layer was evaporated under reduced pressure. Products were purified by column chromatography and characterized by using NMR spectroscopy, HRMS and in some cases using SC-XRD.

2.2.8. CO to CO₂ Oxidation- Experimental Conditions

The catalytic activity of Pd@IISERP-COF1 catalyst for CO oxidation was measured in a fixed bed reactor under atmospheric pressure using 100 mg pelletized catalyst. The temperature was ramped between 30°C to 300°C at 2°/min ramping rate. The total flow rate was 50 ml/min with a ratio of (1:5:19 CO:O₂:N₂). The calculated GHSV was 30000 cm³/gcat/hr. The temperature of tubular furnace where the reactor was mounted was controlled by Radix6400 temperature controller and the catalyst bed temperature was measured by a K-type thermocouple. The effluent gases were analyzed online by a gas chromatograph equipped with an online gas sampling valve and a TCD detector. The activity was examined by looking at the CO conversion.

$$\text{CO conversion (\%)} = \frac{\text{CO}_{\text{initial}} - \text{CO}_T}{\text{CO}_{\text{initial}}} \times 100$$

Where CO_T is the amount of consumed at a particular temperature (T).

2.3. Structure Solution and Description

The powder XRD of the IISERP-COF1 was indexed using an X-Cell program from the Materials Studio. Following a profile fit, the space groups search was carried out using *Pawley* routine. The space groups P6/m and P6/mcc were identified with well-acceptable Figure of Merit (FOM > 20), of which the P6/mcc had the highest value. The powder pattern was analysed, both P6/mcc and P6/m (Fig. 2.3) (P6/mcc: $\chi^2 = 3.512$; $R_p = 0.0264$; $wR_p = 0.0336$) and P6/m: $\chi^2 = 3.406$, $R_p = 0.0230$; $wR_p = 0.0320$). When a Pawley fit was carried out in both space group settings, they both had good statistics (P6/m: $R_p = 2.59$, $wR_p = 3.51$, P6/mcc: $R_p = 2.86$, $wR_p = 4.01$) (Figure. 2.3c). Other space groups such as P3, P-3 produced a structure consistent with the experimental powder pattern, but were not considered as they merely represent the lower symmetry sub-groups. It was difficult to differentiate between the two space groups, P6/m and P6/mcc, based on relative intensities. The major differentiating region in the PXRD was between 2θ of 12° to 16° , a comparison of the simulated patterns in this region with the experimental one showed relatively better fit for P6/mcc (Figure Apex 2.1A). Additionally, the energies associated with P6/m (~ 174 Ha) and P6/mcc (~ 348 Ha), estimated from the Tight Binding Density Functional Theory routine (DFT-TB), also supported the P6/mcc was the favorable structure. This could be due to the higher packing efficiency in the latter space group. Thus, we propose the most favorable structure as being P6/mcc with an *ABAB...* stacking, giving an interlayer separation of 6.8 \AA . Pawley refinements carried out using the *Materials Studio (version 8.0)* gave an excellent fit and all the visible low angle peaks could be assigned. The *002* peak, corresponding to the interlayer spacing of 3.4 \AA is observed at $2\theta = 26.2^\circ$ (Figure Apex 2.1B).

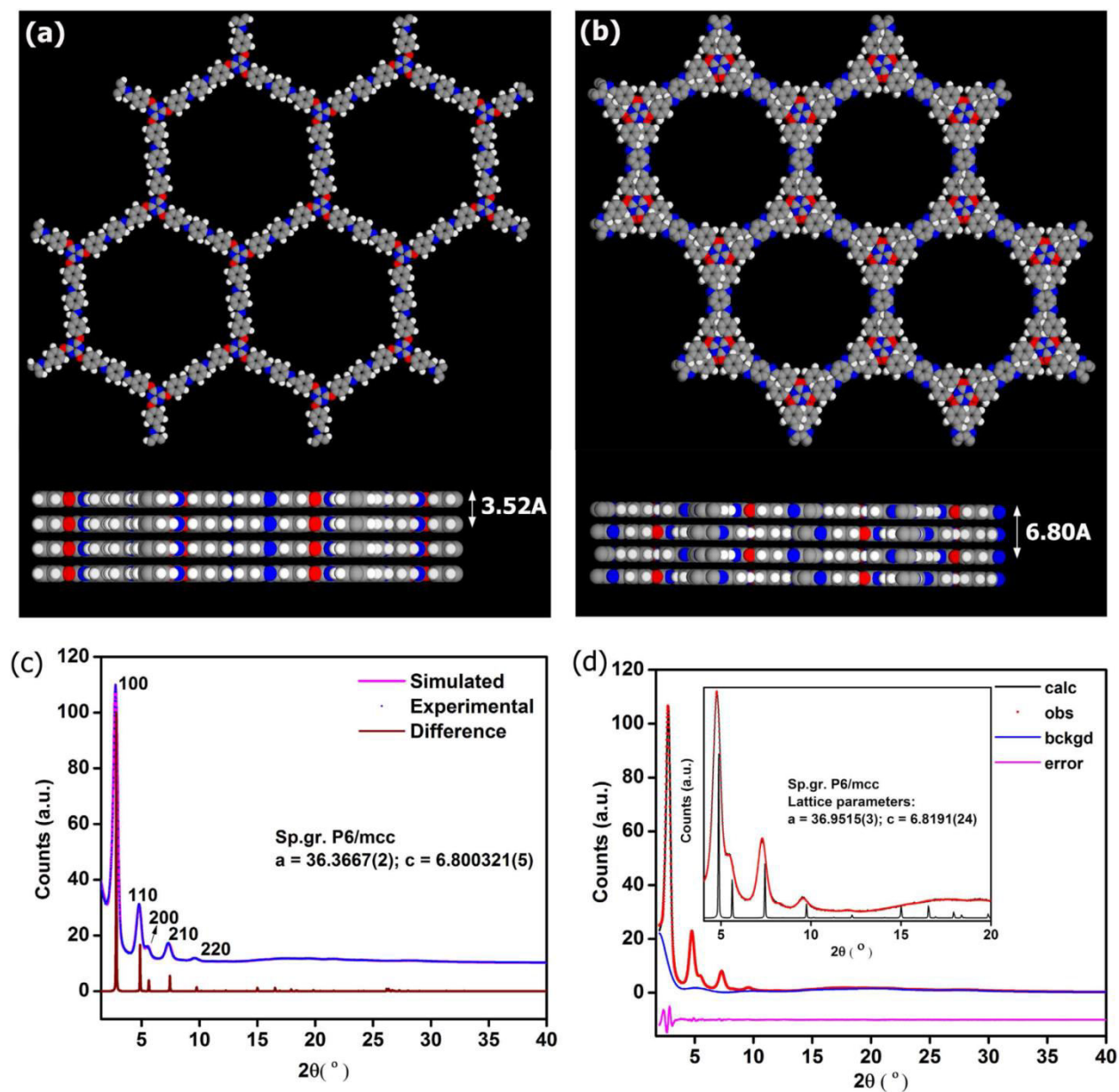


Figure 2.3. (a) Hexagonal honeycomb layers of IISERP-COF1 in P6/m setting, with large 1D pores (34 Å) and the AA... type stacking with an interlayer separation of 3.52 Å. (b) Circular channels (29 Å) created by the stacking of hexagonal layers in P6/mcc setting. The stacking is of ABAB... arrangement with a C-axis length of 6.80 Å. (c) A Pawley fit in P6/mcc setting. The statistics associated were good and comparable to those obtained for P6/m setting. (d) A Le bail fit for the COF in P6/mcc ($\chi^2 = 3.512$; $R_p = 0.0264$; $wR_p = 0.0336$). The inset shows the goodness of the fit with markers for P6/mcc. It also shows the lack of many peaks in the 2θ range of 12-16°, where P6/m would have more peaks than P6/mcc. Color code: O- red; N- blue; C- grey and H- white.

2.4. Results and Discussion

Both the as made IISERP-COF1 and the palladium loaded COF (Pd@IISERP-COF1) were characterized unambiguously through PXRD, TGA, SSNMR IR, XPS, FE-SEM, and TEM analysis. The PXRD pattern of the Pd@IISERP-COF1 matches quite well with that of the as-synthesized COF and displays characteristic higher angle signals at 2θ of 39° and 45° corresponding to the palladium nanoparticles presented in the frameworks, these peaks are assigned to be (111), (200) planes of the Pd(0) (ICSD 064918) (Figure 2.4a). Noticeably, the Pd peaks were quite broad indicating their nanoparticle nature. The TGA plot of the of Pd@IISERP-COF1 shows a continuous and gradual weight loss above 140°C (Figure 2.4a and Appendix 2.2). The IR spectra of Pd@IISERP-COF1 matches well with IISERP-COF1 and revealed characteristic stretching frequency for the triazine core (C=N) at 1570 cm^{-1} and no noticeable carbonyl stretching bands were observed further indicating the lack of any palladium (II) acetate (Appendix 2.3a). Surface area and pore size distribution of IISERP-COF1 and Pd@IISERP-COF1 were determined using N_2 adsorption isotherm measured at 77K. It is quite unusual IISERP-COF1 did not lose any N_2 uptake upon Pd^0 loading unlike other Pd^{2+} loaded COFs¹⁰ (Fig. 2.5a). This could suggest the presence of only Pd^0 in our COF as it occupies much lesser pore space than $\text{Pd}(\text{OAc})_2$ and even while sitting on the surface of the COF, owing to its

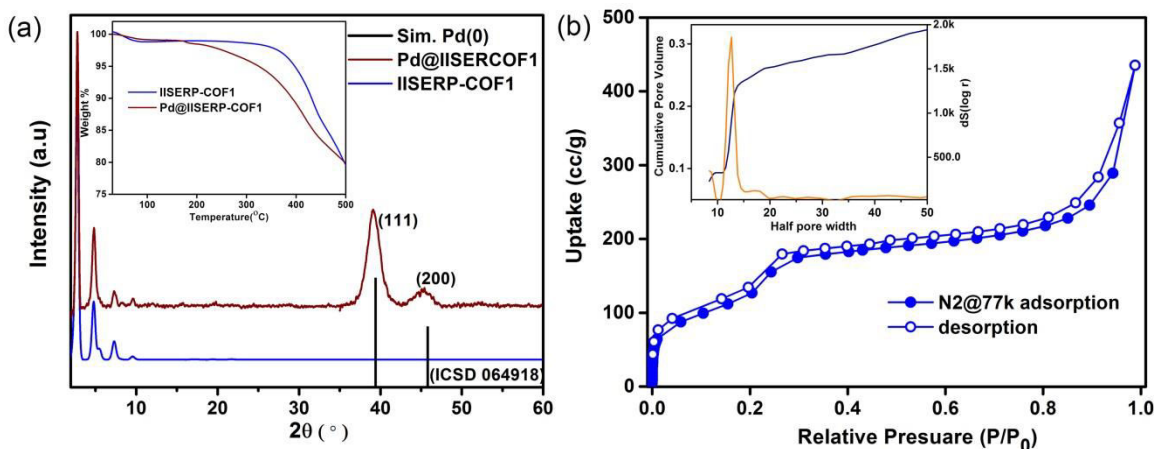


Figure 2.4. (a) PXRD of Pd@IISERP-COF1 shown retention of low angle peaks and two broad signals at 39° and 45° (2θ) these broad signals at higher angles were assigned to be (111) and (200) planes of Pd(0) nanoparticles loaded in the COF. Inset shows TGA spectra of both the COFs. (b) Nitrogen adsorption isotherm of IISERP-COF1 and inset shows pore size distribution of the same.

smaller size, would be expected to create less impediment to the pore access. A Non Localized Density Functional Theory (NLDFT) fit to the isotherm showed the presence of micro and mesopores, with micropores being in minor concentration. The as-synthesized form of IISERP-COF1 has a BET surface area of 408.5 m²/g, while the Pd@IISERP-COF1 possessed a BET surface area of 404 m²/g. Considering this unusual case, wherein there is not much of a loss of surface area upon Pd loading, a non-model dependent fit, Barrett-Joyner-Halenda (BJH), was also used to obtain the pore size. The as-synthesized form had mesopore of 23 Å, while the Pd loaded form had 19 Å pores. While the Dubinin-Radushkevich (DR) model gave a pore volume of 0.21cc/g and a surface area of 563 m²/g. The IISERP-COF1 showed pore sizes of 12.7 and 27 Å, the Pd@IISERP-COF1 showed pore sizes of 18 and 27 Å with exactly same ratio. Seeing this unusual N₂ uptake of Pd@IISERP-COF1 we have repeated the experiments on multiples of batches and activating them at various temperatures (120^oC, 150^oC, 180^oC) still, it did not result in any change in the profiles or uptakes of the N₂ isotherms (Appendix 2.3b). The XPS analysis of Pd@IISERP-COF1 shows presence of only Pd(0) nanoparticle and their respective binding energies (Pd-3d^{5/2} =334.7 and Pd-3d^{3/2} =339.9) (Figure 2.5b). The peaks expected for the other elements carbon, nitrogen and oxygen are consistent with the literature¹⁶.

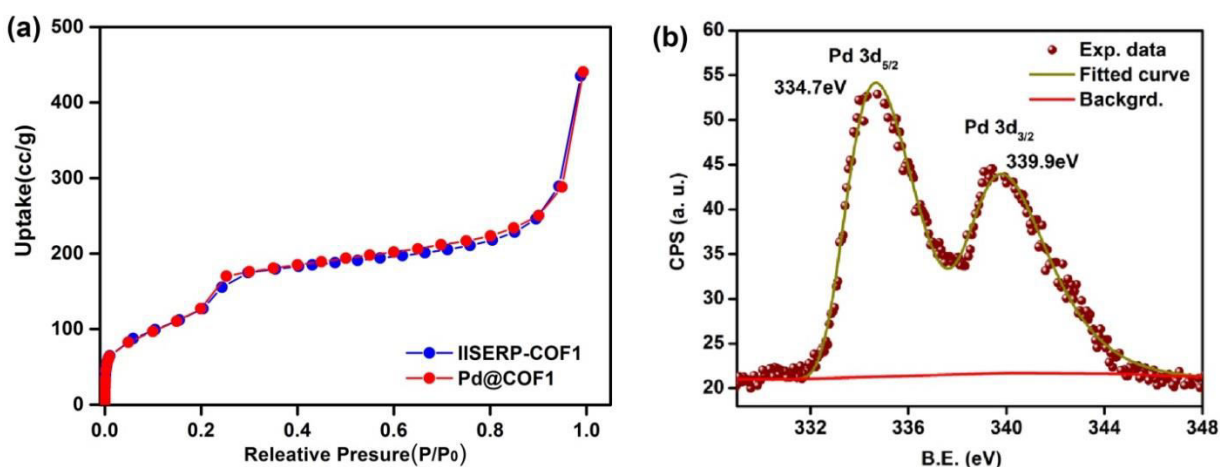


Figure 2.5. (a) Comparison of N₂ isotherm of Pd loaded IISERP-COF1 (Pd@IISERP-COF1) and as made IISERP-COF1. (b) XPS spectra of Pd@IISERP-COF1 showing the presence of Pd(0) and these binding energies concorded with literature.

FE-SEM analysis of the Pd@IISERP-COF1 shows the presence of highly dispersed loading and they have the particles with sizes ranging from < 5 to 20 nm (Fig. 2.6b). Being able

to image Palladium (Pd) on COF with such clarity from FE-SEM is quite remarkable. A high magnification image of FE-SEM shows the presence of patterned surfaces and the Pd nanoparticles are uniformly distributed over them without any aggregation. Further, the HR-TEM images showed an even distribution of Pd nanoparticles with the particle sizes in the range of 5–20 nm and few with sizes < 5 nm could also be seen (Figure 2.5 c-d).

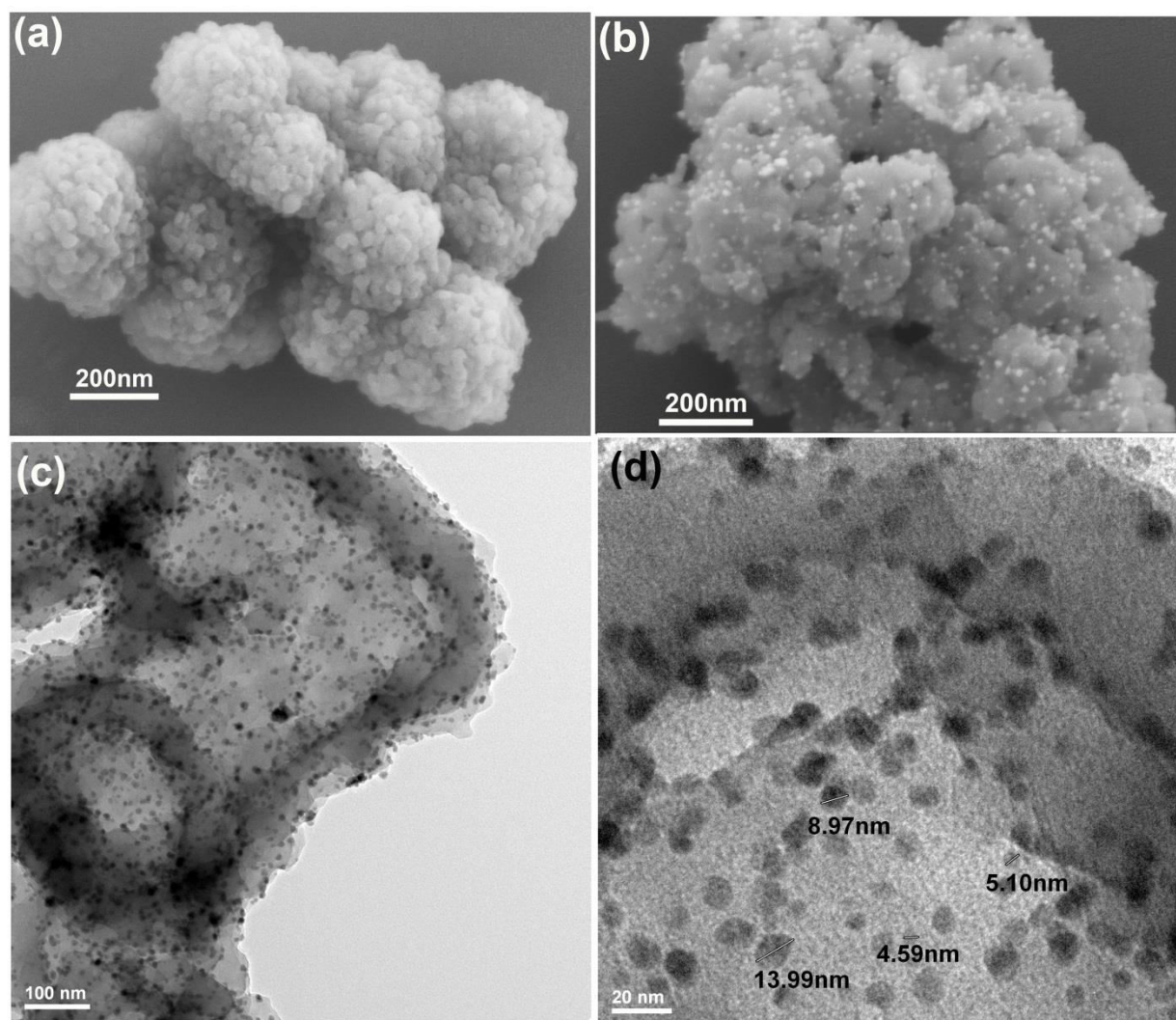
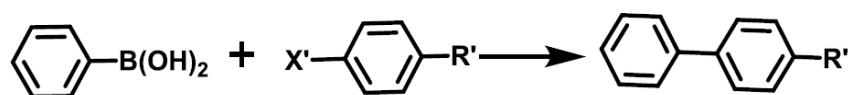


Figure 2.6. (a-b) FE-SEM image of the as made IISERP-COF1 and Pd@IISERP-COF1 showing the uniform morphology of the COF and the homogeneous loading of Pd⁰ nanoparticles. (c-d) HR-TEM image of the as-synthesized COF showing the thin transparent layers formed by the COF and a high resolution TEM image of the Pd@IISERP-COF1 is showing the presence of small nanoparticles of Pd⁰ (< 5 to 20 nm).

2.5. Catalytic Studies of Pd@IISER-COF1 Catalyst

2.5.1. Suzuki-Miyaura Coupling Reactions

To evaluate the catalytic activity of Pd@IISERP-COF1 we have carried out Suzuki-Miyaura coupling reactions using boronic acid and aromatic halides. The catalyst showed excellent activity (yields up to 99%) for all the donating, withdrawing substituents and yielded high TON (up to 2500) and TOF (up to 2500) Table 2.1. The catalyst concentration employed is comparable to the ones observed in some of the homogeneous Heck catalysts optimized over 20 years¹⁷. Also comparable to the some of the lowest catalyst concentrations employed during Suzuki couplings. For example, Pd doped quaternary systems with perovskite structures (TON= 27000)¹⁸. Further, the catalysts did not show any appreciable loss of activity for all three class of reactions when tested over four cycles (Figure 2.9).

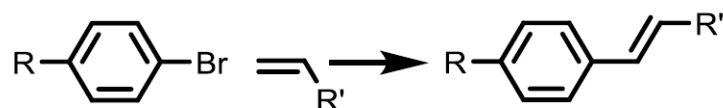


Entry	X	RR	%yield	TON	TOF(h ⁻¹)
1	I	H	99	2604	651
2	Br	H	98	2578	645
3	I	COMe	99	2604	651
4	Br	COOMe	99	2604	651
5	I	NO ₂	99	2604	651
6	Br	OMe	99	2604	651

Table 2.1. Suzuki-Miyaura coupling reactions of various substrates and their isolated yields. Reaction condition: Aryl halide (1.0 mmol), phenylboronic acid (1.1 mmol), NaOH (1.2 mmol), tetra-n-butylammonium bromide (TBAB) (1.2 equiv), 0.01mol% of Pd@IISERP-COF1 were added to 3mL of water. Contents were stirred at 65°C for 4hrs in the open air.

2.5.2. Heck Coupling Reactions

We also extended our studies on highly demanding Heck coupling reactions and observed that our catalyst showed superior performance than reported values (Table 2.2)¹⁰. Encouraged by these results, we further extended our studies to very challenging multisite Heck coupling reactions.



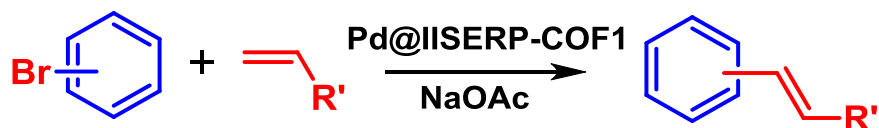
Entry	R	R'	% yield	TON	TOF(h ⁻¹)
1	H	CO ₂ n-Bu	82	2473	2473
2	CH ₃	CO ₂ n-Bu	85	2394	2394
3	OCH ₃	CO ₂ n-Bu	80	2262	2262
4	CN	CO ₂ n-Bu	92	2420	2420
5	NO ₂	CO ₂ n-Bu	93	2446	2446
6	H	Ph	85	2500	2500
7	OCH ₃	Ph	88	2315	2315
8	CN	Ph	88	2288	2288
9	NO ₂	Ph	91	2394	2394

Table 2.2. Heck reactions on substrates with electron withdrawing or electron donating substituents. Amount of catalyst used in each reaction is 1mg for 1.0mmol of reactant, reaction time 1hr at 120 °C, condition: Aryl halide (1.0 mmol), butyl acrylate or styrene (1.1 mmol), sodium acetate (1.2 mmol), and Pd@IISERP-COF1 (~0.01 mol%) were added to 3ml of N-Methyl-2-pyrrolidone (NMP).

2.5.3. Multi-fold Heck Coupling Reactions

One of the major challenges in Heck type reactions is in achieving simultaneous multi-fold substitution to synthesize multi-functionalized final products in pure form with high yields. Typically, this kind of reactions are carried out using a homogeneous catalyst such as highly functionalized Pd complex and with high catalyst concentrations. Owing to multiple steps complex synthesis and poor selectivity of homogeneous counterparts, there is an instant need of a highly active heterogeneous catalyst. Our fissile one-pot loaded Pd@IISERP-COF1 catalyst displays remarkable selectivity and excellent activity (isolated yield 80% to 95% with high TON up to 2500) for the multi-fold Heck coupling reactions Table 2.3. Most of these multi-fold coupling products were used in a wide range of materials synthesis as ligands or monomers. Of particular mention is the products, biphenyl-4,4'-dicarboxylic acid (bpdc), 3,3',5,5'-biphenyltetracarboxylic acid, 1,3,6,8-tetra(styryl)pyrene shown in Table 2.3. The bpdc is a commercially sold and widely used organic ligand in the formation of MOFs and other advanced

materials. Another product, the styryl-pyrene could serve as an excellent monomer for developing functional polymers.



Entry	R ₁	R ₂	Product	% yield	TON	TOF(h ⁻¹)
1		 R'=CO ₂ nBu, Ph	 R'=CO ₂ nBu, Ph 1a 1b	85 (1a) 82 (1b)	2473 2500	2473 2500
2		 R'=CO ₂ nBu, Ph	 R'=CO ₂ nBu, Ph 2a 2b	94 (2a) 90 (2b)	824 789	824 789
3		 R'=CO ₂ nBu, Ph	 R'=CO ₂ nBu, Ph 3a 3b	95 (3a) 91 (3b)	500 478	84 79
4		 R'=CO ₂ nBu, Ph	 R'=CO ₂ nBu, Ph 4a 4b	96(4a) 97(4b)	509 510	84 85
5		 R'=CO ₂ nBu, Ph	 R'=CO ₂ nBu, Ph 5a 5b	91(5a) 86(5b)	478 452	80 76

Table 2.3. List of Heck coupling reactions catalyzed by Pd@IISERP-COF1. Typical reaction condition: Aryl halide (1.0 mmol), butyl acrylate or styrene (1.1 mmol), sodium acetate (1.2 mmol), and Pd@IISERP-COF1 (0.01-0.06 mol%) were added to 3ml of N-Methyl-2-pyrrolidone. % of yield = (Actual weight of the yield/predicted weight of the product)*100 ; TON (Turnover number) calculation = moles converted / moles of active sites; TOF (Turnover frequency) = TON/Time hours.

2.5.4. CO Oxidation Reaction

Motivated by the above results, the CO oxidation activity test was carried out to assess the ability of Pd@IISERP-COF1 catalyst for catalyzing gas phase reaction. Figure.2.7 shows the CO conversion plot for the catalyst during the two cycles of activity testing. During the first run the oxidative conversion showed an onset temperature of 100 °C with a full conversion at 180 °C. The time on stream (TOS) data showed that there was no loss in activity over an extended period of time. The second cycle of the catalyst again proved their stability, where it showed a light-off temperature of 140°C and a drastic increase in activity to full conversion at 160°C. This study implies that COFs can mimic the performance of true industrial catalyst working under harsh conditions without any appreciable loss of activity. The Pd@IISERP-COF1 did not show any substantial interaction with H₂ at 77 K or 303 K and O₂ at 273 K or 303 K, as observed from respective adsorption measurements, which indicate an apparent stronger chemical interaction of the catalyst with CO over these gases.

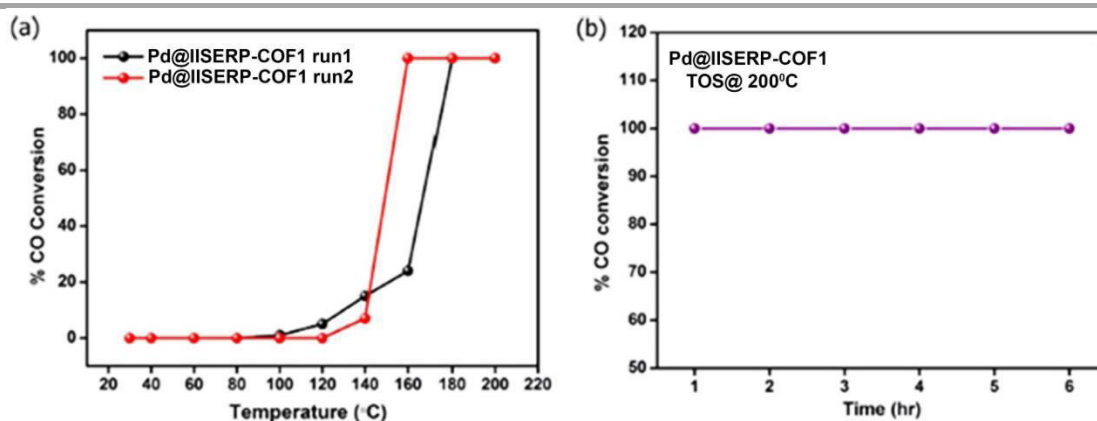


Figure 2.7. (a) The CO conversion plot for Pd@IISERP-COF1 for two cycles of activity testing. (b) Time of stream plot of Pd@IISERP-COF1 at full conversion.

2.5.5. Recyclability and Durability Studies

The stability and durability of the catalyst are crucial for the true industrial catalysts especially to qualify for any commercial use. Here, the durability studies of Pd@IISERP-COF1 have been performed for all the Suzuki-Miyaura, the Heck, and the multi-fold coupling reactions (Figure.2.8a). Remarkably Pd@IISERP-COF1 catalysts did not loss of any activity even after three consecutive cycles and retain its high yields (95-98%). These results clearly reflect the true heterogeneous nature and recyclability of the Pd@IISERP-COF1 catalyst (Figure. 2.8a).

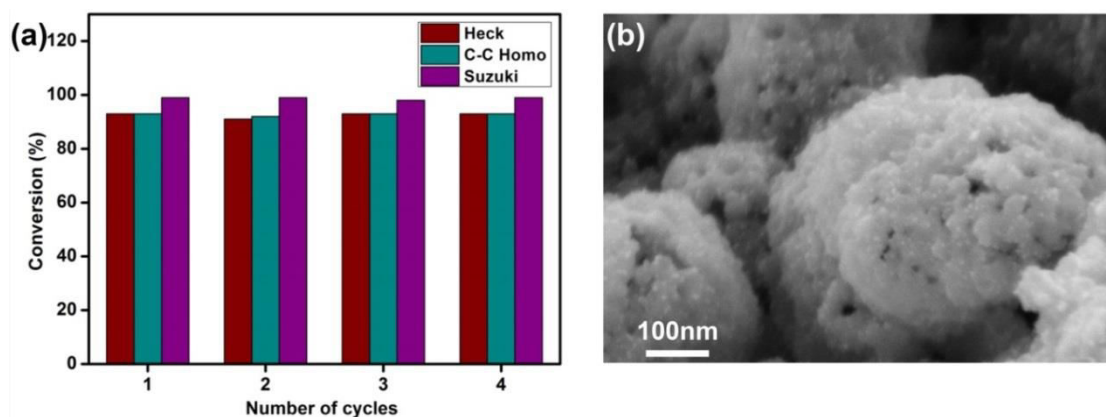


Figure 2.8. (a) A bar chart showing the yield of products obtained via either Heck, non-boronic acid based C-C homo coupling and boronic acid based Suzuki coupling using some representative reactions. In these recycle tests, a reaction involving p-nitrobromobenzene (101 mg, 0.5 mmol), n-butylacrylate (74 mg, 0.575 mol), sodium acetate (51mg, 0.625 mmol), and Pd@IISERP-COF1 (0.5 mg) in 3mL of NMP was used as a representative. (b) SEM image of the Pd@IISERP-COF1 post catalysis. Note the fine dispersion of the Pd nanoparticles and there seems to be no aggregation or sintering even upon heating.

After reaction, the catalyst was recovered by simple filtration and supernatant solution is subjected to SEM-EDX elemental analysis to find any trace quantity of Pd nps leaching. Interestingly EDX analysis displays no signal corresponding to Pd nanoparticles. The FE-SEM images of post catalyst show retention of pristine morphology (Figure. 2.8b). Further, the XPS spectra and PXRD pattern of the spent catalyst shows retention of Pd(0) and crystallinity indicating no morphological and structural changes occurred during catalysis.

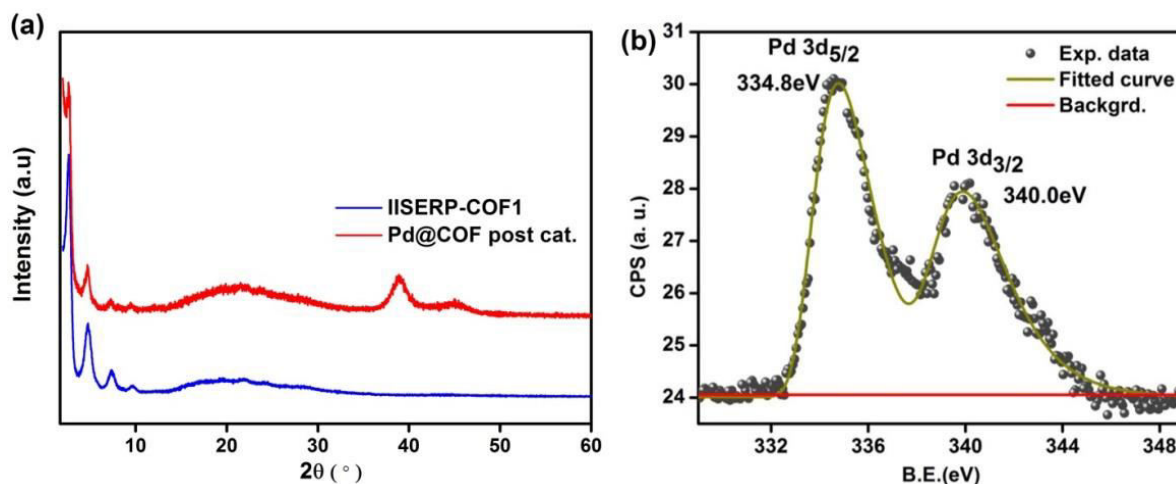


Figure 2.9. (a) The PXRD of spent catalyst showing no considerable change in crystallinity and Bragg's position compared with as made COF. (b) XPS spectra of spent Pd@IISERP-COF1 catalyst displays retentions of Pd(0) binding energies.

To explore the origin of favorable COF-Pd(0) nanoparticles interactions at the surface of the IISERP-COF1, theoretical modeling studies and a series of vapor sorption measurements have been carried out. Water showed a near-linear isotherm with no appreciable concavity or convexity, indicating the lack of any strong interaction with the surface. While the non-polar toluene showed much more abrupt uptake and concavity towards the pressure axis indicating stronger interactions, while methanol has the most abrupt uptake at low P/P_0 compared to toluene or water. This is an indication of stronger interaction particularly at lower pressures, which is reflected in a very strong heat of adsorption for methanol at the zero-loading. This suggests the surface is considerably polar and hydrophobic, thus showing an ‘*amphiphilic*’ nature. And, in spite of having ether group lining and relatively non-polar groups on the walls of the pore, IISERP-COF1 did not show much selectivity between methanol and toluene. This is further confirmed by the heats of adsorptions calculated using a virial model (Figure 2.10). Water had the least value (40 kJ/mol), which is just above the vaporization point of water¹⁹ suggesting very weak interactions, while toluene showed an HOA of 80 kJ/mol and methanol seems to interact the best with the surface with a value of 100 kJ/mol. These observations were in accord with the amphiphilic nature verified from the contact angle of $90 \pm 2^\circ$ for the IISERP-COF1.

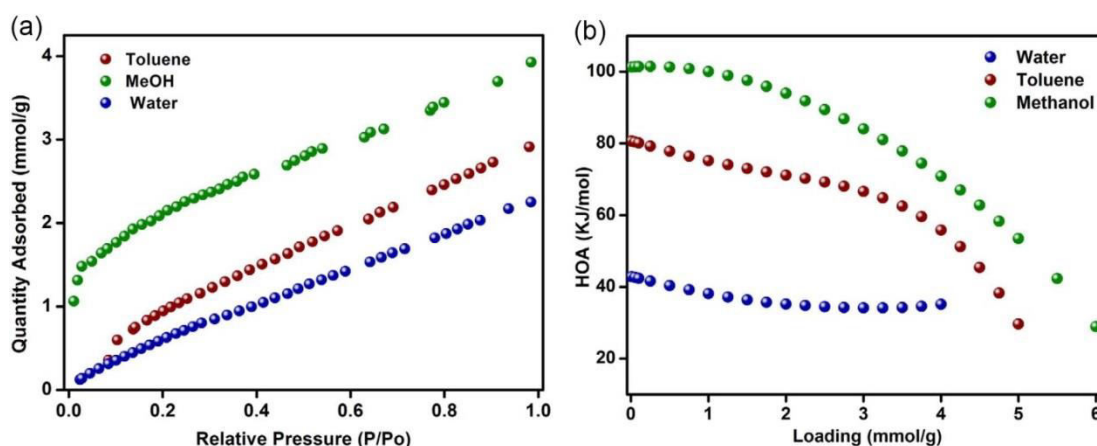


Figure 2.10. (a) Vapour sorption isotherms of IISERP-COF1 showing least interaction towards water and a more abrupt uptake of methanol at low P/P_0 region. (b) Heats of adsorption data showing the interaction being the strongest for methanol.

To further verify the favorable sites in IISERP-COF1 for interacting with Pd⁰ nanoparticles and the effectiveness of triazine cores to serve as interaction sites with Pd nanoparticles, modeling studies have been carried out. The interactions were modeled using a

DMOL³ program with DFT-D corrections (Accelrys). In P6/mcc unit cell, different starting configurations were generated by distributing the Pd atoms in specific sites (closer to the framework). When each such configuration was allowed to geometry optimize, it was found that the most energetically favorable sites were the small cleft formed around the triazine ring and the ether bonds (320 kcal/mol). Other prominent site was the nitrogens of the Schiff bonds (319 kcal/mol, Figure 2.11). The energy associated with Pd located in other sites (example: in the middle of the pore, closer to the aromatic backbone etc.) were much higher.

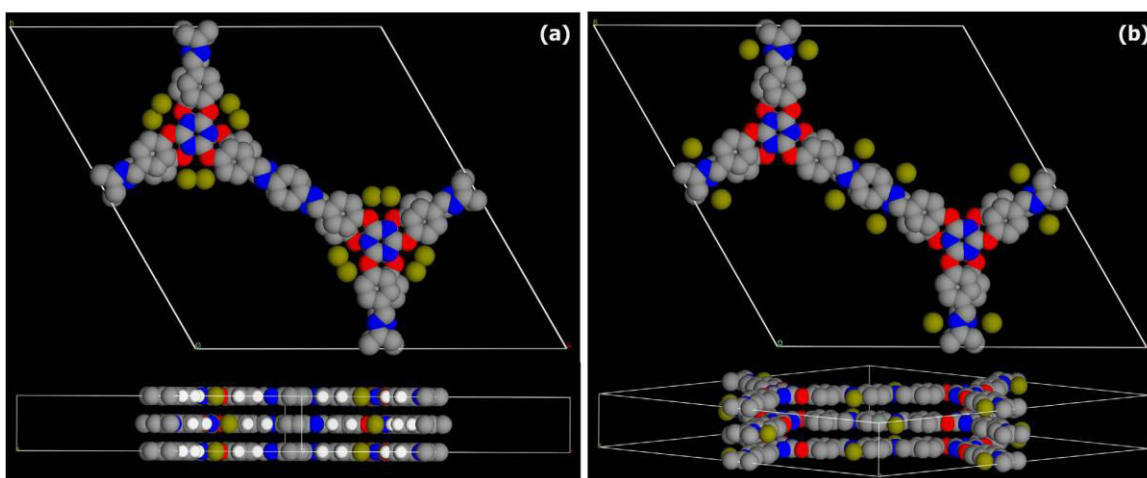


Figure 2.11. A DMol³ (DFT-D corrected) energy and geometry optimization of the Pd-COF interactions. Many starting models with different Pd position were attempted and it yielded two low energy configurations. (a) In the minimized geometry, the Pd atoms resided in the small clefts formed around the triazine core lined by the ether and the N and C of the triazine rings. A b-axis view showed that they were lined well with the layer. (b) Another minimized configuration included the interaction of the Pd atoms with the nitrogens of the Schiff bond. It can be seen that the Pd atoms align with the N atoms. In both cases the unit cell was retained and framework atoms were frozen in P6/mcc configuration. Color code: Pd- olive green; O- red; N- blue; C- grey and H- white.

2.6. Summary

In Summary, we have synthesized the novel IISERP-COF1 and Pd@IISERP-COF1 made up of long and flexible appendages. It crystallizes into a well-ordered structure with good crystallinity (hexagonal, P6/mcc). It has well-defined micro (13 Å) and mesopores (27 Å). Presence of palladium-specific interaction sites with a basic character, triazine and imine groups, favors a facile single-step loading of Pd⁰ nanoparticles into it under room temperature reduction. An 18–20% nano-Pd loading gives highly active composite working in the open air at low concentrations catalyzing simultaneous multiple-site Heck and C-C couplings using ‘non-

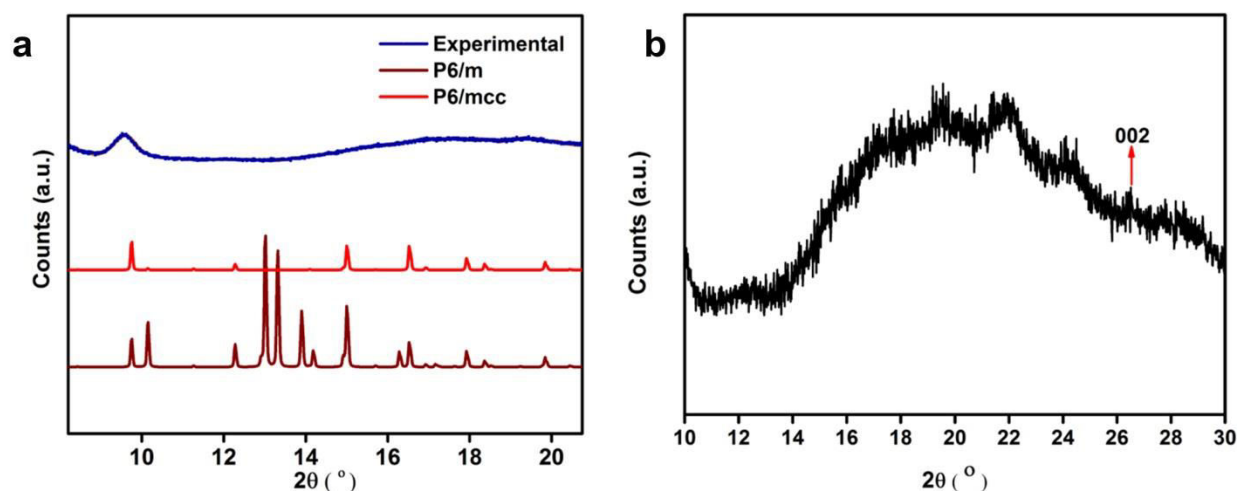
boronic acid' substrates and exhibits good recyclability with no sign of catalyst leaching. As an oxidation catalyst, it shows 100% conversion of CO to CO₂ at 150°C with no loss of activity with time and between cycles. Both vapor sorptions and contact angle measurements confirm the amphiphilic character of the COF. DFT studies showed the Pd-triazine and Pd-Schiff bond interactions as being most prominent.

2.7. References

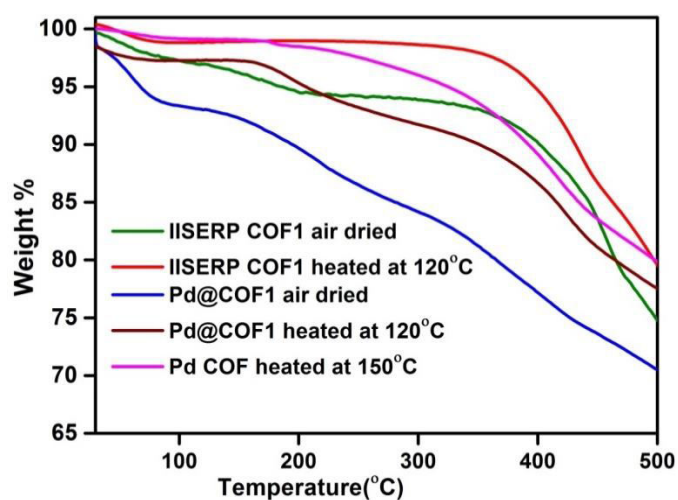
1. (a) Feng, X.; Ding, X.; Jiang, D. *Chem. Soc. Rev.* **2012**, 41, 6010. (b) Cote, A. P.; Benin, A. I.; Ockwig, N. W.; O'Keeffe, M.; Matzger, A. J.; Yaghi, O. M. *Science* **2005**, 310, 1166. (c) Ben, T.; Ren, H.; Ma, S.; Cao, D.; Lan, J.; Jing, X.; Wang, W.; Xu, J.; Deng, F.; Simmons, J. M.; Qiu, S.; Zhu, G. *Angew. Chem. Int. Ed.* **2009**, 48, 9457. (d) Colson, J. W.; Woll, A. R.; Mukherjee, A.; Levendorf, M. P.; Spitler, E. L.; Shields, V. B.; Spencer, M. G.; Park, J.; Dichtel, W. R. *Science* **2011**, 332, 228. (e) Pachfule, P.; Kandambeth, S.; Diaz, D.; Banerjee, R. *Chem. Commun.* **2014**, 50, 3169.
2. (a) Dalapati, S.; Jin, S.; Gao, J.; Xu, Y.; Nagai, A.; Jiang, D. *J. Am. Chem. Soc.* **2013**, 135, 17310. (b) Dogru, M.; Bein, T. *Nat. Nanotechnol.* **2011**, 6, 333. (c) Bertrand, G. H.; Michaelis, V. K.; Ong, T. C.; Griffin, R. G.; Dinca, M. *Proc. Natl. Acad. Sci. USA* **2013**, 110, 4923. (d) Chandra, S.; Kandambeth, S.; Biswal, B. P.; Lukose, B.; Kunjir, S. M.; Chaudhary, M.; Babarao, R.; Heine, T.; Banerjee, R. *J. Am. Chem. Soc.* **2013**, 135, 17853.
3. (a) Furukawa, H.; Yaghi, O. M. *J. Am. Chem. Soc.* **2009**, 131, 8875. (b) Xu, H.; Chen, X.; Gao, J.; Lin, J.; Addicoat, M.; Irleb, S.; Jiang, D. *Chem. Commun.* **2014**, 50, 1292.
4. (a) Ding, S. Y.; Wang, W.; *Chem. Soc. Rev.* **2013**, 42, 548. (b) Ding, S. Y.; Gao, J.; Wang, Q.; Zhang, Y.; Song, W. G.; Su, C. Y.; Wang, W. *J. Am. Chem. Soc.* **2011**, 133, 19816.
5. Modak, A.; Pramanik, M.; Inagaki, S.; Bhaumik, A. *J. Mater. Chem. A* **2014**, 2, 11642. (a) Bhunia, M. K.; Das, S. K.; Pachfule, P.; Banerjee, R.; Bhaumik, A. *Dalton Trans.*, **2012**, 41, 1304.
6. (a) Chen, X.; Engle, K. M.; Wang, D. H.; Yu, J. Q. *Angew. Chem. Int. Ed.* **2009**, 48, 5094. (b) Hassan, J.; Se´vignon, M.; Gozzi, C.; Schulz, E.; Lemaire, M. *Chem. Rev.* **2002**, 102, 1359.
7. Marrodan, C. M.; Berti, D.; Liquori, F.; Barbaro, P. *Catal. Sci. Technol.* **2012**, 2, 2279.
8. Groppo, E.; Agostini, G.; Borfecchia, E.; Wei, L.; Giannici, F.; Portale, G.; Longo, A.; Lamberti, A. *J. Phys. Chem. C* **2014**, 118, 8406.

-
9. Reggelin, M.; Doerr, S.; Klussmann, M.; Schultz, M.; Holbach, M. *PNAS*. **2014**, 101, 5461.
 10. Pachfule, P.; Panda, M. K.; Kandambeth, S.; Shivaprasad, S. M.; Díaz, D. D.; Banerjee, R., *J. Mater. Chem. A* **2014**, 2, 7944.
 11. (a) Dhakshinamoorthy, A.; Asiric, A. M.; Garcia, H.; *Chem. Soc. Rev.*, **2015**, 44, 1922. (b) Long, J.; Liu, H.; Wu, S.; Liao, S.; Li, Y. *ACS Catal.* **2013**, 3, 647.
 12. Fang, P. P.; Jutand, A.; Tian, Z. Q.; Amatore, C. *Angew. Chem. Int. Ed.* **2011**, 50, 12184.
 13. Stulgies, B.; Prinz, P.; Magull, J.; Rauch, K.; Meindl, K.; Rühl, S.; de Meijere, A. *Chem. Eur. J.* **2005**, 11, 308.
 14. (a) Zhou, Y.; Xiang, Z.; Cao D.; Liu, C.-j. *Ind. & Eng. Chem. Res.* **2014**, 53, 1359. (b) Freund, H. J.; Meijer, G.; Scheffler, M.; Schlogl, R.; Wolf, M. *Angew. Chem. Int. Ed.* **2011**, 50, 10064. (c) Liang, Q.; Liu, J.; Wei, Y.; Zhao, Z.; MacLachlan, M. J. *Chem. Commun.* **2013**, 49, 8928.
 15. Deborah, C. T.; Tomikazu, S.; *J. Org. Chem.* **1994**, 59, 679.
 16. He, Q. L.; Lai, Y. H.; Lu, Y.; Law, K. T.; Sou, L. K. *Sci. Rep.* **2013**, 3, 2497.
 17. Reetz, M. T.; de Vries, J. G. *Chem. Commun.* **2004**, 1559.
 18. Smith, M. D.; Stepan, A. F.; Ramarao, C.; Brennan, P. E.; Ley, S. V. *Chem. Commun.* **2003**, 2652.
 19. Taylor, J. M.; Vaidhyanathan, R.; Iremonger S. S.; Shimizu, G. K. H. *J. Am. Chem. Soc.* **2012**, 134, 14338.

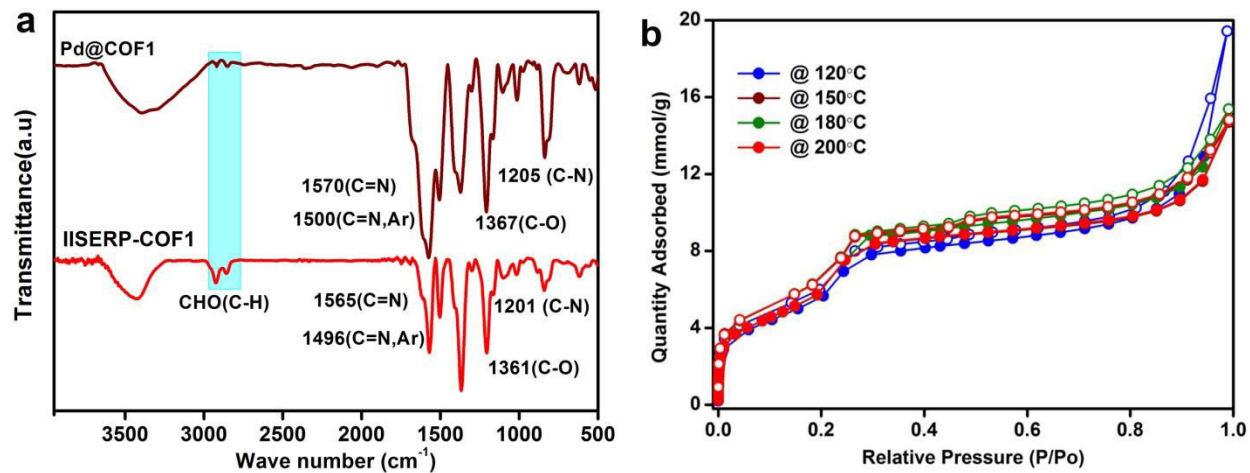
Chapter-2 Appendix



Appendix 2.1 (a)PXRD of the as-synthesized form of IISERP- COF1 being compared to the simulated patterns of P6/m and P6/mcc, showing the lack of peaks expected for the P6/m in the 12° to 16° of 2-theta region and indicating a better fit to P6/mcc. (b) Shows the 002 peak at $2\theta = 26.2^\circ$ corresponding to the interlayer spacing of 6.81Å in the P6/mcc setting.



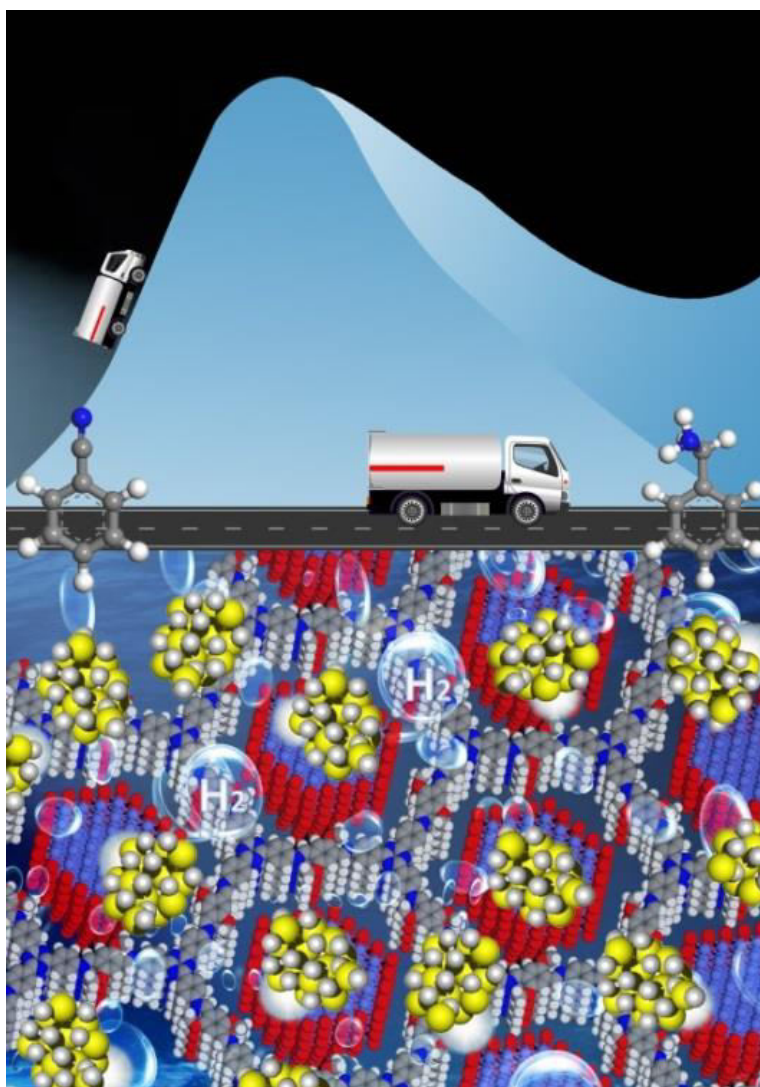
Appendix 2.2 Thermogravimetric analysis of IISERP-COF1 and Pd@IISERP-COF1. Both the as made IISERP- COF1 and Pd@IISERP-COF1 shown significant weight loss at $>140^\circ\text{C}$ this could be due to the solvent and moisture content that could be strongly adsorbed on the surface of the Pd nanoparticles or COF. However, TGA of the high temperature dried Pd@IISERP-COF1 showing the near complete removal of these solvents during this thermal treatment.



Appendix 2.3. (a). IR spectra were showing the presence of expected functionalities and a good match between the catalyst (b) the support Shows the 77K N₂ adsorption isotherms of Pd@IISERP-COF1 heat treated at different temperatures under a vacuum atmosphere.

Chapter-3

Enhancing the Stability of Schiff-Bonded COF for use as Support for Catalytic Cobalt Nanoparticles and their Activity in Releasing H₂ Gas from Solid Hydride Sources under Harsh Aqueous Conditions and the In-Situ Reduction of C≡N/NO₂ to Amines



3.1. Introduction

Covalent Organic Frameworks owing to their highly ordered structure, chemical tunability and porosity can serve as excellent supports for metal nanoparticles (nps)¹. In our earlier chapter, we showed that triazine-COF (IISERP-COF1) can serve as a porous host for growing small uncapped nanoparticles. The resulting composite exhibited exceptional stability and high catalytic activity for the multi-fold Heck coupling and CO oxidation reactions². Some of the recent works on metal–superoxo species oxygen activation reactions highlight the potential interplay between magnetism and catalysis in inert C-H bond activation and hydrogenation reactions^{3, 4}. Encouraged by these findings, we realized, if magnetic nanoparticles can be grown in the nano-confinements of a porous COF it might yield catalytically active 'nanomagnets'. The modular construct of a COF enables controlled inclusion of heteroatoms, which is key to functionalizing the COF for binding with first and second-row transition metals. While there are reports on the use of COF supported noble metal nanoparticles (Pd, Au) as heterogeneous catalyst^{1,2}, utilizing N-rich COF as support for the non-noble metal catalyst (Co, Ni) is fairly recent^{5,6}.

In this chapter we demonstrate the effectiveness of IISERP-COF5 embedded with Co metal nanoparticles as a catalyst for the on-demand release of H₂ from a very safe and cheap solid hydrogen source namely the NaBH₄ (a high gravimetric density (> 4.0 wt%) and volumetric density 30 wt% solution of NaBH₄ ~63 g H₂/L without any toxic by-products like CO, CO₂)⁷. NaBH₄ is more stable and cheaper than the well-investigated hydrogen storage material aminoborane (NH₃:BH₃)⁸. Also, sodium borohydride (NaBH₄) can release 4H₂ per formula unit, compared to the 3H₂ by the NH₃:BH₃. Typically, the hydrogen release from sodium borohydride is catalyzed by noble metal catalysts⁹ and such catalysts with non-noble metals are scarce¹⁰. Thus, there is a clear need for efficient noble metal-free heterogeneous catalysts for H₂ evolution from NaBH₄. Developing such active catalysts from earth-abundant and environmentally benign materials adds immense value. Generally, the activity of the first-row transition (3d) metals in these types of redox reactions is quite sluggish. To enhance their catalytic activity, they are either engineered into high surface area nanostructures and/or grown as small nanoparticles (<10nm) using capping agents¹¹. But such capping is known to inhibit access to the nanoparticle surfaces. In this regard, COFs can play an excellent role of being a high surface area support for growing such catalytically active small nanoparticles and in

facilitating the development of heterogeneous catalysts, which have several advantageous in terms of high recyclability, ease of handling and inexpensive.

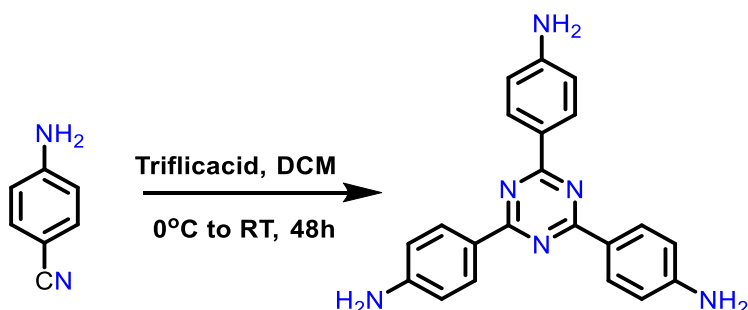
The catalytic hydrogenation of nitriles (-CN) is an atom-economic route to amines (-NH₂)¹². Nitriles are typically reduced to amines using metal hydrides, hydrosilanes, or organocatalysts¹³. But, these methods have a poor catalyst economy and low functional group tolerance. The most atom economy is realized from using H₂ gas. Undesirably, reductions using H₂ are typically carried out using a noble metal catalyst (Pt, Pd and Au etc.) and at elevated temperatures and pressures, which can prove unsafe and energy-consuming (Appendix Table 1). While there are many reports for the reduction of nitro (-NO₂) compounds using NaBH₄ or NH₃:BH₃ type of solids, very few reports are available on their use in nitrile (-CN) reduction (Appendix Table 1). Few cobalt based heterogeneous catalysts have been used for various reduction reactions.¹⁴ However, the reductions using NaBH₄ is usually achieved by the use of noble metal catalysts¹⁵. These are sensitive to moisture can ignite easily, particularly under the elevated pressure and temperature (Appendix Table 1 and 2). The most recent report comes from Lin and co-workers, who demonstrated the use of a Co-Zr-MOF as a single-site catalyst for the nitrile to amine reduction¹³. While, Beller and co-workers found a high activity for this reaction in a catalyst formed by supporting 1,10-phenanthroline decorated Co(OAc)₂ on α -Al₂O₃¹⁶. In their work, they emphasize the crucial role of the alumina support in realizing high activity. One drawback, in both Co-Zr-MOF and alumina (Co(OAc)₂ on α -Al₂O₃) catalyzed nitrile to amine hydrogenation is the need to employ at 40 bar pressurized H₂ as the reducing medium and temperatures in the range of 85-110°C. In comparison to these inorganic supports, carbonaceous porous materials are advantageous owing to their ability to facile absorb small organic molecules and can thereby boost catalytic activity⁷. In the case of COFs, despite being insoluble solids, they can be chemically tuned to mimic the solvent environments of a homogeneous catalyst^{1,2}. Hence, developing a heterogeneous reduction catalyst with tunable organic support that can operate under ambient conditions is still rewarding in heterogeneous catalysis.

3.2. Experimental details

3.2.1. Materials and Measurements

Powder X-ray diffractions were carried out using Bruker D8 Advance X-ray powder diffractometer (Cu K α radiation, $\lambda = 1.541\text{\AA}$) and for some cases using Rigaku Miniflex-600 instrument and processed using PDXL software. Variable temperature Powder X-ray diffractions (VT-PXRD) were carried out using the Bruker D8 Advance X-ray powder diffractometer (Cu K α radiation, $\lambda = 1.541\text{\AA}$) fitted with the standard variable temperature furnace. Thermogravimetric Analysis (TGA) was carried out on NETSZCH TGA-DSC system. The routine TGAs were done under N₂ gas flow (20ml/min) (purge + protective) and samples were heated from RT to 600°C at 2K/min or from RT to 900°C at 5K/min. Infrared (IR) spectra were recorded using Bruker FT-IR (ATR mode) spectrophotometer in the range of 4000-600 cm⁻¹. NMR spectra were recorded on a 400 MHz Jeol ECS-400, Bruker 400MHz and Bruker 500MHz. Adsorption studies were done using a Quantachrome pore and surface area analyser, Model IQ dual port. FEI (Jeol FEG 2100F) high resolution transmission electron microscope (HR-TEM) equipped with field emission source operating at 300 KeV was used. GC analysis was carried out using an Agilent 7890B GC system on a HP-05 (30m \times 0.25 mm \times 320 μ m) column and split ratio 30:1 and inlet temperature was 320°C. Temperature program starts at 70 °C then hold for 1min @ 2 °C to 120 °C, and @ 20 °C to 320 °C hold for 3 mins, FID temperature: 330 °C. UV-Vis absorption studies were carried out on Shimadzu UV- 3600 UV/Vis/NIR spectrophotometer over the entire range of 400 – 800 nm. M-H hysteresis loops were measured using a Quantum design MPMS-XL SQUID magneto meter. The powder specimen was packed in a gelatin capsule and loaded inside a plastic straw. The M-H isotherm measurements at 5K and 300K, were performed by sweeping the magnetic field up to ± 5 Tesla. X-Ray photoelectron spectroscopic (XPS) measurements were carried out on a VG Micro Tech ESCA 3000 instrument at a pressure of $>1 \times 10^{-9}$ Torr (pass energy of 50 eV, electron take-off angle of 60°, and the overall resolution was 0.1 eV). Ultra Plus Field Emission Scanning Electron Microscope (FE-SME) with integral charge compensator and embedded EsB and AsB detectors. Oxford X-max instruments 80mm². (Carl Zeiss NTS, Gmbh), Imaging conditions: 2kV, WD =2mm, 200kX, In-lens detector

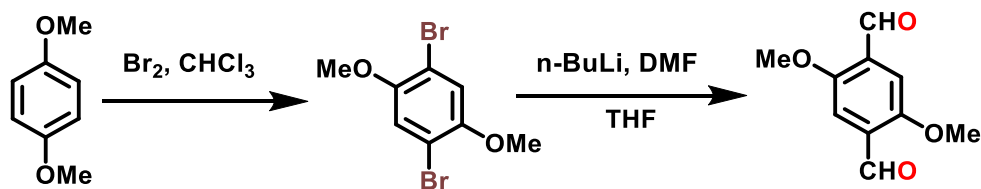
3.2.2. Synthesis of 2,4,6-Tris(4-aminophenyl)-s-triazine ligand (1)



In a typical synthesis, trifluoromethanesulfonic (triflic acid) acid was added to 100mL of trichloromethane (CHCl_3) in a two neck round bottom flask maintained at 0°C under an N_2 atmosphere and stirring was continued for 2hrs. Simultaneously, 4-aminobenzonitrile (4gm, 0.033mol) was dissolved in 80mL of CHCl_3 in the nitrogen atmosphere and slowly added drop by drop to the trifluoromethanesulfonic acid solution at 0°C under a blanket of N_2 . The reaction mixture was warmed up to room temperature and was allowed to stir under N_2 for additional 48hrs. Completeness of the reaction was monitored using TLC. The contents were neutralized by adding about 250 mL of 2M NaOH solution. Upon neutralization, a pale yellow precipitate was obtained, which was filtered and washed with copious amounts of distilled water. Yield: 94%. The product was characterized by ^1H , and ^{13}C NMR.

^1H NMR (400 MHz, DMSO- D_6): $\delta = 8.37$ (d, $J = 8.7$ Hz, 6H), 6.70 (d, $J = 8.6$ Hz, 6H), 5.96 (s, 6H). ^{13}C NMR (101 MHz, DMSO- D_6): $\delta = 170.09$, 152.95 , 130.50 , 122.96 , 113.18 .

3.2.2. Synthesis of 2,5-dimethoxybenzene-1,4-dicarboxaldehyde ligand (2)



The 2,5-dimethoxybenzene-1,4-dicarboxaldehyde monomer was synthesized by a slight modification to reported procedure¹⁷ In a typical synthesis, 10 gm of 1,4-dimethoxybenzene was added to 50mL of dry CHCl_3 in a two neck round bottom flask maintained at 0°C under N_2 atmosphere. To this, 10 mL of bromine solution was slowly added over 30 mins and stirring was continued for additional 2hrs. The resulting reaction mixture was poured into 500 mL of 1M

KOH aqueous solution to remove any unreacted bromine. Upon KOH addition, the brownish colored solution changed into a yellowish color. The resulting mixture was poured into ice water (400 mL) and extracted with dichloromethane, the organic layer was washed with brine solution and water over three times. The extracted organic layer was dried with Na_2SO_4 and the solvent was removed under reduced pressure to give a white solid of 1,4-dibromo-2,5-dimethoxybenzene with an Yield of 90%. The product was characterized by ^1H and ^{13}C NMR. ^1H NMR (400 MHz, CDCl_3): $\delta = 7.08$ (s, 2H), 3.82 (s, 6H). ^{13}C NMR (100 MHz, CDCl_3): $\delta = 150.73$, 117.35, 110.71, 57.23.

1,4-dibromo-2,5-dimethoxybenzene (3gm 0.1mol) was added to 60mL of dry THF at 78°C under N_2 atmosphere, The mixture was thawed and the stirring was continued until 1,4-dibromo-2,5-dimethoxybenzene dissolved completely. To this 15 mL of n-Butyllithium 2.5 M in hexane and 3.0 mL of dry DMF was added at -78°C . The reaction was warmed up to room temperature and stirring was continued overnight. The resulting mixture was neutralized with 10 ml of 3N hydrochloric acid. After extraction with dichloromethane, the organic layer was washed with brine and the extracted organic layer was dried with Na_2SO_4 and solvent was removed under reduced pressure give a yellow color of 2,5-Dimethoxybenzene-1,4-dicarboxaldehyde compound (Yield: 300mg). The product was characterized by ^1H and ^{13}C NMR. ^1H NMR (400 MHz, CDCl_3): $\delta = 10.50$ (s, 1H), 7.45 (s, 1H), 3.94 (s, 3H). ^{13}C NMR (100 MHz, CDCl_3) δ 189.70, 156.19, 129.59, 111.37, 56.69.

3.2.3. Synthesis of IISERP-COF5

2,4,6-Tris(4-aminophenyl)-s-triazine (40 mg, 0.112mmol) and 2,5-dimethoxyterephthalaldehyde (33 mg, 0.169mmol) were weighed into a Pyrex tube and dissolved in ethanol (3.0 mL), to this *o*-dichlorobenzene (*o*-DBC,3.0mL) was added. Following this, 0.25 mL of aqueous acetic acid (3 M solution) was added to this mixture. Then the Pyrex tube was flash frozen in a liquid nitrogen bath and sealed. The Pyrex tube along with its contents was placed in an oven at 120°C for 3 days. This yielded about 52mg of yellow colored solid which was washed with DMF, dioxane, MeOH, Acetone and THF (86%, isolated yield). A soxhlet extraction/wash was carried out on the final product and the supernatant was analyzed using solution NMR and no peaks corresponding to any organic impurity was found suggesting the sample is free of any dissolved oligomers (Formula for IISERP-COF5 $\text{C}_{72}\text{N}_{12}\text{H}_{48}\text{O}_6$, M. Wt. 1177.25 g/mol, CHN Obsd. C =

67.81; H = 3.15; N = 12.97. Calc. C=73.46; H=4.11; N=14.28). The discrepancy in the CHN values can be attributed to the presence of some unreacted aldehyde and amine sites in the COF framework. This is consistent with the observations from the SSNMR and IR spectra.

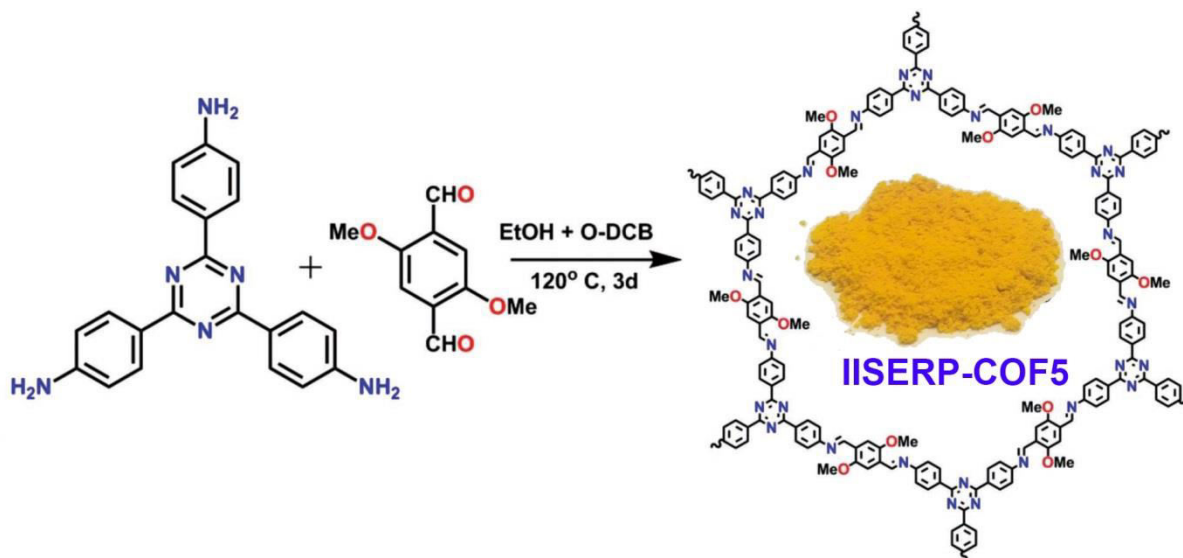


Figure 3.1. Schematic representation of the IISERP-COF5 synthesis and proposed topology structure.

3.2.4. Synthesis of Co@IISERP-COF5 Composite (1)

The Co@IISERP-COF5 (Co@COF5) was synthesized via a slight modification of the double solvent method^{5,8}. In a typical synthesis, the COF (100 mg) was dispersed in 40 mL of n-hexane and the mixture was sonicated for about 30 min resulting in a yellow color dispersion (Figure S2). To this, a clear methanolic solution of $\text{CoCl}_2 \cdot 6\text{H}_2\text{O}$ (100 mg in 0.2 mL of MeOH) was added drop by drop over a period of 3 h with vigorous stirring. Upon addition of the methanolic $\text{CoCl}_2 \cdot 6\text{H}_2\text{O}$ solution to the COF dispersion, the solution turns from yellow into a pinkish-orange color. Contents were stirred for 12 h at room temperature. The solid particles are extracted by decanting the solvent and were dried at room temperature. The solid was heated at 150°C for 12 h and then cooled to room temperature. This solid was suspended in 20 mL of water and the reduction was carried out by adding 30 mL freshly prepared 0.6 M aqueous NaBH_4 solution under vigorous stirring. This resulting solid was washed with copious amounts of millipore water and ethanol. These results in the formation of the COF supported cobalt catalysts as a blackish-brown color solid. The synthesized samples were collected by centrifuging and

dried under vacuum then used for the characterizations and catalytic studies. Also, the final blackish-brown solid even upon sonicating in water did not seem to produce any colored solution, suggesting the lack of any unreacted or unloaded Co^{2+} salts that could be leaching out. The EDAX analyses of a solid extracted from this aqueous supernatant confirmed the absence of any metal. In addition, the EDAX analysis carried out on the extracted metal-COF composite showed no trace of chloride ions. (CHN % Obsd. Co@IISERP-COF5 ($\text{C}_{72}\text{N}_{12}\text{H}_{48}\text{O}_6 \cdot (\text{Co})_{3.2}$): C = 60.35; H = 3.99; N = 11.96; calculated C= 63.32; H= 3.54; N= 12.31. The Cobalt loading from EDAX was in the range of 5-6 wt% which was much lower than the anticipated loading (100 wt% is expected for a complete loading and reduction of all the Co^{2+} to Co). This could be due to the Cobalt being buried in the COF and also due to the surface Co atoms being hydroxylated to $\text{Co}(\text{OH})_2$. Hence we resorted to Inductively Coupled Plasma (ICP) analysis to determine the overall Cobalt content. From which, assuming that all the cobalt is in a metallic form, we estimate a loading of 3.2 mol of Cobalt per formula unit (16 wt %). The Cobalt loading was systematically varied to identify the highest possible loading. The following cobalt chloride hexahydrate loading amounts were prepared: **Co@COF-20%** (10mg of $\text{CoCl}_2 \cdot 6\text{H}_2\text{O}$:40mg COF); **Co@COF-33%** (20mg of $\text{CoCl}_2 \cdot 6\text{H}_2\text{O}$:40mg COF); **Co@COF-43%** (30mg of $\text{CoCl}_2 \cdot 6\text{H}_2\text{O}$:40mg COF) and **Co@COF-50%** (40mg of $\text{CoCl}_2 \cdot 6\text{H}_2\text{O}$:40mg COF). The highest loading, 50 wt% Cobalt Chloride loading yields the catalyst with ~16 wt% of Cobalt nanoparticles loaded on the COF and this has been named as $\text{Co@IISERP-COF5}(\text{Co@COF5})$.

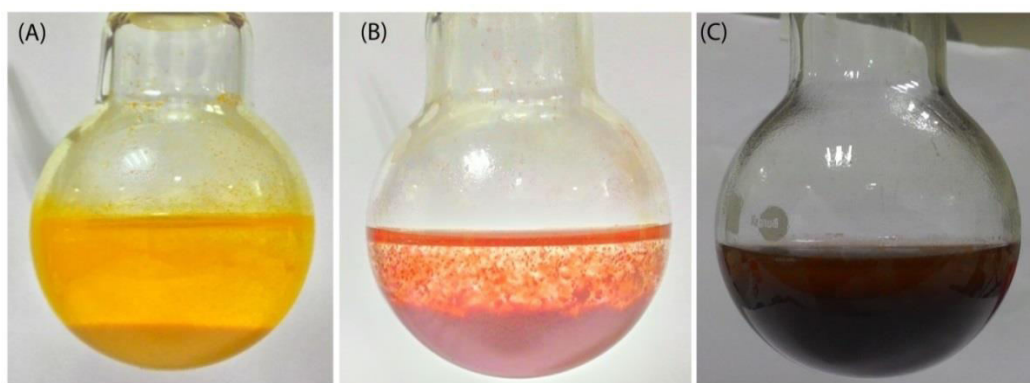


Figure 3.2. Photographic images of color change during the metal nanoparticle loading (A) As-synthesized COF before addition of metal salt. (B) After the addition of metal salt. (C) After the reduction using $\text{NaBH}_4(\text{aq})$.

3.2.4. Synthesis of unsupported Co/Co(OH)₂ nanoparticles (2)

The unsupported catalyst was prepared by dissolving the cobalt chloride hexahydrate (100mg) in 20ml of water and this was reduced using 30ml of a 0.6M aqueous solution of NaBH₄. This yielded a black colored relatively dense powder.

3.2.5. General procedure for the catalytic Hydrogen Evolution from NaBH₄

A mixture of Co@IISERP-COF5 catalyst (10mg, 0.0072mmol), sodium hydroxide (NaOH) (20mg, 0.5mmol) and distilled water (2.5 mL) was placed in a two-necked round-bottomed flask (30 mL), which was placed in a water bath at room temperature under ambient atmosphere. A gas burette filled with water was connected to the reaction flask to measure the volume of hydrogen released during hydrolysis. The reaction started when aqueous NaBH₄ solution (1 mmol in 0.5 mL water) was injected into the mixture using a syringe with vigorous stirring. The volume of the evolved hydrogen gas was monitored by recording the displacement of water in the gas burette. The completion of the reaction was indicated by no further gas generation.



Hydrogen evolution reaction in methanol: $\text{NaBH}_4 + 2\text{MeOH} \rightarrow \text{NaB}(\text{OCH}_3)_2 + 4\text{H}_2$

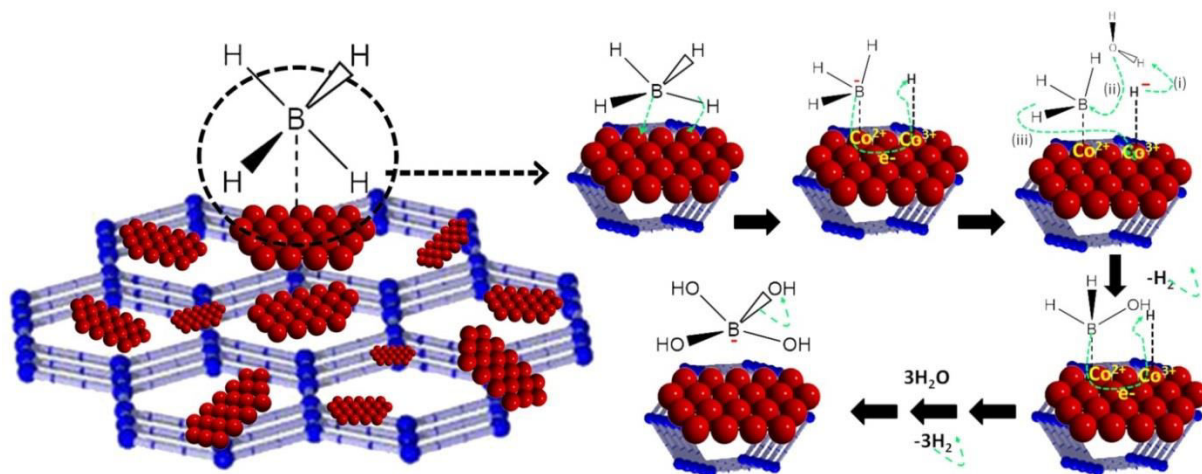
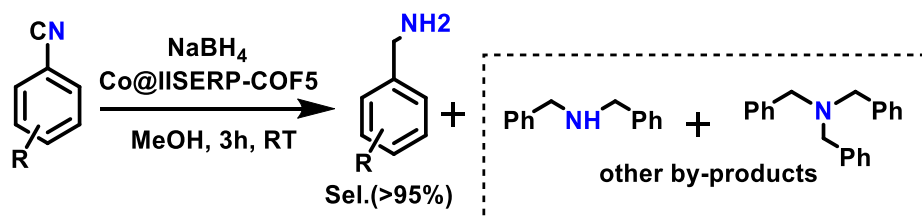


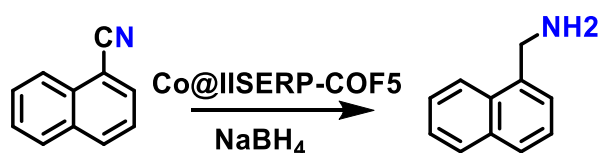
Figure 3.3. A schematic representation of the role of the Co@IISERP-COF5 catalyst in the activation of BH₄⁻ ions and in releasing the H₂ from aqueous solution.

3.2.6. General Procedure for the Catalytic Nitrile Reduction Reactions



In a typical reaction, a mixture of Co@IISERP-COF5 catalyst (0.0072 mmol), and NaBH₄ (2.5 mmol) were added into a pyrex tube. To this, about 3 mL of methanolic solution of the aryl nitrile (0.5 mmol) was added and the pyrex tube was sealed immediately. The contents were stirred at room temperature for 3 hrs. After completion of the reaction (monitored by TLC), the crude reaction mixture was filtered through celite and washed with 150 mL of Dichloromethane (DCM). This product containing DCM solution was concentrated using rota-evaporation and was further purified by column chromatography on silica gel (200 mesh) using 5-10% methanol in DCM as the eluent. After completion of the reaction, the catalyst was recovered by a magnet and dried for further use. The products were characterised by ¹H and ¹³C NMR, HRMS and GCMS/GC. GC yields were calculated by using m-xylene as an internal standard. The use of methanolic solution as the reaction medium enabled the facile dissolution of a wide range of substrates. Note: The room temperature ferromagnetic nature of the nanocomposite particles makes the catalyst removal a very easy process.

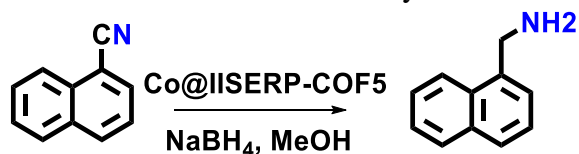
Table 3.1. Optimization of reaction conditions - Screening of different organic solvents.



Entry	Solvent	Cat.amount.	Time	GC conversion
1	MeOH	10mg	3hrs	>99%
2	EtOH	10mg	3hrs	~95%
3	i-PrOH	10mg	3hrs	<2%
4	n-BuOH	10mg	3hrs	<3%
5	H ₂ O	10mg	3hrs	~30%
6	THF	10mg	3hrs	<2%
7	Benzene	10mg	3hrs	n.d.
8	Toluene	10mg	3hrs	n.d.
9	n-Hexane	10mg	3hrs	n.d.
10	MeOH+H ₂ O	10mg	3hrs	~54%

Reaction conditions: 0.0075 mmol of Co@IISERP-COF5 catalyst, 0.5mmol of 1-Naphthonitrile and 2.5 mmol of NaBH₄ at room temperature for 3hrs. Note: n.d.- not determined. Note: Co@IISERP-COF5 refers to the 16 wt% Co nanoparticles loaded in the IISERP-COF5.

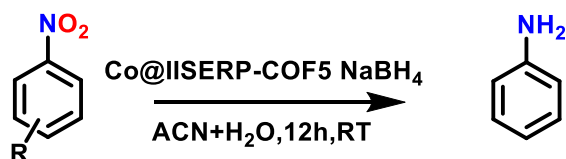
Table 3.2. Optimization of reaction conditions- Catalyst amounts and reaction time.



Entry	Catalyst	Cat.amount	Time	Conversion
1	Co@COF5.cat-20% ^a	10mg	3hrs	15%
2	Co@COF5.cat-33% ^a	10mg	3hrs	35%
3	Co@COF5.cat-43% ^a	10mg	3hrs	54%
4	Co@COF5-50% ^a	10mg	3hrs	>99%
5	IISERP-COF5 ^b	10mg	3hrs	6%
6	CoCl ₂ .6H ₂ O	10mg	3hrs	25%
7	Neat Co NPs ^c	10mg	3hrs	28%
8	Co@COF5.cat.	3mg	3hrs	33%
9	Co@COF5.cat.	5mg	3hrs	~71%
10	Co@COF5.cat.	10mg	12hrs	>99%
11	Co@COF5cat.	10mg	6hrs	>99%
12	Co@COF5.cat.	10mg	3hrs	>99%

Reaction conditions: 0.0075 mmol of Co@IISERP-COF5 catalyst, 0.5mmol of 1-Naphthonitrile, 2.5 mmol of NaBH₄ and 3mL of MeOH. a- the number % indicates the amount (in mgs) of CoCl₂.6H₂O loaded per 100mg of IISERP-COF5. ^bneat COF without metal nPs. ^c neat Co nanoparticles without COF support.

3.2.7. General Procedure for the Catalytic Nitro Reduction Reactions



In general, a mixture of Co@IISERP-COF5 catalyst (0.0072mmol) and NaBH₄ (2.5 mmol) was added into a pyrex tube. To this, about 3mL of an acetonitrile solution of the nitroarenes (0.5 mmol) and 0.5mL of water were added and the tube was sealed immediately. The reaction was continued stirring at room temperature for 12hrs. After completion of the reaction, the crude reaction mixture was filtered through celite and washing with 150mL of DCM, resulting mixture was evaporated using rota-evaporation and purified by column chromatography on silica gel using 10% EtOAc and hexane mixture. After completion of the reaction the catalyst was

recovered by centrifugation and dried for further use. The products were characterized by ^1H and ^{13}C NMR, HRMS and GCMS/GC.

3.3. Structure Solution and Description

A two-dimensional structure made up of hexagonal layers that are consistent with the experimentally observed powder X-ray pattern was modeled using the *Material Studio* program. For the structure solution, we adopted the same routine as in our earlier work². The *XCELL* program was used to index the experimental Powder X-ray Diffraction (PXRD) pattern and to identify the best possible space group as being P6, for the structure including the hydrogen atoms. The geometry optimized and energy minimized final structure with an eclipsed configuration, was obtained using Tight Binding Density Functional Theory (DFT-TB) (Figure 1B). The experimental PXRD pattern could be refined against this model using a *Pawley routine*. An excellent fit was obtained (Figure 3.4A). Also, the pore dimensions observed for this eclipsed model agrees well with the experimentally determined pore sizes (Figure 3.8B).

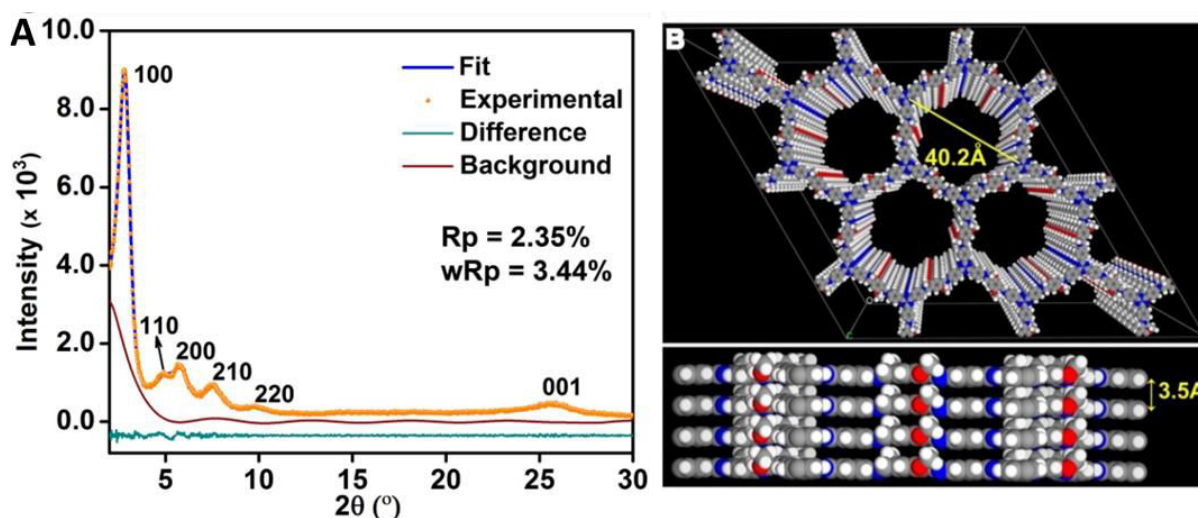


Figure 3.4. (A) Pawley refinement fit, of IISERP-COF5. (B) A unit cell perspective view of the 1D channel in the most-probable structure of IISERP-COF5, the hexagonal layers stack in an eclipsed fashion with an interlayer separation of 3.5 Å. (Formula: $\text{C}_{72}\text{H}_{48}\text{O}_6\text{N}_{12}$): space group: P6, lattice or unit cell $a = b = 37.21$; $c = 3.54$ Å.

3.4. Results and Discussion

IISERP-COF5 is prepared as an insoluble solid via solvothermal synthesis. The obtained solid product exhibited good crystallinity and could be made in bulk quantities (grams) with high

purity as indicated by the PXRD (Figure 3.5). The methoxy groups were introduced in the COF because of owing to its ability to increase the stability at the Schiff bond links via its electron-donating character¹⁸. thus resulting IISERP-COF5 poses remarkable stability upon harsh treatments: soaking in highly polar DMF, DMSO, MeOH and non-polar benzene and acid (3M HCl) and base (3M NaOH) for 7 days and even to boiling in water (Figure 3.5A). Thermogravimetric analysis (TGA) measurement and the variable temperature PXRD (VT-PXRD) of IISERP-COF5 displays its excellent thermal stability up to 400°C (Figure 3.5B).

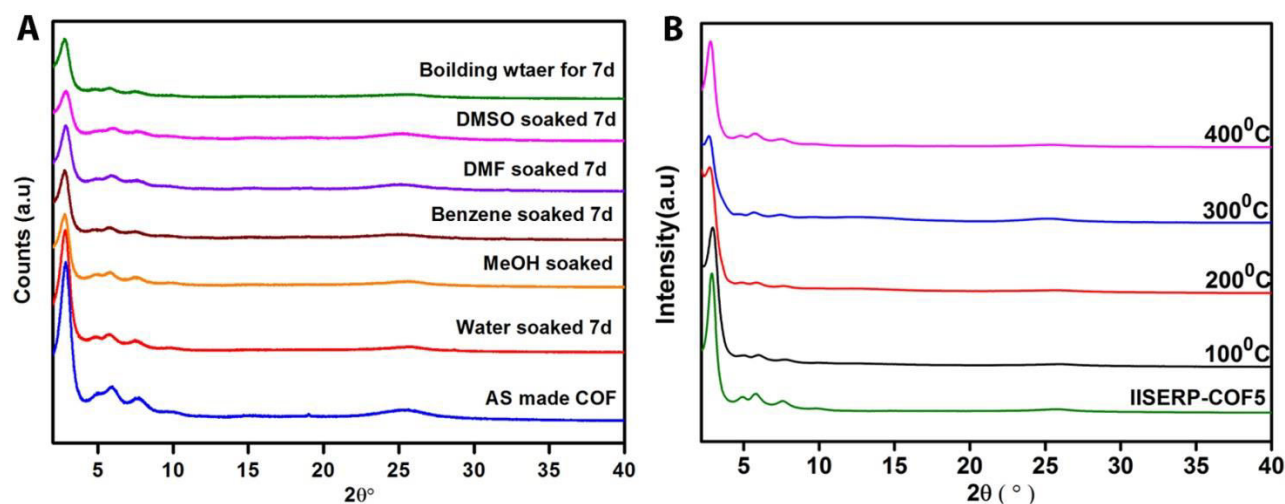


Figure 3.5. (A) A comparison of the PXRD of the COF and the Co@IISERP-COF5 (b) Stability of the COF towards acids, bases and solvents from PXRD studies.

As synthesized IISERP-COF5 is loaded with $\text{CoCl}_2 \cdot 6\text{H}_2\text{O}$ using double solvent method¹⁵ upon addition of $\text{CoCl}_2 \cdot 6\text{H}_2\text{O}$ resulted in a sharp color change from yellow to pinkish-orange, which is retained its color even when the solid is washed and dried at 120°C, thus indicating an intimate loading of Co^{2+} ions into the solid. This solid, when reduced with $\text{NaBH}_4(\text{aq})$ yielded the composite (Co@IISERP-COF5) as a blackish-brown colored fine powder (Figure 3.3). The powder X-ray diffraction (PXRD) pattern of Co loaded COF matches well with as made COF and did not show any the peaks corresponding to Co-metal at higher 2θ suggesting them forming as exceptionally small nanoparticles (Figure 3.6)⁷. Solid-state ^{13}C -NMR (500 MHz) spectra of IISERP-COF5 displays eight individual peaks/ signals between $\delta = 114.57$ to 159.90 ppm, which were assigned to be aromatic benzene and triazine carbons (Figure 3.7A). The signal observed at ~159 ppm indicates the formation of the imine($\text{C}=\text{N}$) bond which propagates to form the conjugated crystalline covalent organic framework (IISERP-COF5). These features corroborate

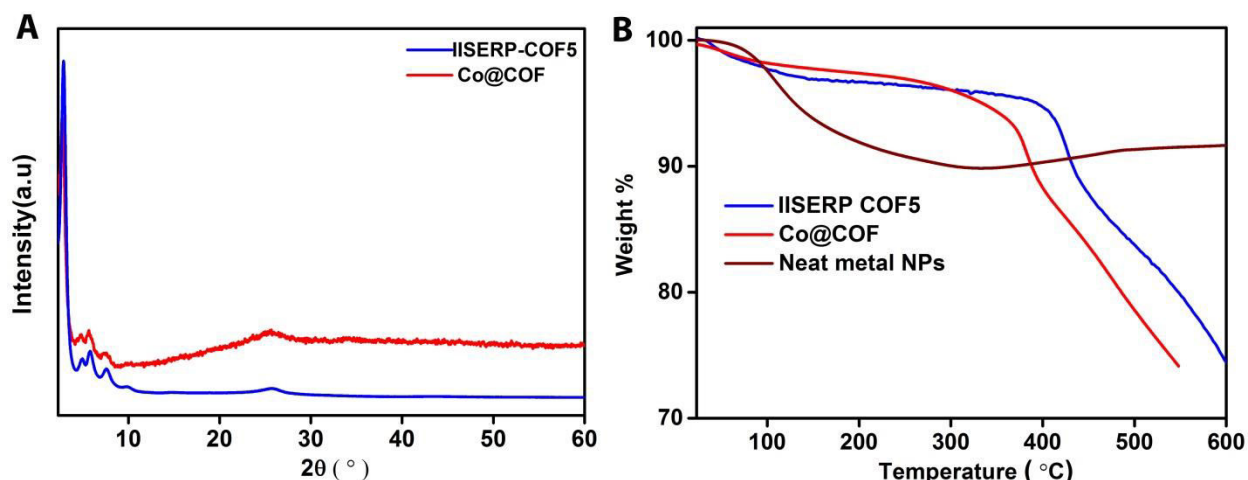


Figure 3.6. (A) The variable temperature powder X-ray diffraction (VT-PXRD) of the IISERP-COF5. (B) TGA measurement shows the thermal stability of the COF up to 400°C.

well with the functional groups observed from the Fourier transform infrared (FTIR) spectra (Figure 3.7B). The parent IISERP-COF5 shows characteristic stretching bands for C=N Schiff bond at 1615cm^{-1} and aromatic triazine C=N at 1598cm^{-1} , these bands are retained also by the nanoparticle loaded IISERP-COF5. Considering that the reduction procedure involved in the nanoparticle loading is quite harsh, this suggests the stability of the IISERP-COF5 towards the harsh reduction conditions. This is crucial when it comes to applying these COFs as catalyst support for organic reactions carried out in a solution medium.

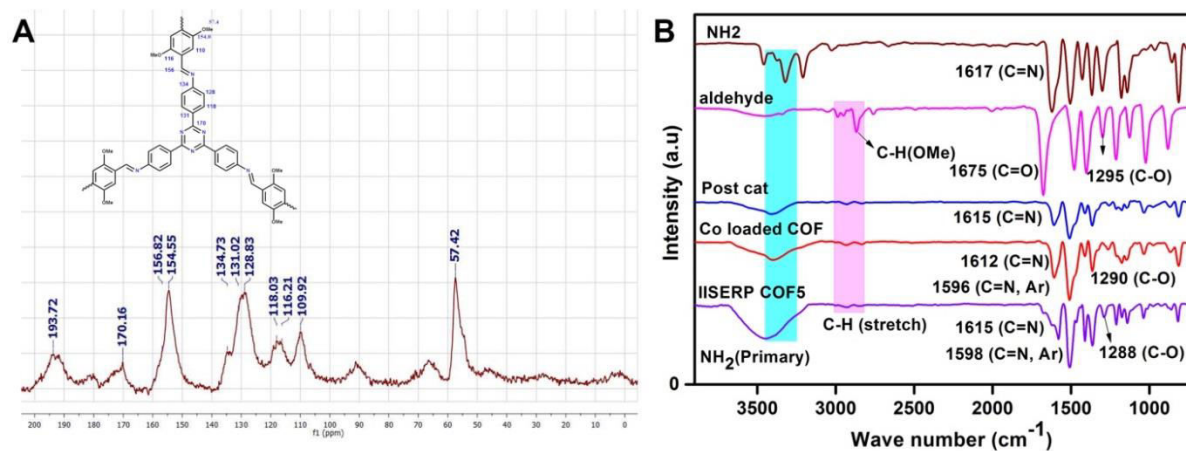


Figure 3.7. (A) A ChemDraw representation displaying the different unique carbon atoms in the IISERP-COF5 and the corresponding solid state ^{13}C -MASNMR spectrum. The peak at 193.72 ppm is due to the unreacted terminal aldehyde groups present in the framework. (B) Comparison of the IR spectra of the starting materials, IISERP-COF5, Co@IISERP-COF5 and post catalysis sample. The highlighted regions

indicate the peaks in the IISERP-COF5 due to the unreacted terminal aldehyde and amine functionalities and corroborate with SSNMR.

A 77K N₂ adsorption isotherm of IISERP-COF5 shows ~1000cc/g of N₂ uptake at 1 bar pressure with a mesoporous reversible type-2 profile (Figure 3.8A). We attribute this high N₂ uptake to the presence of highly ordered porous structure reflected in the high degree of crystallinity observed in the PXRD. A model-independent Barrett-Joyner-Halenda (BJH) fit to the desorption isotherm exhibits the presence of uniform ~36Å pores with a pore volume of 1.154 cc/g (Figure 3.8B). The BET surface area was estimated to be 1036 m²/g. A DFT model fit to the cylindrical carbon at 77K N₂ yielded a surface area of 1305 m²/g and a pore volume of 1.37 cc/g. This high porosity is drastically reduced (up to 85%) upon loading of Co np (~16 wt%) as evidenced from the 77K N₂ isotherm (Figure 3.8B), thus suggesting that the majority of the cobalt nanoparticles were loaded in the pores of the COF.

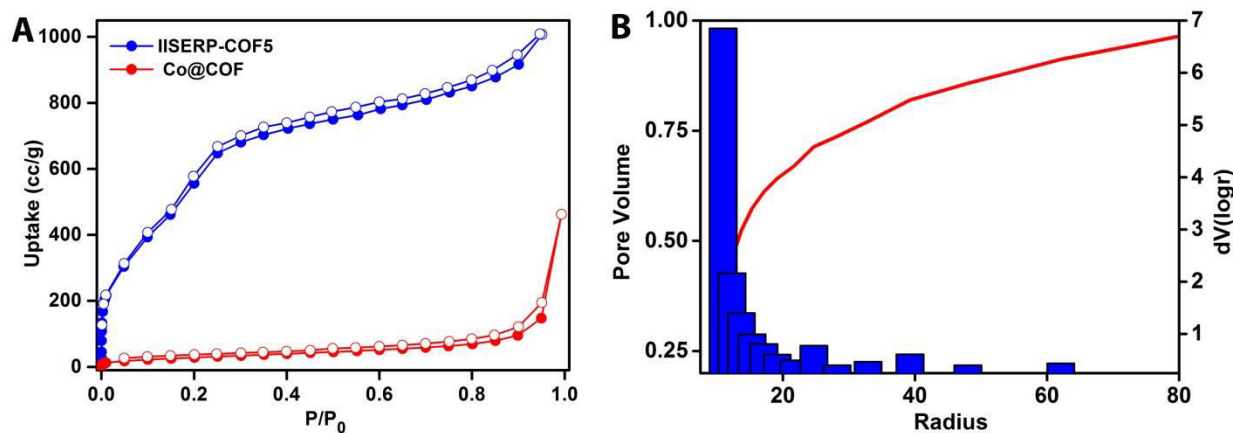


Figure 3.8. (A) Comparison of N₂ adsorption isotherms of the IISERP-COF5 and the Co@IISERP-COF5 measured at 77K. (B) Shows the BJH pore size distribution of the as-made IISERP-COF5.

The Co@IISERP-COF5 display a fluffy cotton-like morphology under the SEM, they appear to be aggregates of flaky crystallites under the TEM (Appendix 3.1). The particle size estimate from HR-TEM suggests the majority of the nanoparticles being in the range of 3–5 nm (Figure 3.9). It is important to realize that a significant amount of the nps are above the limiting pore size of the COF (40 Å) (Figure 3.4). The lattice fringes observed in the HR-TEM indexed to a d-spacing of 0.21 nm (Figure 3.9), which corresponds to cubic cobalt metal (Co metal; ICSD: α -Co (metal), 05-0727). Whereas, the XPS measurements shown binding energies at 781.1 eV correspondings to the Co-2p_{3/2} levels of Co(OH)₂ (Figure 3.9)⁵. This indicates that the

surface of the Co-metal is hydroxylated under the aqueous phase reduction that has been employed in their synthesis. To gain further evidence, in an XPS experiment, the top layers of the Co@IISERP-COF5 is peeled using sputtering, the resulting spectra shows lower binding energy of metallic cobalt peak at 778.2 eV. These results clearly indicating most of Co metal on the COF surface hydroxylated and the majority of nanoparticles were loaded inside the pores. The best distinction between Co(OH)_2 , Co_3O_4 , CoO and Co , comes from their magnetic properties.

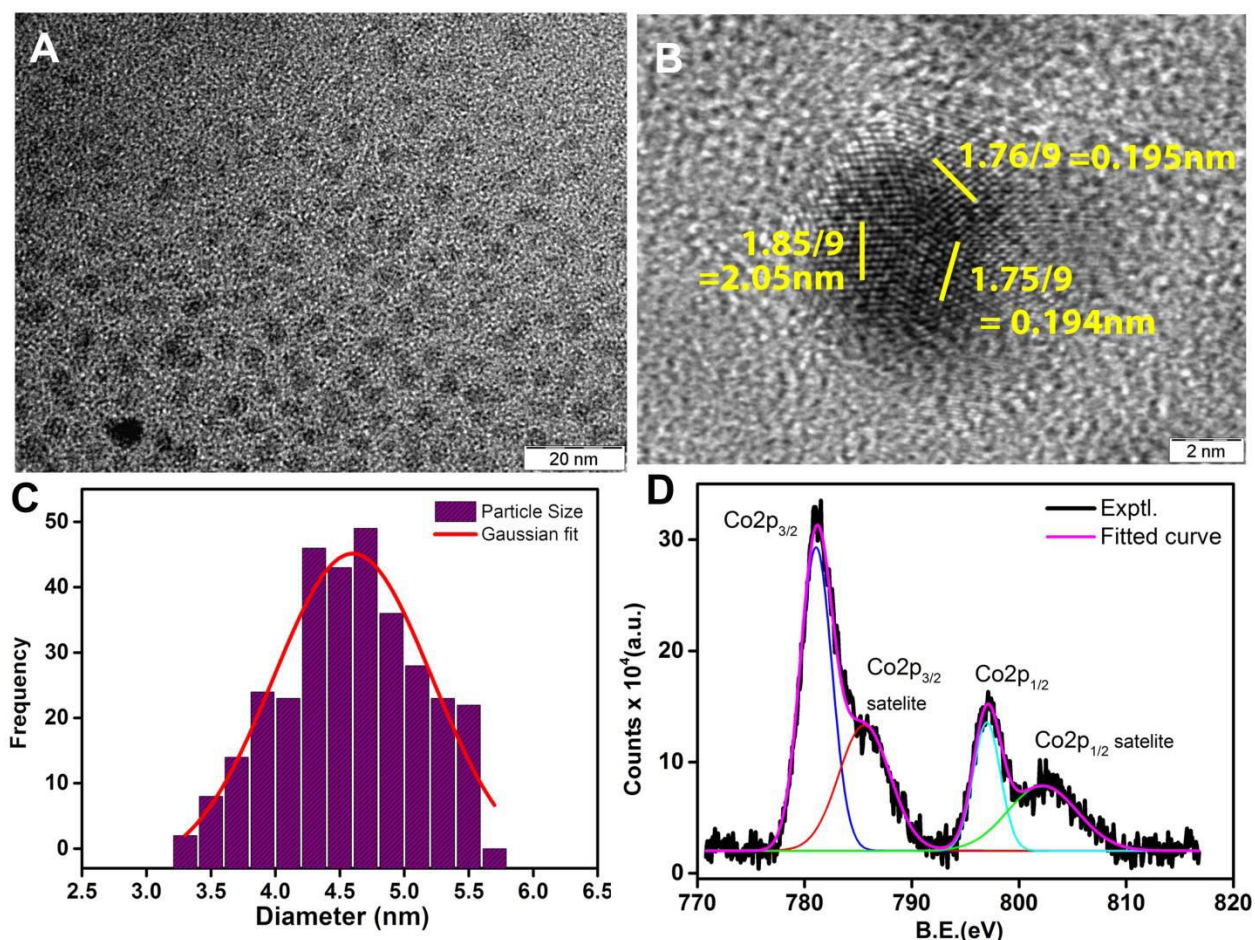


Figure 3.9. (A). HR-TEM image of the Co@IISERP-COF5 showing the uniform distribution of Co nanoparticles. (B). Lattice fringes indexing shows metallic cobalt. (C) Particle size distribution calculated from HR-TEM image gives average sizes in the range of 3-6nm (D) The XPS spectra of Co@IISERP-COF5 showing the characteristic binding energy for the Co(OH)_2 .

In bulk, both the hydroxide and the oxide of cobalt nanoparticles are anti-ferromagnetic at room temperature¹⁹, while the *metallic* cobalt is ferromagnetic even at a temperature as high as 350°C ²⁰. Interestingly, our Co@IISERP-COF5 is a room-temperature ferromagnet and the entire

bulk of the sample is homogeneously attracted by permanent magnets (Figure 3.10), confirming that this is not a mere heterogeneous mixture of IISERP-COF5 and ferromagnetic nanoparticles. In fact, this is another excellent proof for the formation of true composite between COF and metal derived nanoparticles⁵. Co_3O_4 when grown as small nanoparticles is known to exhibit weak ferromagnetism at room²⁰, while amorphous nanoparticles of $\text{Co}(\text{OH})_2$ with unusual ferromagnetic character is reported, but they show characteristic hysteresis only below 10K temperature²¹. Here we have a room temperature ferromagnet, which suggests that the majority of the nanoparticles are *metallic cobalt* and not $\text{Co}(\text{OH})_2$ or Co_3O_4 nanoparticles. However, magnetization does not saturate even at higher fields implying the presence of small amounts of some paramagnetic or anti-ferromagnetic impurity.

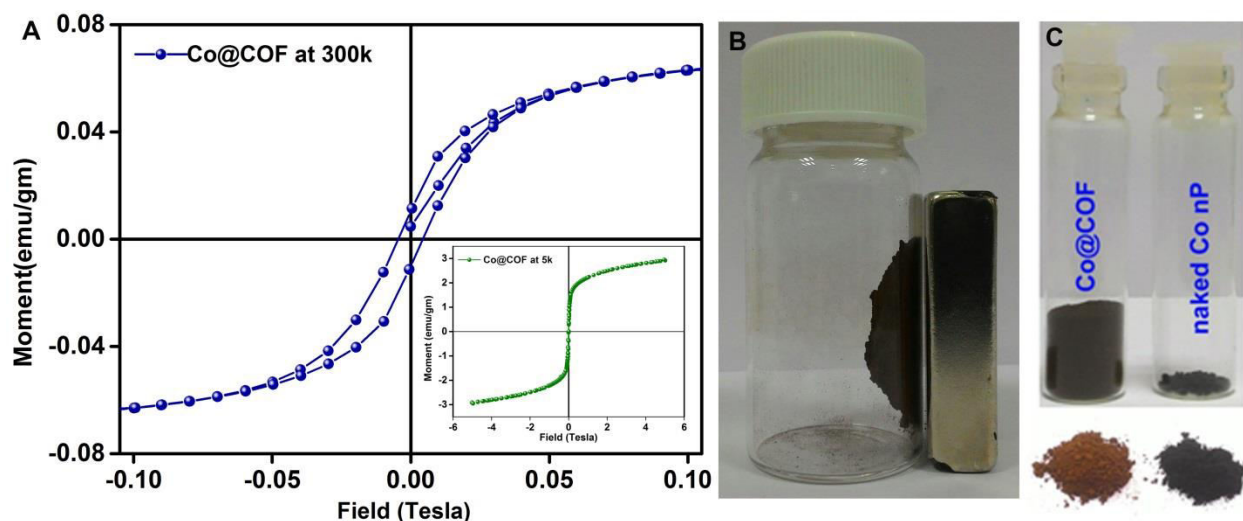


Figure 3.10. (A) A room-temperature magnetism data showing the ferromagnetic character of the Co@IISERP-COF5. The inset shows the hysteresis from a 5K measurement. (B) Photographic image of Co@IISERP-COF5 showing room-temperature ferromagnet (C) A mass-volume comparisons of Co@IISERP-COF5 and neat Co metal nps synthesized under the same condition.

The lattice fringes calculated from several HR-TEM images were indexed to 0.19 or 0.205 nm (α -Co (metal), Figure 3.9, Appendix 3.1) and none of them had the characteristic d-spacing expected for the Co_3O_4 (0.46nm) or the CoO (0.24nm) or the $\text{Co}(\text{OH})_2$ (0.27nm). But, in the XPS, a feature corresponding to cobalt metal ($\text{Co-}2p_{3/2} = 778.1$ eV) was absent and only the peak corresponding to hydroxide was observed ($\text{Co-}2p_{3/2} = 781.1$ eV). This is in contrast with the observations from HR-TEM lattice imaging. Additionally, the magnetic measurements shows room temperature ferromagnet. Therefore coupling the observations from XPS, HR-TEM and

the magnetism, we most likely have a cobalt metal hydroxylated on the surface. A mass-balance comparison visibly suggests that the particles of Co@IISERP-COF5 are 6.25 times lighter than the unsupported Co/Co(OH)₂ synthesized under similar condition(Figure 3.10C). Thus the Co@IISERP-COF5 represents a lightweight room temperature ferro-nanomagnet.

3.5. Catalytic Studies of Co@IISERP-COF5

3.5.1. Hydrogen Evolution from Chemical Hydrides

To evaluate the catalytic activity of Co@IISERP-COF5 we have performed hydrogen evolution reactions from the chemical hydrides (NaBH₄, NH₂NH₂, BH₃NH₃ and HCOOH) and evolved H₂ was monitored using a simple gas displacement cell. In a typical reaction, a flask containing 10 mg of pre-activated Co@IISERP-COF5 catalyst and 1ml of an alkaline solution of chemical hydrides (NaBH₄ or NH₂NH₂ or BH₃NH₃) were injected. This reaction immediately sets-off the release of H₂ visualized from continuous bubbling (Figure3.11). The released hydrogen was measured using the water-displacement method at different temperatures and the quantity of H₂ evolved as a function of time reveals the abrupt change of kinetics (Figure 3.11B). The total estimated, the H₂ volume is reached the theoretical limit of 98.8mL (with NaBH₄) in < 6 mins at 20°C. The same could be achieved in < 2 mins at 50°C (Figure 3.11). This is much faster compared to the Pt-LiCoO₂ (15mins) reported by Inokawa et al., which is among the best-performing catalyst⁷. The activation energy (E_a) was calculated from the Arrhenius relation found to be 48 kJ/mol, which is comparable to the lowest activation energies reported for any Co-based catalysts (less than 50 kJ/mol)²². Moreover, the production of H₂ remained the same even after five conjugative runs indicating the high durability of catalysts in NaBH₄ hydrolysis (Figure.3.11)

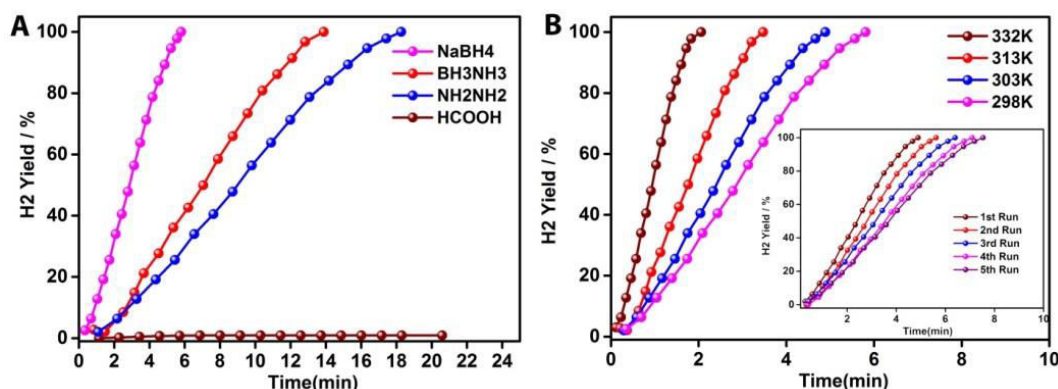


Figure 3.11. (A) Co@IISERP-COF5 catalyzed H₂ Evolution from various chemical hydrides. (B) H₂ evolution from NaBH₄ at different temperatures. The inset shows recycling studies.

3.5.2. Hydrogenation of Nitro (-NO₂) Compounds

The evolved hydrogen from the NaBH₄ was used in-situ for the hydrogenation of nitro (-NO₂) compounds to corresponding primary amines (-NH₂). Interestingly, our Co@IISERP-COF5 catalyst shown good activity (yields up to 99%) for all the donating, withdrawing substituents and obtained high TON (up to 2500), TOF (up to 2500) Table 2.1. Encouraged by these results we further extended our studies on highly complicated cyano (-CN) compound reduction reactions.

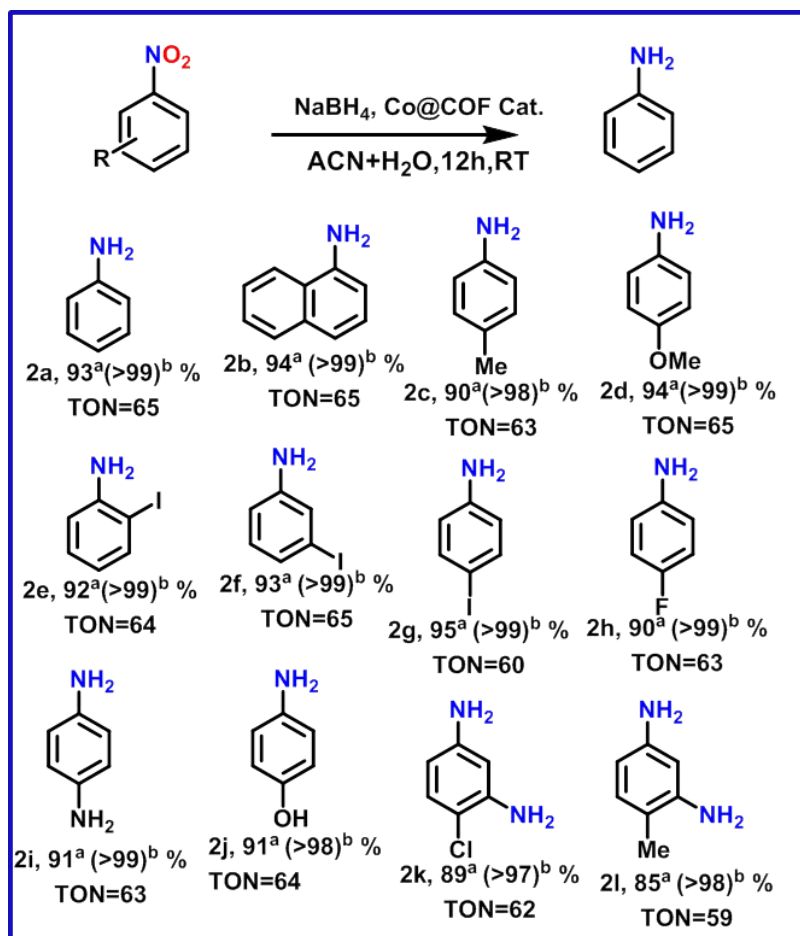


Table 3.3. Catalytic Hydrogenation of nitro compounds to corresponding amines catalyzed by Co@IISERP-COF5. Reaction condition 0.0075 mmol of Co@IISERP-COF5 catalyst, 0.5mmol of nitroarenes, 2.5 mmol of NaBH₄ and 3mL of ACN, 0.5 mL of H₂O were stirred in a sealed pyrex tube for 12hr at RT. ^a isolated yields. ^bGC Yields. % of yield = (Actual weight of the yield/ predicted weight of the product)*100 ; TON (Turnover number) calculation = moles converted / moles of active sites; TOF (Turnover frequency) = TON/Time hours.

3.5.3. Hydrogenation of Cyano (-C≡N) Compounds

The reactions were carried out by using Co@IISERP-COF5 catalyst and NaBH₄ into a methanolic solution of the cyano (-CN) substrates at room temperature for 3-12hrs. Remarkably, in all cases the catalyst showed excellent activity; high conversion (> 93-99% for the aromatic substrates and 82-86% for the aliphatic ones) and good selectivity towards primary amines were achieved. The TOF for these nitrile reductions were 25-30 hr⁻¹, which is quite reasonable for a non-noble metal based heterogeneous catalyst²³.

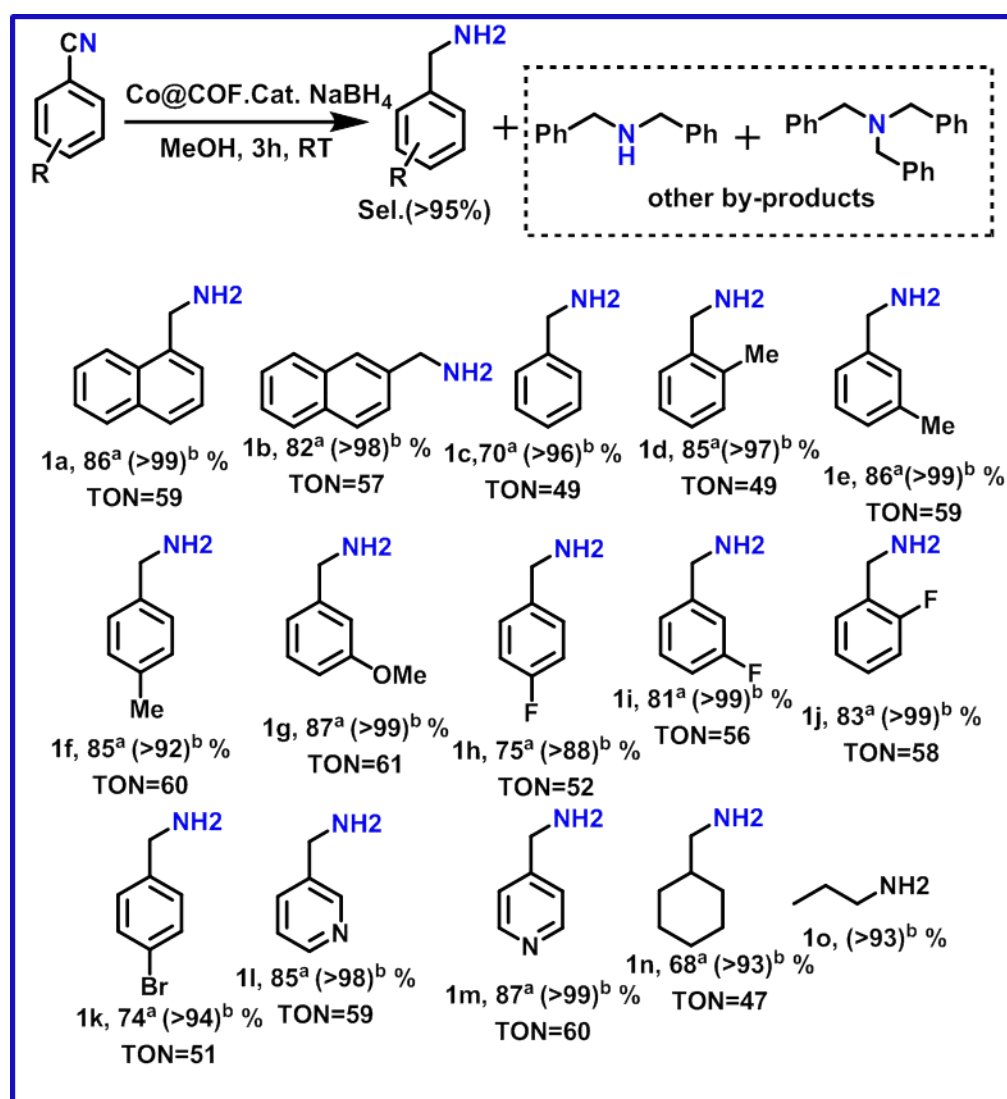


Table 3.4. A schematic illustration of the catalytic nitrile to amine conversion. Reaction conditions: 0.0075 mmol of Co@IISERP-COF5 catalyst (1.5 mol%), 0.5mmol of nitrile, 2.5 mmol of NaBH₄ and 3mL of MeOH at RT for 3hrs. The substrates have been shown with their ^aisolated % yields, ^b(% GC conversion shown in brackets).

3.5.4. Recyclability and Durability Studies

For assessing the potential leaching of the nanoparticles from COF surface, a post catalysis supernatant solution was analyzed under SEM-EDAX analysis and no trace of Co signal was observed. Also, neither the hydrogen evolution nor the nitrile reduction was observed when this supernatant was employed in place of the catalyst indicating the lack of nanoparticle leaching and also suggesting strong binding of Co nps with the COF5. To further evidence the role of the COF in the catalysis, we synthesized the unsupported catalyst Co/Co(OH)₂ nanoparticles and investigated its activity towards the nitro/nitrile reductions. The hydrogenation of benzonitrile occurred with only about 30% conversion, in < 20% yield, even after 48hrs (with our cat, 98% within 3hrs).

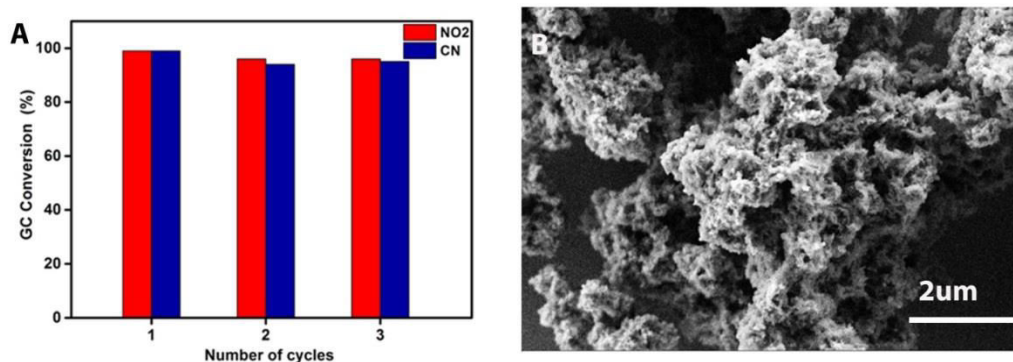


Figure 3.12. (A) A bar chart showing the yield of products obtained in the recycle studies. Reaction condition: for the nitro (-NO₂) reduction reaction 0.5 mmol of 4-nitrophenol, 0.0075 mmol of Co@IISERP-COF5 catalyst, 2.5 mmol of NaBH₄, and 3ml of ACN, 0.5ml of H₂O at RT 12hrs. For the nitrile reduction reaction 0.5 mmol of 1-Naphthonitrile, 0.0075 mmol of Co@IISERP-COF5 catalyst, 2.5 mmol of NaBH₄, and 1ml of MeOH at RT 3hrs. (B) SEM image of post catalysis shows no considerable change in morphology.

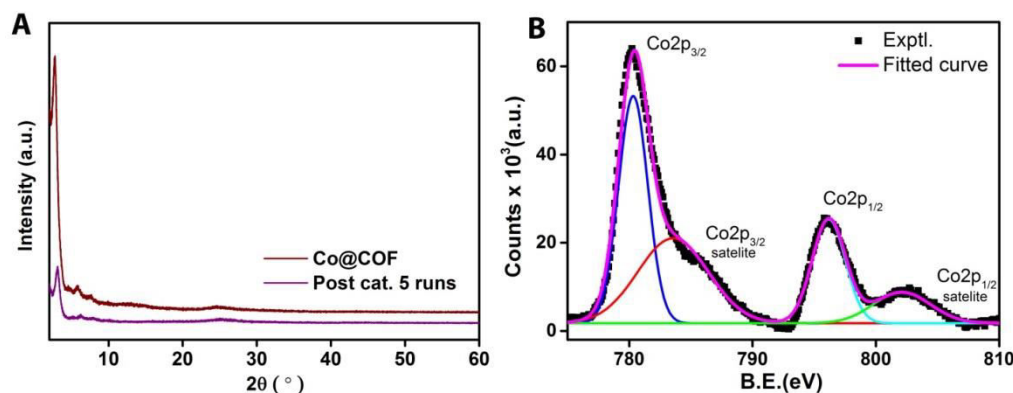


Figure 3.13. A) Comparison of the powder X-ray diffraction patterns of the Co@COF and the post-catalysis Co@IISERP-COF5. (B) XPS spectra of a sample subjected to 5 runs.

3.6. Computational Modeling of the NaBH_4 Activation on the Co@IISERP-COF5 Surface

The advantage of this nano-confinement in exposing the nanoparticles facets and its potential impact on the activation of NaBH_4 is modeled via computational methods. For understanding the energy associated with the growth of the Co/Co(OH)_2 clusters within the nano-confinement of the IISERP-COF5, we developed 'frustum' nanoclusters from the typical hexagonal close-packed cobalt lattice (Space group.: $P6_3/mmc$; $a = 2.77$; $c = 4.10 \text{ \AA}$). The cleaved bonds at the shape boundaries of the cluster were capped by hydroxyl oxygen atoms, giving it a Co/Co(OH)_2 structure which corresponds to what is observed from HR-TEM and XPS analysis. The frustum clusters were grown along five different facets- (100), (010), (002), (101), and (111) (Figure 3.14). Note: The (002) and (101) are the facets predominantly observed under the HR-TEM images. Each cluster was dispersed in the IISERP-COF5 lattice using a simulated annealing routine. Following this, a $4 \times 4 \times 4$ unit cell of the Co@IISERP-COF5 was geometry optimized using the *Forcite* package material studio. The relative energies of these different Co@IISERP-COF5 configurations are presented in Figure 3.14. The cluster grown along the (101) facet had the lowest relative energy over others.

The activation of the $[\text{BH}_4]^-$ ions, from the NaBH_4 , by the catalyst surface directly decides the efficiency of the H_2 evolution and in turn the tandem reduction reactions. To elucidate how these nanoclusters can serve as a high activity catalyst in activating the $[\text{BH}_4]^-$

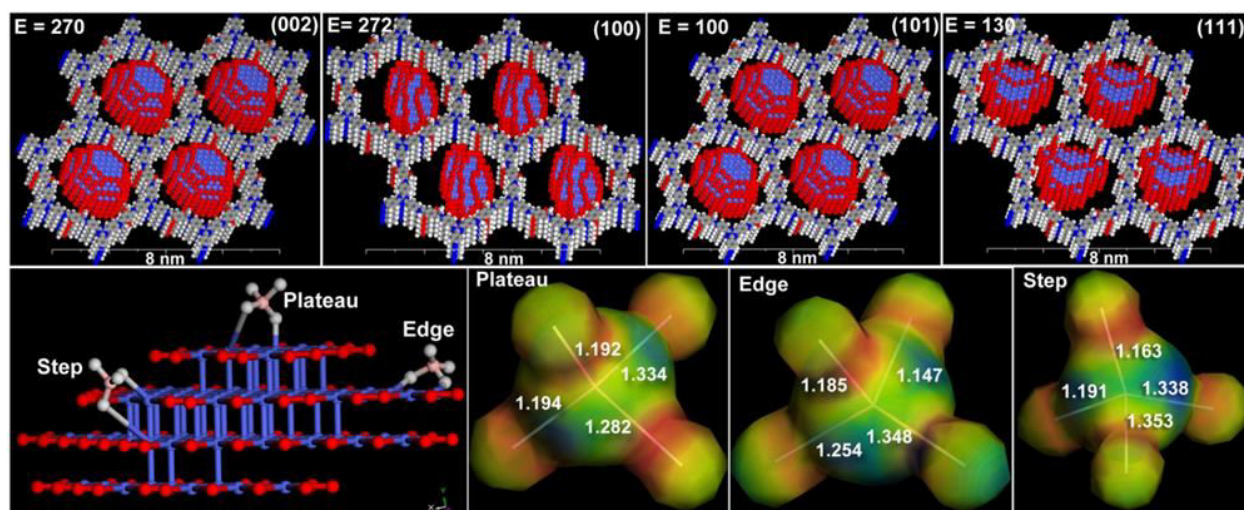


Figure 3.14. Top: Optimized structure of Co/Co(OH)_2 clusters in COF. The clusters are grown from different basal planes. The relative energies are represented as 'E' in units of kcal/mol. Bottom: The $[\text{BH}_4]^-$ ions geometry optimized at the different energetic positions of the Co/Co(OH)_2 cluster grown from the

(101) basal plane. The electrostatic potentials calculated from DMol³ showing the activated [BH₄]⁻ ions at these different sites on the cluster. The hydrogens of the capping hydroxyls have not been shown.

ions, we calculated the energy associated with the activation of the reactant and substrates on the surface of these clusters. For this, we bonded the [BH₄]⁻ ions on the 'plateau', 'step' and the 'edge' of the cluster grown along the [101] facet and minimized its geometry and energy using DMol³ package, which yielded some fascinating results. The borohydride gets activated and the Co...H-B bond attached to the cobalt surface gets elongated, this is manifested by the marked change in B-H bond lengths and the change in electron distribution which is visualized from the potential maps (Figure 3.14). From the figure, it can be seen that this energy associated with the activation is slightly different for each facet. We believe, this is where the role of COF in exposing the specific facets becomes crucial. Importantly, all these clusters seem to stabilize to a small size in the nano-confinement of the COF, however the cluster exposing the (101) facet has the lowest relative energy, which corroborates well with it being the most frequently observed facet under the HRTEM (Figure 3.9 and 3.11). It is important to underscore the fact that the crystalline structure of the COF enables these atomic-level computations.

Elucidating the ability of COF to stabilize clusters larger than its limiting pore size- an ubiquitous observation: As mentioned earlier, significant amount of the nps have sizes larger than the limiting pore-size (~40 Å) of the COF. Rationally, such large particles would be expected to leach from the surface of the support, particularly under the harsh reaction conditions. For assessing the potential leaching of the nanoparticles from the COF surface, a post catalysis supernatant solution was analyzed under SEM-EDAX and no trace of cobalt signal was observed. Also, neither the H₂ evolution nor the nitrile (-CN) reduction was observed when this supernatant was employed in place of the Co@IISERP-COF5 catalyst indicating the lack of nanoparticle leaching, it suggesting strong binding of the nanoparticles with the IISERP-COF5. How do such particles exceeding the limiting pore size (40 Å) of the IISERP-COF5 manage to adhere so strongly?

In fact, this is an ubiquitous observation in supported catalyst systems^{1d,1g, 2,5, and 24}. Thus, providing a plausible explanation for this would be of immense value. We realize that in these porous supports, the clusters could be growing from within the pores and the growth can extend beyond the pore dimension (~40 Å) (Figure 3.5). And in such scenario, the particles found under

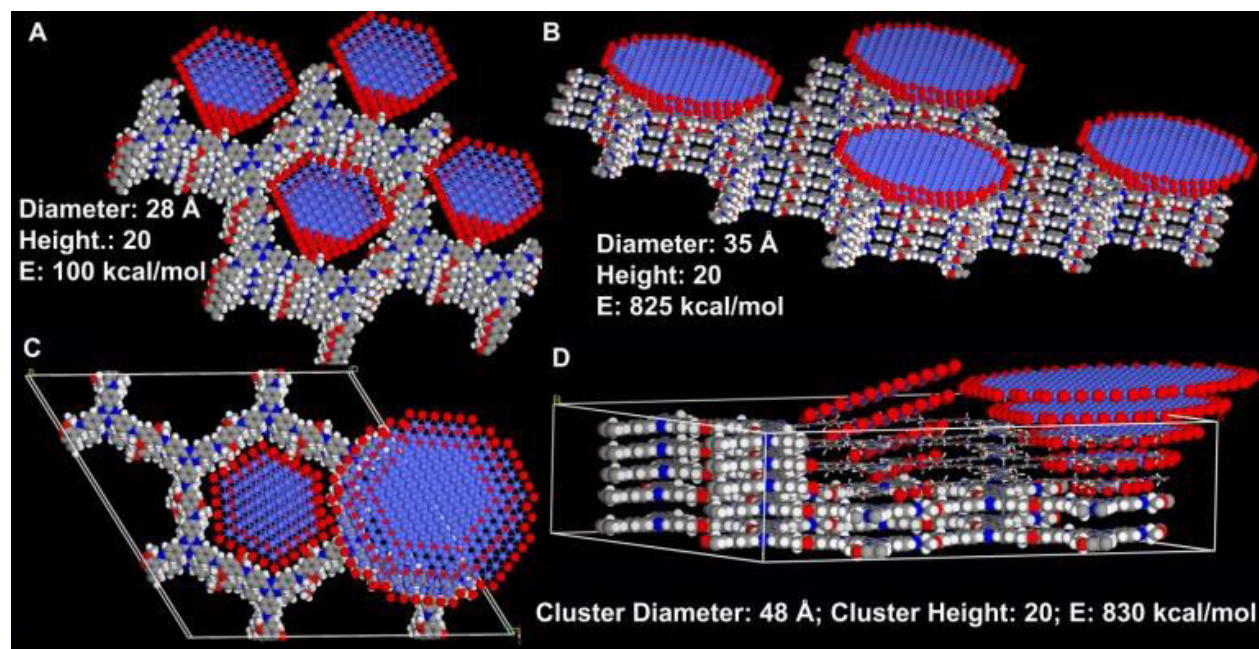


Figure 3.5. DFT optimized Co@IISERP-COF5 with increasing sizes of Co/Co(OH)₂ clusters. (A) Small cluster fitting the pore (~28 Å). (B) Large cluster with a cone shape (35 Å pore). The narrow apex is buried in the pores of the COF, while the wider base is projecting out of the COF pore. The cluster is stabilized (825 kcal/mol) within the pores by the narrow apex. (C) and (D) COF with both small and large clusters (diameter > the limiting pore size (~40 Å) of the COF).

the TEM can be larger than the COF's limiting pore-size. Since they are anchored to the support by the part of the cluster residing within the pores, they do not leach out. A DFT geometry-optimization using a 2 x 2 x 5 cell reveals that such clusters can be stabilized within the COF matrix, but the larger clusters tend to have higher relative energy (Figure 3.5). Importantly, excellent convergence with acceptable geometries and energies were obtained for all three configurations, suggesting they all can be expected to form under the experimental conditions (Figure 3.5). However, when a cluster of very large size (Diameter- 6nm; Height- 5 layers) was attempted, a stable configuration for the Co@IISERP-COF5 could not be obtained using the DFT minimizations and the energies were unacceptably large.

3.7. Summary

In summary, we have developed a non-noble metal heterogeneous catalyst (Co@IISERP-COF5) comprising of surface hydroxylated cobalt nanoparticles supported on a N-rich COF. The Co/Co(OH)₂@IISERP-COF5 composite containing about 16 wt% of < 6 nm sized Co/Co(OH)₂ nanoparticles. It catalyzes the hydrogenation of nitro/nitrile compounds in the presence of readily

available and safe NaBH_4 under ambient conditions with excellent yields and good recyclability. The COF “by choice” is built from “methoxy” functional groups, this plays a crucial role in stabilizing Schiff bond and enabling the complete retention of the COF structure under the strong reduction conditions of the catalysis, where the regular Schiff bonds would most likely have hydrolyzed. Interestingly, these cobalt nanoparticles ($\text{Co}/\text{Co}(\text{OH})_2$) loaded in IISERP-COF5 is a room temperature ferro-nanomagnet, which is 6.25 times lighter than the neat nanoparticles. This indicates the high dispersivity of these small uncapped nanoparticles in the pores of the COF. Density Functional Theory (DFT) geometry and energy-optimized structures of $\text{Co}@$ IISERP-COF5 and the electrostatic potentials for the $[\text{BH}_4]^-$ ions activated on the nanoparticle surface displays how the COF modulates the catalytic activity by exposing specific facets of the cluster.

3.8. References

1. (a) Waller, P. J.; Gándara, F.; Yaghi, O. M.; *Acc. Chem. Res.* **2015**, *48*, 3053-3063. (b) Segura, J. L.; Mancheno, M. J.; Zamora, F.; *Chem. Soc. Rev.* **2016**, *45*, 5635-5671. (c) Ding, S. Y.; Gao, J.; Wang, Q.; Zhang, Y.; Song, W. G.; Su, C. Y.; Wang, W. *J. Am. Chem. Soc.* **2011**, *133*, 19816-19822. (d) Pachfule, P.; Panda, M. K.; Kandambeth, S.; Shivaprasad, S. M.; Díaz, D. D.; Banerjee, R. *J. Mater. Chem. A.* **2014**, *2*, 7944-7952. (e) Du, Z.-L.; Dang, Q.-Q.; Zhang, X.-M.; *Ind. Eng. Chem. Res.* **2017**, *56*, 4275-4280. (f) Shi, X.; Yao, Y.; Xu, Y.; Liu, K.; Zhu, G.; Chi L.; Lu, G. *ACS Appl. Mater. Interfaces* **2017**, *9*, 7481-7488. (g) Pachfule, P.; Kandambeth, S.; Díaz D. D.; Banerjee, R. *Chem. Commun.* **2014**, *50*, 3169-3172. (h) Zhi, Y.; Li, Z.; Feng, X.; Xia, H.; Zhang, Y.; Shi, Z.; Mua, Y.; Liu, X. *J. Mater. Chem. A.* **2017**, *5*, 22933-22938.
2. Mullangi, D.; Nandi, S.; Shalini, S.; Sreedhala, S.; Vinod, C. P.; Vaidhyanathan, R. *Sci. Rep.* **2015**, *5*, 10876.
3. Ansari, A.; Jayapal, P.; Rajaraman, G. *Angew. Chem. Int. Ed.* **2015**, *54*, 564-568.
4. Chirik, P. J. *Acc. Chem. Res.*, **2015**, *48*, 1687-1695.
5. (a) Mullangi, D.; Dhavale, V.; Shalini, S.; Nandi, S.; Collins, S.; Woo, T.; Kurungot, S.; Vaidhyanathan, R.; *Adv. Energy Mater.* **2016**, *6*, 1600110. (b) Nandi, S.; Singh, S. K.; Mullangi, D.; Illathvalappil, R.; George, L.; Vinod, C. P.; Kurungot, S.; Vaidhyanathan, R. *Adv. Energy Mater.* **2016**, *6*, 1601189.

6. Banerjee, T.; Haase, F.; Savasci, G.; Gottschling, K.; Ochsenfeld, C.; Lotsch, B. V. *J. Am. Chem. Soc.* **2017**, 139, 16228–16234.
7. (a) Inokawa, H.; Driss, H.; Trovela, F.; Miyaoka, H.; Ichikawa, T.; Kojima, Y.; Zaman, S. F.; Al-Zahrani, A.; Alhamed, Y.; Petrov, L. *Int. J. Energy Res.* **2016**, 40, 2078-2090. (b) Mao, J.; Gregory, D. *Energies* **2015**, 8, 430-453.
8. (a) Göksu, H.; Ho, S. F.; Metin, Ö.; Korkmaz, K.; Garcia, A. M.; Gültekin, M. S.; Sun, S. *ACS Catalysis* **2014**, 4, 1777-1782. (b) Zhu, Q. L.; Li, J.; Xu, Q. *J. Am. Chem. Soc.* **2013**, 135, 10210-10213.
9. (a) Yadav, M.; Xu, Q.; *Energy Environ. Sci.* **2012**, 5, 9698-9725. (b) Brack, P.; Dann, S. E.; Wijayantha, K. G. U. *Energy Sci. Eng.* **2015**, 3, 174-188.
10. (a) Mahmood, J.; Jung, S.-M.; Kim, S.-J.; Park, J.; Yoo, J.-W.; Baek, J.-B. *Chem. Mater.*, **2015**, 27, 4860-4864. (b) Zhang, H.; Ling, T.; Du, X.-W. *Chem. Mater.* **2015**, 27, 352-357.
11. (a) Jia, C. J.; Schuth, F. *Phys. Chem. Chem. Phys.* **2011**, 13, 2457-2487. (b) Bhumkar, D. R.; Joshi, H. M.; Sastry, M.; Pokharkar, V. B. *Pharma. res.* **2007**, 24, 1415-1426.
12. Enthaler, S.; Junge, K.; Addis, D.; Erre, G.; Beller, M.; *ChemSusChem* **2008**, 1, 1006-1010.
13. Ji, P.; Manna, K.; Lin, Z.; Feng, X.; Urban, A.; Song, Y.; Lin, W. *J. Am. Chem. Soc.* **2017**, 139, 7004-7011.
14. (a) Westerhaus, F. A.; Jagadeesh, R. V.; Wienhofer, G.; Pohl, M. M.; Radnik, J.; Surkus, A. E.; Rabeah, J.; Junge, K.; Junge, H.; Nielsen, M.; Bruckner, A.; Beller, M. *Nat. Chem.* **2013**, 5, 537-543. (b) J. Long, K. Shen, Y. Li, *ACS Catalysis* **2016**, 7, 275-284. (c) Zhang, T.; Manna, K.; Lin, W. *J. Am. Chem. Soc.* **2016**, 138, 3241-3249. (d) Yang, H.; Bradley, S. J.; Chan, A.; Waterhouse, G. I.; Nann, T.; Kruger, P. E.; Telfer, S. G. *J. Am. Chem. Soc.* **2016**, 138, 11872-11881.
15. (a) Li, M.; Chen, G. *Nanoscale* **2013**, 5, 11919-11927. (b) Lee, J. H.; Hong, S. K.; Ko, W.B. *Asian J. Chem.* **2011**, 23, 2347-2350. (c) Feng, J.; Handa, S.; Gallou, F.; Lipshutz, B. H. *Angew. Chem. Int. Ed.* **2016**, 55, 8979-8983.
16. Chen, F.; Topf, C.; Radnik, J.; Kreyenschulte, C.; Lund, H.; Schneider, M.; Surkus, A. E.; He, L.; Junge, K.; Beller, M. *J. Am. Chem. Soc.* **2016**, 138, 8781-8788.

17. Kuhnert, N.; Rossignoloa, G. M.; Lopez-Periagoa, A. *Org. Biomol. Chem.*, **2003**, 1, 1157-1170 .
18. Xu, H.; Gao, J.; Jiang, D. *Nat. Chem.* **2015**, 7, 905-912.
19. Mousavand, T.; Naka, T.; Sato, K.; Ohara, S.; Umetsu, M.; Takami, S.; Nakane, T.; Matsushita, A.; Adschiri, T. *Phys. Rev. B.* **2009**, 79, 144411-144415.
20. de la Peña O'Shea, V. c. A.; de la Piscina, P. R. r.; Homs, N.; Aromí, G.; Fierro, J. L. G. *Chem. Mater.* **2009**, 21, 5637-5643.
21. Li, H. B.; Liu, P.; Liang, Y.; Xiao, J.; Yang, G. W.; *RSC Adv.* **2013**, 3, 26412-26417.
22. Zhang, H.; Ling, T.; Du, X.-W. *Chem. Mater.* **2015**, 27, 352-357.
23. Sun, X.; Olivos-Suarez, A. I.; Oar-Arteta, L.; Rozhko, E.; Osadchii, D.; Bavykina, A.; Kapteijn, F.; Gascon, J. *ChemCatChem* **2017**, 9, 1854-1862.
24. (a) Kaleeswaran, D.; Antony, R.; Sharma, A.; Malani, A.; Murugavel, R. *ChemPlusChem* **2017**, 82, 1253 (b) Ma, W.; Yu, P.; Ohsaka, T.; Mao, L.; *Electrochem. Commun.* **2015**, 52,53.

Chapter-3 Appendix

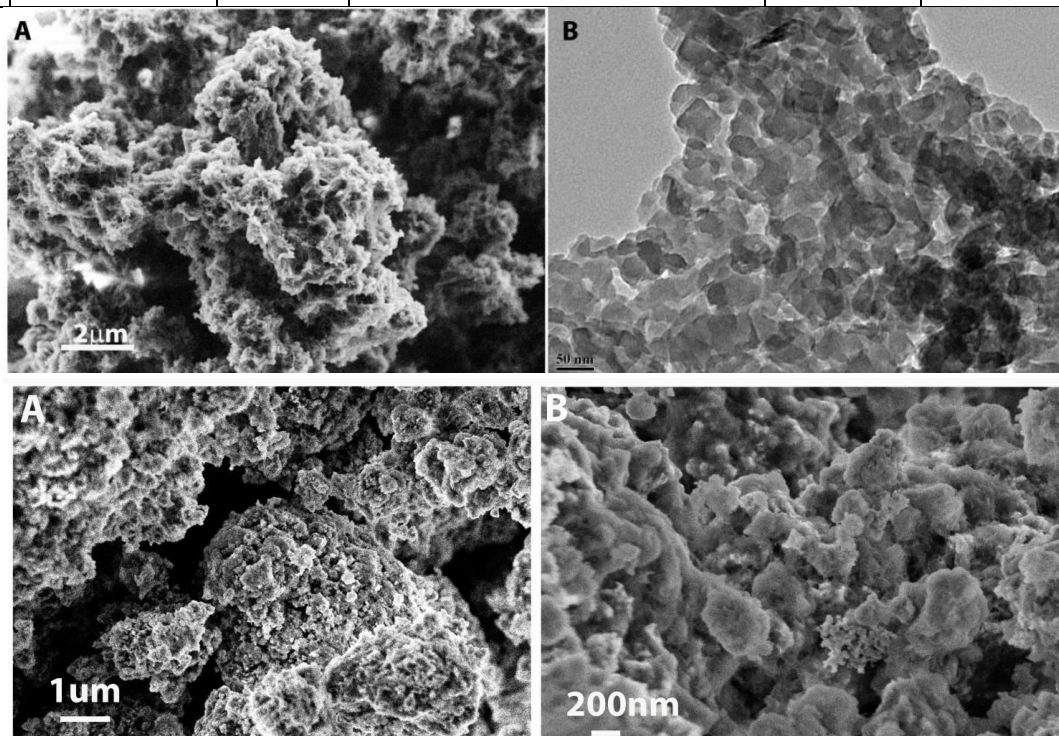
Appendix Table 1: Recent literature of the catalytic reduction of nitrile to amines by using various hydrogen source and heterogeneous catalysts.

Entry	Catalyst	Active metal	Reaction condition	H ₂ source	Reference
1	Co@IISERP-COF5	Co	0.5 mmol of nitriles, 0.0075mmol of catalyst, 2.5 mmol of NaBH ₄ , and 3ml MeOH, 0.5ml H ₂ O at RT 12hrs.	NaBH ₄	This work
2	[j3-(1-pz) ₂ HB(N=CHCH ₃)]Ru(cymene)+ TfO (pz = pyrazolyl)	Ru	5 mol% of Cat 4 eq. NaBH ₄ , 1 eq. NaOtBu MeOH, reflux, 12 h.	NaBH ₄	<i>Chem. Commun.</i> , 2014 , 50, 5391-5393
3	Zr ₁₂ -TPDC-Co	Co	0.5 mol% of catalyst, benzonitrile (42 μL, 0.4 mmol), toluene, 40 bar H ₂ , 110 °C, 42 h.	40 bar H ₂	<i>J. Am. Chem. Soc.</i> , 2017 , 139, 7004–7011
4	Co Catalyst on α-Al ₂ O ₃	Co	0.5 mmol of nitrile, 4 mol % of catalyst, under 40 bar H ₂ for 2 hrs 85°C	40 bar H ₂	<i>J. Am. Chem. Soc.</i> 2016 , 138, 8781–8788
5	Fe ₃ -O ₄ @nSiO ₂ @NiPd-PVP@mSiO ₂	PdNi	20 mmol substrate, 0.12 g catalyst, 1.5 MPa H ₂ 2hrs 100°C.	1.5 MPa H ₂	<i>J. Mater. Chem. A</i> , 2015 , 3, 19807–19814
6	Ru ₃ -CO/K-Alu C	Ru	3.96 mmol of nitrile, 0.0396 mmol of catalyst, 101.3 kPa of H ₂ , at 90°C for 20 min.	101.3 kPa H ₂	<i>Phys. Chem. Chem. Phys.</i> , 2015 , 17, 24791-24802
7	PNP pincer cobalt catalyst	Co	0.5 mmol of nitriles, 0.8 mmol of AB, 1 mol % catalyst and 1 mL of n-hexane at 50°C 16hrs.	BH ₃ NH ₃	<i>Angew.Chem.Int. Ed.</i> 2016 , 55,14653 –14657
8	Fe(PNP)Br ₂ complex	Fe	1 mmol nitrile , 60 bar H ₂ , and 2mL THF, heated in an autoclave at 140°C, 19-48hrs.	60 bar H ₂	<i>Chem. Commun.</i> , 2016 , 52, 1812-1815
9	Mo/WN(CH ₂ CH ₂ Pi Pr ₂) ₂	MoW	20 equivalent substrate relative to 5 mg catalyst, 5.0 mol% catalyst, 60 bar H ₂ , 2 mL of THF, at 140°C , 30min.	60 bar H ₂	<i>ACS Catal.</i> 2014 , 4, 2191–2194
10	[Ru(cod)(methylallyl) ₂]	Ru	0.5 mmol of nitrile, 0.5–2 mol% of catalyst, 15 bar H ₂ and 2 mL of dry iPrOH, 50°C, 3 hrs.	15 bar H ₂	<i>ChemCatChem</i> 2016 , 8,1329 –1334
11	Co PNNH pincer complex,	Co	1 mmol nitrile, 2.0 mol% catalyst, 2 mol% NaEt ₃ BH, 4.4 mol% NaOEt, 30 bar H ₂ , and 2 mL benzene, heated in an autoclave at 135 °C, 36hrs.	30 bar H ₂	<i>J. Am. Chem. Soc.</i> 2015 , 137, 8888–8891

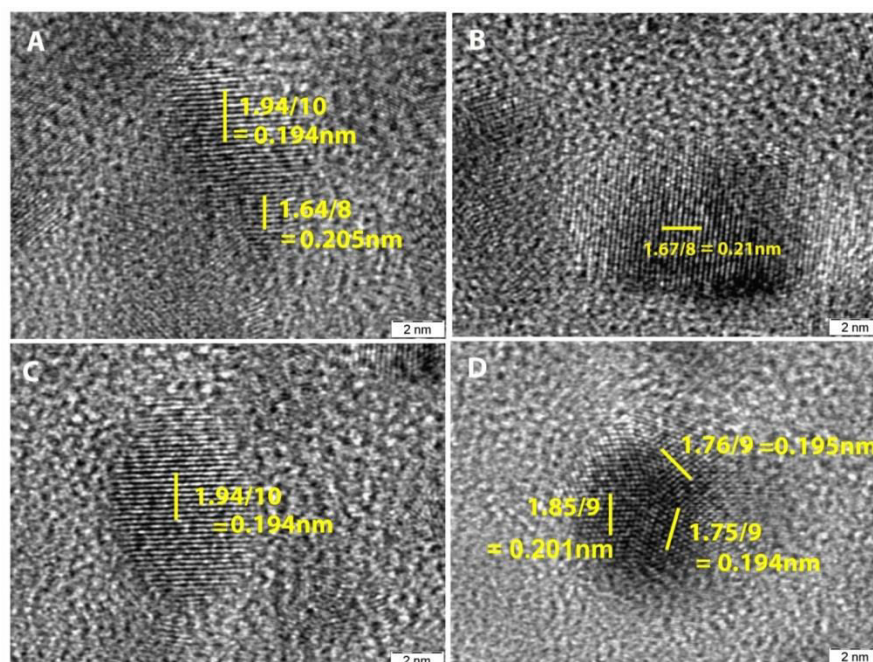
Appendix Table 2: Recent literature of the catalytic reduction of nitro to amines by using various hydrogen source and heterogeneous catalysts.

Entry	Catalyst	Active metal	Reaction condition	H ₂ source	Reference
1	Co@IISERP COF5	Co	0.5 mmol of nitroarenes, 0.0075 mmol of catalyst, 2.5 mmol of NaBH ₄ , and 3ml ACN, 0.5ml H ₂ O at RT 12hrs.	NaBH ₄	This work
2	Zr12-TPDC-Co	Co	0.5 mol% of catalyst, 1-nitronaphthalene (69 mg, 0.4 mmol), toluene, 40 bar H ₂ , 110 °C, 42 h.	40 bar H ₂	<i>J. Am. Chem. Soc.</i> , 2017 , 139, 7004–7011
3	PtCo@NHPC	PtCo	20mg of catalyst, 0.5mmol of the substrate, 6.8 bar H ₂ methanol, 50 °C, 40min.	6.8 bar H ₂	<i>J. Am. Chem. Soc.</i> 2016 , 138, 11872–11881
4	Fe/ppm Pd Nanoparticles	Pd-Fe	0.5 mmol of nitroarene, 6 mg of catalyst, 0.75–3.0 mmol of NaBH ₄ , and 2wt% PGS-750-M/H ₂ O (1 mL) at RT up to 24hrs.	NaBH ₄	<i>Angew. Chem.</i> 2016 , 128, 1 – 6
5	GO–Chit-Ag/AuNPs	Ag-Au	1 mmol of nitroarene, 50 mg of catalyst, 10 mmol of NaBH ₄ and 50 mL of water at RT 40-45hrs	NaBH ₄	<i>Phys. Chem. Chem. Phys.</i> , 2015 , 17, 11329–11340
6	Ru–BBA-1	Ru	0.5 mmol of nitroarene , 5 mg Ru-A catalyst, 2.5 mmol of NaBH ₄ and (THF/H ₂ O (1:3 v/v) at RT 30-120min	NaBH ₄	<i>Chem. Eur. J.</i> 2015 , 21, 19016 – 19027
7	Pd@OIP-1	Pd	0.5 mmol of nitroarene, 1 mol% of catalyst, 2.5 mmol of NaBH ₄ at 25° C, 1.5 h.s	NaBH ₄	<i>Chem. Commun.</i> , 2014 , 50, 10871–10874
8	Porous Pd nanoclusters	Pd	2 mmol of nitrophenol, 1.6-3.0 mol Pd nanoclusters and 0.03 mmol of NaBH ₄	NaBH ₄	<i>Nanoscale</i> , 2011 , 3, 725–730
9	DACH-Pd-β-CD	Pd	1.0 mmol of nitroarene, 3mmol of NaBH ₄ , 11.9 mg of catalyst and 2mL water at RT 3hrs	NaBH ₄	<i>RSC Adv.</i> , 2016 , 6, 7950–7954
10	PGMA@PAH @AuNP	Au	p-nitrophenol = 0.125 mmol, NaBH ₄ = 50 mmol, AuNPs = 4.4357x10 ⁻¹² mol, T = 295 K.	NaBH ₄	<i>Nanoscale</i> , 2013 , 5, 11919–11927
11	Pd/AIO(OH) NPs	Pd	1 mmol nitroarene, 25 mg of catalyst, 3 mmol NaBH ₄ , and 1 ml of water/methanol (v/v = 7/3) at RT for14- 50min	NaBH ₄	<i>New J. Chem.</i> , 2015 , 39, 8498 – 8504
12	Graphene-Supported NiPd Alloy Nanoparticles	Pd-Ni	1 mmol of substrate, 4 mg of catalyst (25 wt % metal content), 3 mmol NH ₃ BH ₃ , , 10 mL of water/methanol (v/v = 3/7), and RT for 5-10min.	NH ₃ BH ₃	<i>ACS Catal.</i> 2014 , 4, 1777–1782

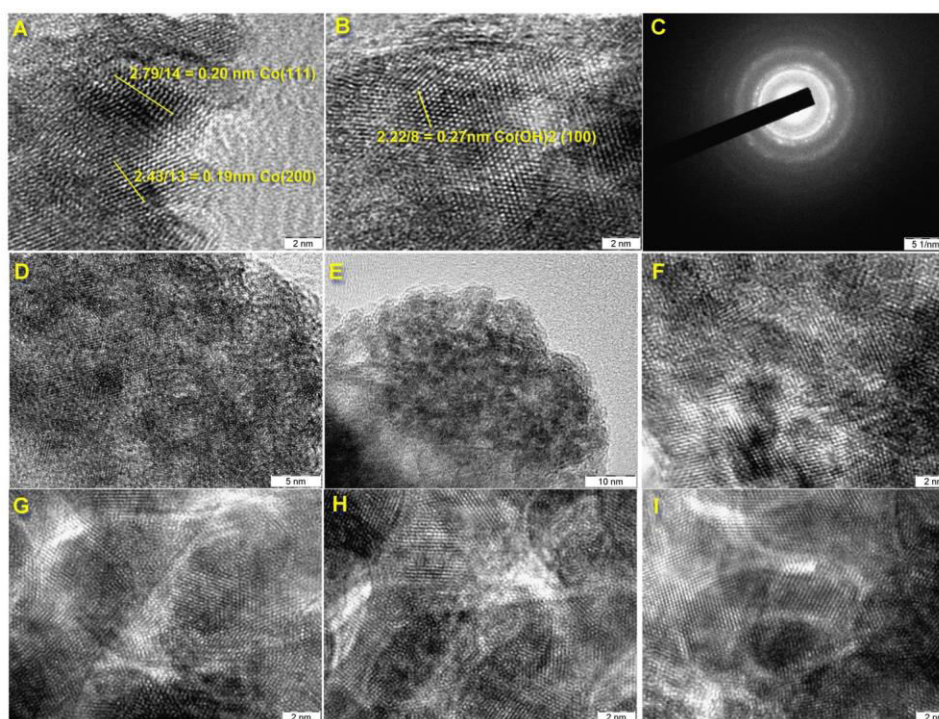
13	Pd-Pt-Fe ₃ O ₄ Nanoflakes	Pt-Pd	0.5 mmol of the substrate, 1 mol % of Pd-Pt-Fe ₃ O ₄ catalyst, 1.5 mmol of NH ₃ BH ₃ and 5 mL of methanol, at RT 5min	NH ₃ BH ₃	<i>ACS Appl. Mater. Interfaces</i> 2016 , 8, 14637–14647
14	MOF-derived Co-CoO@N- doped porous carbon	Co-CoO	0.2 mmol nitro compound, 0.6 mmol NH ₃ BH ₃ , 0.05 mmol catalyst, 4 mL of MeOH, and 6 mL of H ₂ O, at RT for 1.5-4hrs.	NH ₃ BH ₃	<i>Chem. Commun.</i> , 2016 , 52, 7719 – 7722
15	CoOx@NCNTs hybrids	Co	1 mmol nitroarene, 4.0 mol % Co catalyst, 3 MPa H ₂ , and 5 mL of EtOH, at 110°C for 3-15hrs	3 MPa H ₂	<i>ACS Catal.</i> , 2015 , 5, 4783–4789
16	Co-SiCN nanocomposit	Co	0.5 mmol nitroarene, 35 mg (4.8 mol %) catalyst, 5 MPa H ₂ , and 2mL of EtOH, 0.5ml H ₂ O at 15hrs 110°C	5.0 MPa H ₂	<i>Angew.Chem.Int.E d.</i> 2016 , 55, 15175 –15179
17	PtIPr NPs Catalyst	Pt	0.74 mmol nitroarene, 0.2 mol % of Pt, 1bar H ₂ , and 5ml of THF solvent at 30°C .	1 bar of H ₂	<i>ChemCatChem.</i> , 2014 , 6, 87–90
18	Ni- xMoO ₃ /CN@S BA-15 catalysts	Ni-Mo	6mmol nitroarene, 20mg of Catalyst, 36 mmol N ₂ H ₄ ·H ₂ O, 6ml of Ethanol, at 40 °C, 30-60mn	N ₂ H ₄ ·H ₂ O	<i>Green Chem.</i> , 2017 , 19, 809 –815



Appendix 3.1. (A) SEM image of IISERP-COF5 (B) HR-TEM image of Co@IISERP-COF5. Below (A and B) SEM images of the unsupported Co nanoparticles at different magnifications



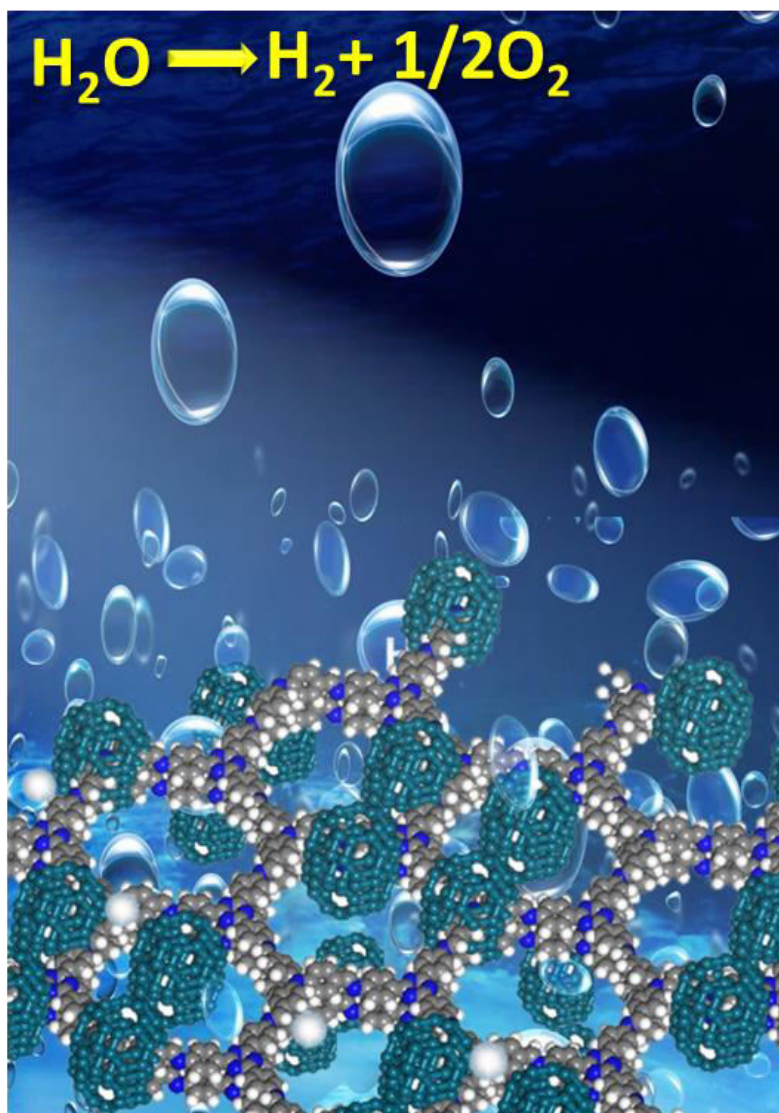
Appendix 3.2. HR-TEM of the Co@IISERP-COF5 shows the presence of small nanoparticles with different lattice facets. Note that these are the predominant lattice planes.



Appendix 3.3. HRTEM images of the unsupported Co/Co(OH)₂ nanoparticles. (A) The lattice fringes index well to the α -Cobalt metal (ICSD: 05-0727). (B) Few regions showed the presence of Co(OH)₂ crystallites. (C) The SAED pattern shows that the phase formed as a polycrystalline material. (D) and (E) Higher resolution images indicating the formation of the phase as aggregated thin flakes which are stacked. (F-I) Images from different regions of the sample and the lattice fringes on all these images uniformly index to 0.20 nm suggesting Cobalt metal as the majority species.

Chapter-4

Low-overpotential Electrocatalytic Water Splitting with Noble-Metal-Free Nanoparticles Supported in an sp^3 N-Rich Flexible COF



4.1. Introduction

Covalent Organic Frameworks (COFs) are a novel class of porous organic polymers that form pre-designable crystalline architectures that are unlike traditional polymers, which generally pack in a more randomized amorphous fashion¹. The majority of COFs are constructed from aromatic carbon rich building blocks that favor the formation planar 2D networks that can pi-stack to form framework with uniform 1-D pores. Owing to their chemical tunability, ordered porosities and crystalline nature COFs are being actively pursued for use in wide range of applications such as oxygen reduction reactions², photoconductivity³, proton conduction⁴, hydrogen generation⁵, quantum sieving⁶, sensing⁷, gas storage⁸ and catalysis⁹. Recently, COFs have been explored as supports for active metal nanoparticles (nps), which have resulted in composites with diverse properties¹⁰. Through appropriate choice of building units, one can potentially tune the nanoparticle binding and np-np separation in the host COFs.

In this Chapter, we describe a flexible pseudo three-dimensional COF which serves as ideal supports for nanoparticles of hydroxides of non-noble-metals. We demonstrate the electrocatalytic activity of these COF-np composites in Oxygen Evolution Reaction (OER) from water, $2\text{H}_2\text{O}(\text{l}) \rightarrow \text{O}_2(\text{g}) + 4 \text{H}^+(\text{aq}) + 4\text{e}^-$. The flexible sp^3 nitrogen-rich host COF (IISERP-COF2) limits the size and distribution of the nickel and cobalt hydroxide nanoparticles, $(\text{Co}_x(\text{OH})_2\text{Ni}_y(\text{OH})_2)$, to a regime (~ 2 nm) that is otherwise difficult to access and allows for near-record low overpotentials for electrocatalytic water splitting reaction. The composite $\text{Co}_x(\text{OH})_2\text{Ni}_y(\text{OH})_2@$ IISERP-COF2 is a highly active electrocatalyst for the oxygen evolution reaction and that has an overpotential of only 258 mV at 10 mA cm^{-2} current density and possesses outstanding kinetics (Tafel slope: 38.9 mV dec^{-1}). The overpotential observed in our $\text{Co}_x(\text{OH})_2\text{Ni}_y(\text{OH})_2@$ IISERP-COF2 system is the best in the class and is close to the current record of ~ 200 mV for any noble-metal-free (Fe-Co-Ni metal-oxide-film) electrocatalytic water splitting systems¹¹.

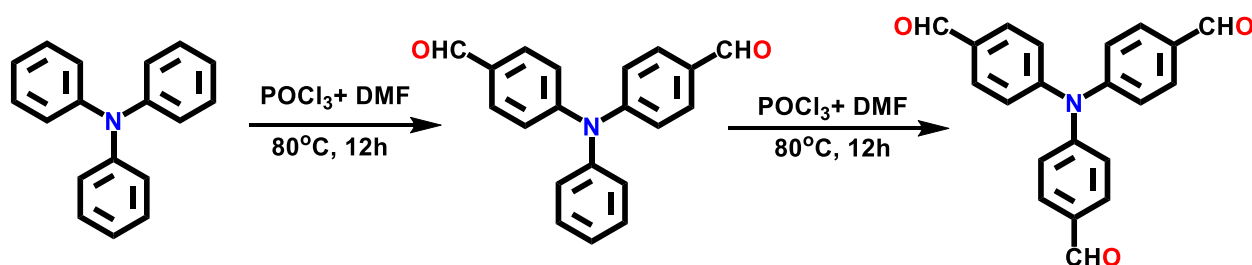
4.2. Experimental details

4.2.1. Materials and Measurements

Thermogravimetric analysis was carried out on a NETSZCH TGA-DSC system. The routine TGAs are done under N_2 gas flow (20ml/min) (purge + protective) and samples were

heated from RT to 900°C at 2K/min. Infrared spectra were recorded using Bruker FT-IR (ATR mode) spectrophotometer in the range of 4000-600 cm^{-1} . CD spectra is recorded on JASCO J-815 CD spectrometer. Raman spectra were recorded using LabRAM HR 800 Raman spectrometer (Horiba Scientific). NMR spectra are recorded on a 400 MHz Jeol ECS-400 and Bruker 500MHz. X-Ray photoelectron spectroscopic (XPS) measurements were carried out on a VG Micro Tech ESCA 3000 instrument at a pressure of $>1 \times 10^{-9}$ Torr (pass energy of 50 eV, electron take-off angle of 60°, and the overall resolution was 0.1 eV). Ultra Plus Field Emission Scanning Electron Microscope with integral charge compensator and embedded EsB and AsB detectors. Oxford X-max instruments 80mm². (Carl Zeiss NTS, Gmbh), Imagin conditions: 2kV, WD=2mm, 200kX, Inlens detector. Adsorption studied was done using a Quanta Chrome pore and surface area analyser, Model IQ dual port. FEI (Jeol FEG 2100F is the model) high-resolution transmission electron microscope (HRTEM) equipped with field emission source operating at 300 KeV was used. The electrochemical studies are carried out by using Bio-Logic instrument with techniques like cyclic voltammetry (CV), chronoamperometry and linear sweep voltammetry (LSV).

4.2.2. Synthesis of tris(4-formylphenyl)amine



The tris(4-formylphenyl)amine monomer was synthesized by a slight modification to a reported procedure¹². Phosphorus oxychloride (POCl₃) (9.5 mL, 101.9 mmol) was added dropwise to dry dimethylformamide (DMF) (7.3 mL, 94.3 mmol) at 0°C under argon/nitrogen atmosphere. The mixture was thawed and stirred at 0°C for 30 min and room temperature for about an hour. A solution of triphenylamine (5.0 g, 20.4 mmol) in dry chloroform (5 mL) was added to the above mixture slowly over a period of 30 min and resulting contents were stirred at 80°C for 12 hrs. After cooling to room temperature, the solution was poured into ice cold water (400 mL) and the resulting mixture was neutralized to pH 7 with 5% NaOH(aq) solution. After extraction with DCM, the organic layer was washed with brine solution and water at least three to four times to

remove excess mineral acids and DMF. The extracted organic layer was dried with Na_2SO_4 and the solvent was removed under reduced pressure gives a blackish yellow solid product. The residue was filtered through a short column chromatography with hexane/dichloromethane (1:2, v/v) to yield a yellowish solid product of mono and di-substituted aldehyde. This di-substituted aldehyde is subjected to the same reaction to get tri-substituted aldehyde. A DCM solution of above-obtained di-aldehyde is added into an ice-cooled mixture of POCl_3 (9.5 mL, 101.9 mmol) and dry DMF (7.3 mL, 94.3 mmol) under a nitrogen atmosphere. The resulting mixture was heated at 80°C for 12hrs then cool down to room temperature and poured into ice water (400 mL). The resulting mixture was neutralized to pH 7 with 5% aqueous NaOH solution, which was then extracted with DCM. Once again, the organic layer was washed with brine solution and copious amount of water then dried over Na_2SO_4 . Following the evaporation of the DCM under reduced pressure produces the blackish yellow compound. The solid was purified with column chromatography using hexane/dichloromethane (1:4, v/v) gives the product as yellow color crystals in considerable yields (2.7 g, 40%). ^1H NMR (400 MHz, CDCl_3): δ = 9.96 (s, 3H), 7.86 (d, J = 8.7 Hz, 6H), 7.27 (d, J = 8.6 Hz, 6H). ^{13}C NMR (101 MHz, CDCl_3): δ = 190.83 (s), 151.64 (s), 133.08 (s), 131.91 (s), 124.98 (s).

p-phenylenediamine(2) and all other chemicals were purchased from the Sigma Aldrich used without any other purification.

4.2.3. Synthesis of IISERP-COF2 α and IISERP-COF2 β

Tris(4-formylphenyl)amine (1) (40 mg, 0.12mmol) and 1,4-diaminobenzene (2) (20 mg, 0.19mmol) were weighed into a Pyrex tube and dissolved in a 3.0 mL of ethanol, to this *o*-dichlorobenzene (*o*-DBC) (3.0mL) was added and stirred until monomers dissolve. Then 0.25 mL of 3M aqueous acetic acid (CH_3COOH) was added and Pyrex tube was flash frozen in a liquid nitrogen bath, the sealed tube was placed in an oven at 120°C for 3 days (Figure 4.1). This produces 48 mg (86% isolated yield) of yellow colored solid product (IISERP-COF2 α .) upon washing with DMF, dioxane, MeOH, Acetone and THF. This obtained IISERP-COF2 α is activated (desolvated) by heating at above 50°C to prepare IISERP-COF2 β . Formula for the IISERP-COF2 β based on unit cell stoichiometry: $\text{C}_{240}\text{N}_{32}\text{H}_{168}$, M. Wt. 3500.2 g/mol, CHN observed. C = 77.35; H = 4.409; N = 10.85. Calculated 82.36; H = 4.84; N = 12.81%.

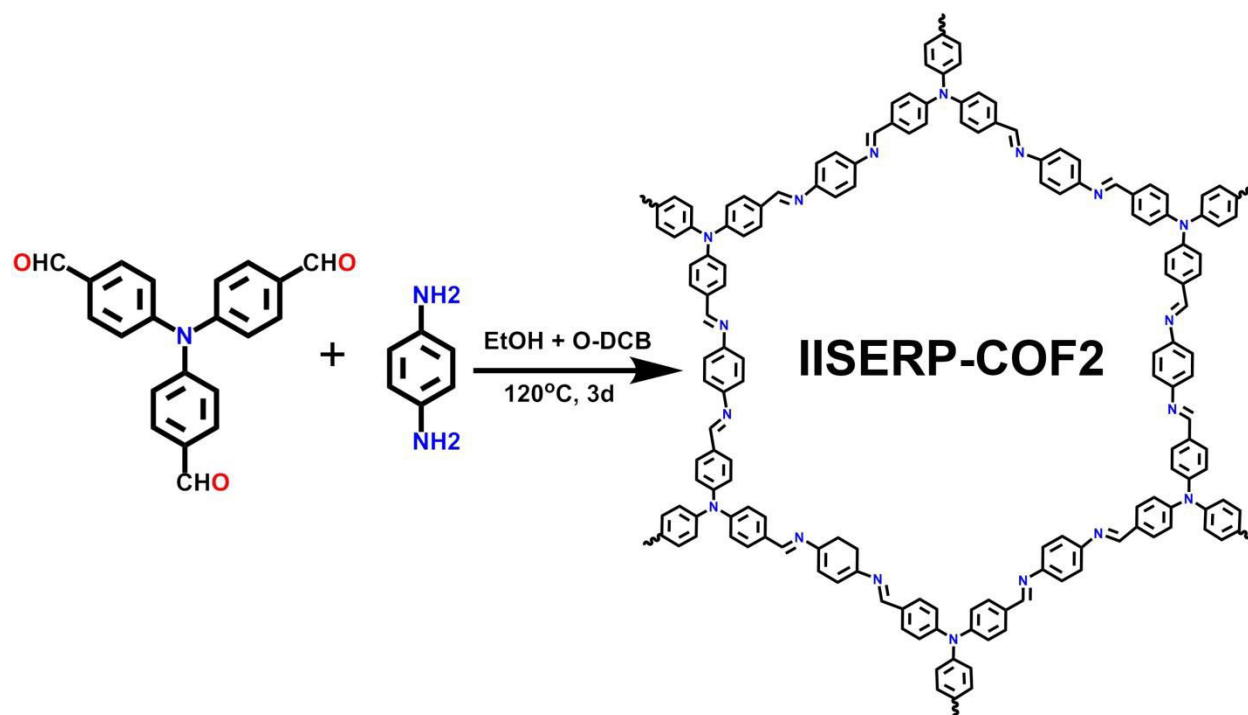


Figure 4.1. Schematic representation of the IISERP-COF2 synthesis and proposed topology structure.

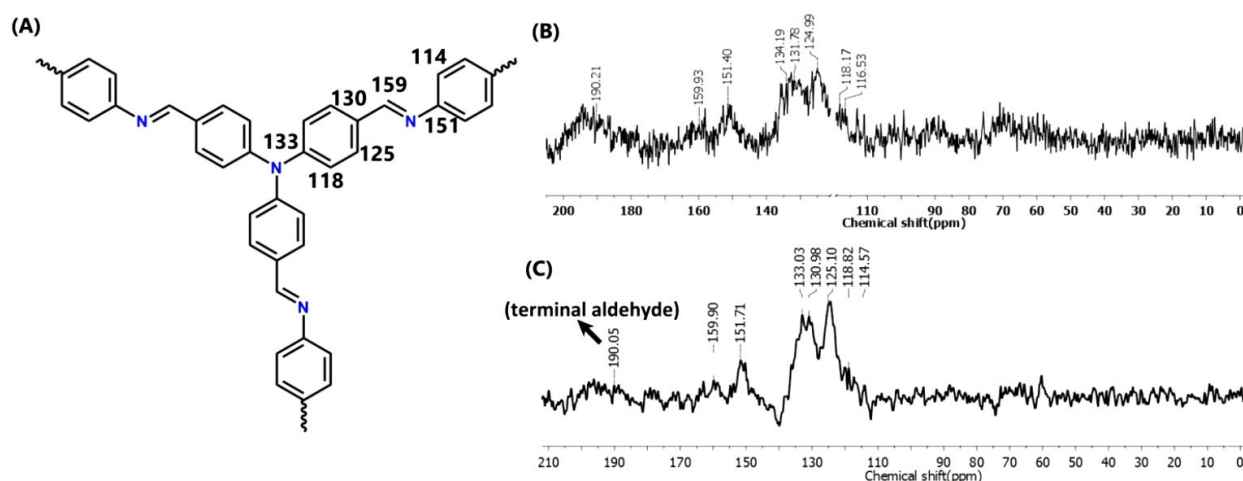


Figure 4.2. (A) A schematic representation of the different unique carbon atoms in the COF and their solid-state ^{13}C -MASNMR spectrum. (B) IISERP-COF2 α . (C) IISERP-COF2 β .

4.2.4. Synthesis of Homometallic $\text{Co}_x(\text{OH})_2/\text{Ni}_y(\text{OH})_2@$ IISERP-COF2 β Composites

The as-synthesized IISERP-COF2 β (100 mg) was dispersed in 20mL of n-hexane and sonicated for about 30 min until it became a homogeneous suspension. To this, 0.5 mL of methanolic solution of $\text{NiCl}_2 \cdot 6\text{H}_2\text{O}$ (1) or $\text{CoCl}_2 \cdot 6\text{H}_2\text{O}$ (2) (40 mg in 0.5mL of MeOH) was

added drop by drop over a period of 3hrs under vigorous stirring. Upon addition of the methanolic metal salt, the solution turns from yellow color to a deep orange-red color (Figure 4.3). Stirring was continued for another 12hrs at room temperature, then solid particles Co/Ni@IISERP-COF2 were extracted by filtering the solvent and dried at 150⁰C for 12hrs. Then the deep-orange solid of metal loaded COF was suspended in 50mL of distilled water and the reduction was carried out by using 25 mL 0.6 M aqueous NaBH₄ solution. This result in the formation of the IISERP-COF2 supported metal nanoparticles loaded catalysts as a dark greenish color solid product (Figure 4.4). Both the Ni@COF2 [1] and Co@COF2 [2] composites exhibit about ~15-16% of Ni/Co nanoparticles loading (ICP analysis). From the CHN analysis the observed: C = 61.60; H = 4.35; N = 9.13; Calculated: % C = 62.49; H = 4.20; N = 9.72 for the Ni loading sample. Similarly for Co loaded COF2 Observed: C = 62.32; H = 4.45; N = 9.24; calculated: C = 62.45; H = 4.19; N = 9.71.

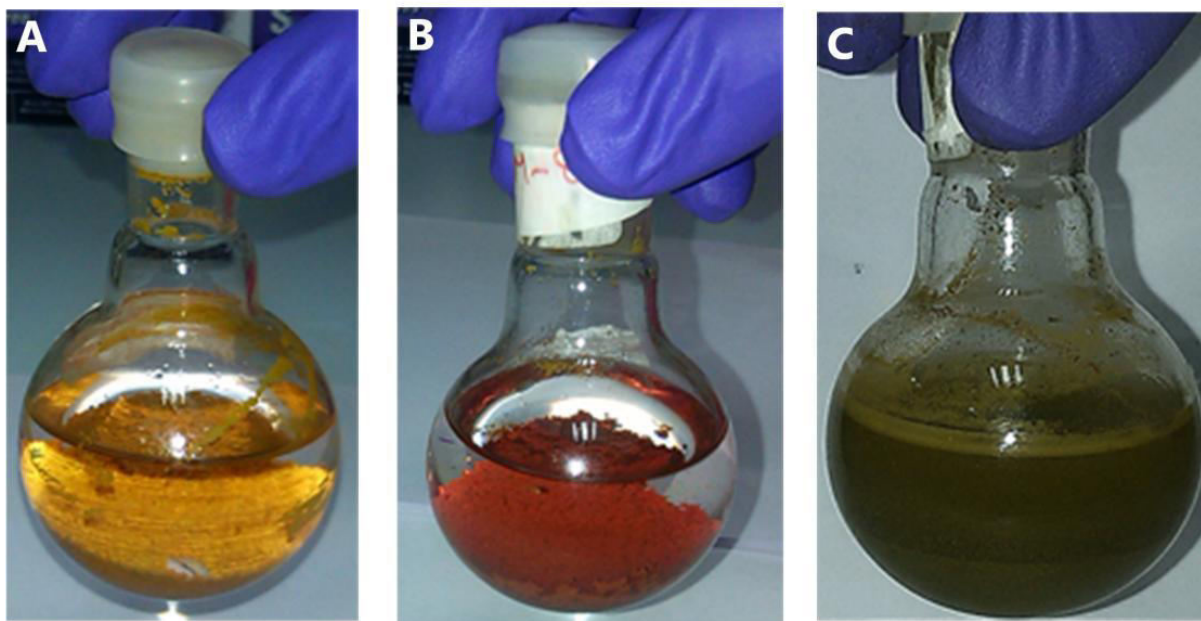


Figure 4.3. Photographic images showing the change of colors upon addition of metal salts and the reducing agent. (A) As-synthesized COF before addition of metal salt (B) After the addition of metal salt (C) After the reduction using NaBH₄. Similar color change trend was observed for the heterometallic composites.

4.2.5. Synthesis of Heterometallic Co_x(OH)₂/Ni_y(OH)₂@COF2-β Composite

In a typical synthesis, the as-made IISERP-COF2-β (100 mg) was dispersed in 20mL of n-hexane and sonicated for about 30 min until it became homogeneous suspension. To this, a

mixture of 0.5 mL methanolic solution of $\text{CoCl}_2 \cdot 6\text{H}_2\text{O}$ + $\text{NiCl}_2 \cdot 6\text{H}_2\text{O}$ ((3)20 +20 mg, 30+10 (4),10+30 (5) in 0.5mL of MeOH) was added drop by drop over a period of 3hrs with vigorous stirring. Upon addition of the methanolic metal salt, the solution turns from yellow color into a deep orange-red color (Figure 4.3). Stirring was continued for additional 12hrs at room temperature, then the solid particles (Co/Ni@COF_2) were extracted by vacuum filtration and dried at 150°C for 12hrs. This deep-orange solid of metal loaded COF2 was suspended in 50mL of distilled water and the reduction was carried out by using 25 mL 0.6 M aqueous NaBH_4 solution. This result in the formation of the IISERP-COF2 supported nickel and cobalt nanoparticles loaded nanocatalysts (Ni@IISERP-COF_2 [1], Co@IISERP-COF_2 [2], $8\text{Co}:8\text{Ni@IISERP-COF}_2$ [3], $12\text{Co}:4\text{Ni@IISERP-COF}_2$ [4], and $4\text{Co}:12\text{Ni@IISERP-COF}_2$ [5]) as a dark greenish color solid product. All the $\text{Co/Ni@IISERP-COF}_2$ composites exhibit about ~15-16% of Ni/Co nanoparticles loading (ICP analysis). Here the numbers in the compositions represent the weight % of metal/metal hydroxide nanoparticles present in the COFs, which was conformed from the ICP analysis.

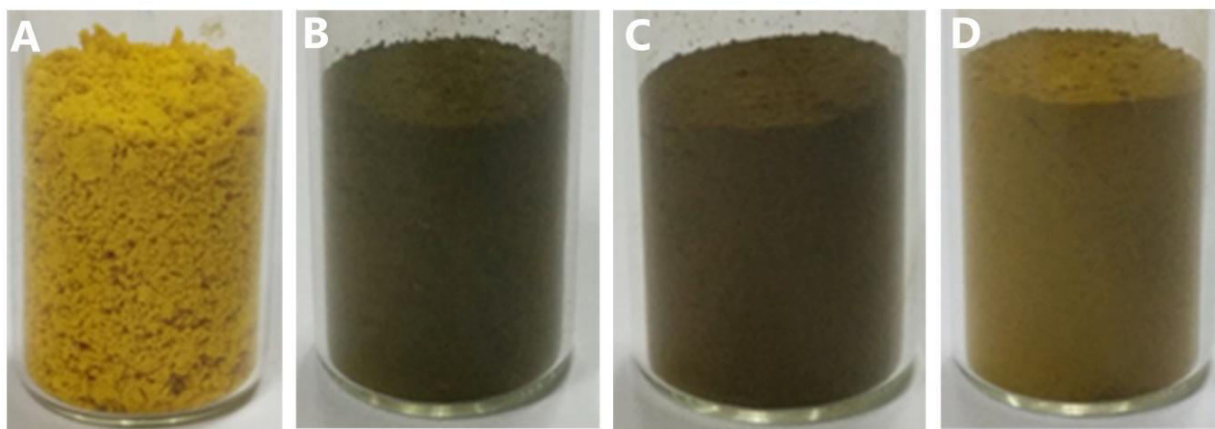


Figure 4.4. Photographic images showing the color changes upon addition of metal nanoparticles to the IISERP-COF2 β . A) As-synthesized COF; B) Nickel loaded COF (Ni@COF_2); C) Co+Ni loaded COF (Co.Ni@COF_2); D) Cobalt loaded COF (Co@COF_2). Note that these are samples collected by mixing several synthesis batches and do not represent the yield from a single 100mg synthesis.

To grasp the effect Co/Ni ratio in the electrocatalyst, we further screened different (Co:Ni) ratios by fixing the total metal concentration constant (40mg). In the homometallic case (Co@IISERP-COF_2 (2) or Ni@IISERP-COF_2 (1), 100 mg IISERP-COF2 and 40mg of the metal salts ($\text{CoCl}_2 \cdot 6\text{H}_2\text{O}$ or $\text{NiCl}_2 \cdot 6\text{H}_2\text{O}$) were used. For making the heterometallic phases, the

IISERP-COF2 weight was maintained constant (100mg) and the following variations were made to the Co:Ni ratio: 20mg Co:20mg Ni [3], 30mg Co:10mg Ni[4], 10mg Co:30mg Ni[5]. All these cases offered a metal loading of ~16-18wt%. The CHN analysis values for the 20mg Co:20mg Ni loading were CHN % observed. C = 60.73; H = 4.45; N = 8.92. Calculated: C = 62.47; H = 4.19; N = 9.71.

4.2.6. Electrochemical Studies

The test cell is fabricated in a traditional three-electrode configuration by using Hg/HgO as the reference electrode and platinum flag as a counter electrode. The modified glassy carbon electrode was used as a working electrode (area = 0.07065 cm²). The working electrode was prepared by coating the catalyst (**1-5**) on carbon disk and the catalyst mass loading was maintained constant (20 µg) for all the electrochemical studies. The catalyst ink was prepared by sonicating the mixture of 1 ml ethanol:water (3 : 2) and 5mg of Co_xNi_y@IISERP-COF2β, this catalyst paste was drop-coated on the tip of a glassy carbon disk electrode (Area : 0.07065 cm²). Resulting electrode was dried under IR lamp and used as the working electrode for the electrochemical studies. Prior to catalytic studies the tip electrode was polished with 0.3 µm alumina slurry and washed with acetone and deionized water. For electrochemical studies, the de-aerated 0.1 M KOH was used as an electrolyte. The potential is converted to a reversible hydrogen electrode (RHE) by using the following equation. (From now on η₁₀ represents overpotential at 10 mA cm⁻² current density)

$$E_{\text{RHE}} = E_{\text{Hg/HgO}} + 0.098 + 0.0591 * \text{pH}$$

Faradaic Efficiency

The Faradaic efficiency experiments were carried out using a rotating ring disc electrode (RRDE) experiment by applying the series of current density steps from 2 to 10 mA cm⁻² to the disk and measured the corresponding voltage (V). The same as the above procedure is adopted for the catalyst preparation, loading, and cleaning of RRDE electrode [Pt ring (9 mm outer diameter and 7.5 mm inner diameter) GC 19 disk (6 mm diameter) and (area of GC disk = 0.2628 cm²)]

The efficiency was calculated by using the following equation

$$\text{Faradaic Efficiency} = (n * I_r) / (I_d * N)$$

Here, n = number of electrons involved during the process

I_r and I_D = Ring and disk current respectively.

N is the collection efficiency of ring electrode (0.37)

Electrochemical surface area

Electrochemical active surface area (ECSA) has been calculated by recording the cyclic voltammetry (CV) in the non-faradaic region at different scan rate¹³. The electrochemical double layer capacitance (C_{dl}) of the catalytically active surface was estimated from the anodic current density vs scan rate graph slope¹³. The C_{dl} is calculated by using Equation 1.

$$i = \nu C_{dl} \dots\dots\dots\text{Equation 1}$$

Here ‘ i ’ is the measured anodic current density and ‘ ν ’ is the scan rate. The plot of i vs ν offers the C_{dl} slope as a straight line¹³. The ECSA is calculated by dividing the C_{dl} with specific capacitance, using a capacitance (C_s) value of $27 \mu\text{F}/\text{cm}^2$. In addition, the roughness factor (RF) is calculated by dividing the ECSA by surface area of the electrode (0.07065 cm^2).

TOF calculation

The turnover frequency (TOF) values of $\text{Co}_x(\text{OH})_2/\text{Ni}_y(\text{OH})_2@\text{IISERP-COF2-}\beta$ (1-5) samples coated on the GC electrodes were calculated from the equation-2¹⁴

$$\text{TOF} = (j * A) / 4 * m * F \dots\dots\dots\text{Equation 2}$$

Here, j is the current density obtained at an overpotential of $400\text{mV} = 0.04237 \text{ A}/\text{cm}^2$; A is Surface area of the GC electrode = 0.07065 cm^2 and m is number of moles of active Ni/Co deposited on the working electrode = 0.13626E^{-6} ; F is Faraday efficiency = $96485 \text{ C}/\text{mol}$

Observed TOF at an overpotential of $400\text{mV} = 0.05691$.

4.3. Structure Solution and Description

The sp^3 nitrogen nodes in the COF impart significant flexibility to the structure. A 2D structure with hexagonal layers (SEM and TEM) that is consistent with the experimentally observed powder pattern has been obtained using a combination of the general-structure analysis system (GSAS) and modeling-based calculations carried out using the *Material Studio* program.

For the structure solution, we adopted the same routine as in our earlier work^{10d}. The X-Cell indexing followed by *Pawley* search revealed five space groups as most probable solutions: Ia-3, I2₁3, P6₃, and P4/n. The circular dichroism (CD) spectra of the COF confirmed its homochirality (Appendix 1), restricting the structure into chiral space groups. The final structure depicted in Figure 4.6. was solved in P6₃ and was geometry optimized and energy minimized using tight-binding density functional theory (DFT-TB).

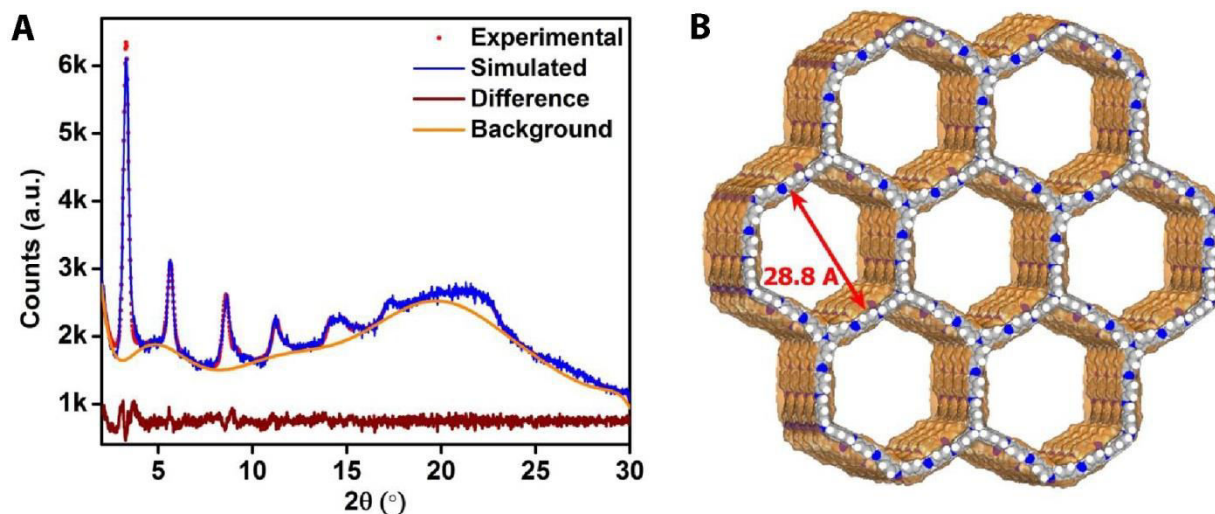


Figure 4.5. (A) Pawley fit for the IISERP-COF2 α for the structure solved in P6₃ setting. $a = b = 31.71(3)$; $c = 10.25(1)$, $R_p = 2.24$, $wR_p = 2.96$. (B) Structure of the IISERP-COF2- α showing the hexagonal honeycomb-shaped structure formed by stacked layers.

The powder patterns were analyzed in the P6₃ setting using both *Pawley* and *Le Bail* fits (Appendix 1). An excellent intensity agreement and fit was obtained for a Pawley fit in P6₃ space group. The unit cell for **IISERP-COF2 α** : $a = b = 31.71(3)$; $c = 10.25(1)$ Å (Figure 4.5); **IISERP-COF2 β** : $a = b = 29.43(3)$; $c = 28.48(4)$ Å in the same space group (Figure 4.6). Where is the eclipsed planar structure vs. buckled structure discussed? What about the pore size matching only for the buckled structure? Where is the DFTB minimization? The hexagonal layers of the **IISERP-COF2 β** had an *ABAB*... stacking arrangement with uniform triangular-shaped cavities (~ 18.5 Å) along the *ab*-plane (Figure 4.6). This pore size well agrees with the pore size observed from N₂ adsorption studies (vide infra). These layers are held together by six-point CH... π type interactions (2.835 Å) and their buckling results in the formation of uniform cavities (~ 22 Å) along the interlayer spaces (Figure 4.6. C and D).

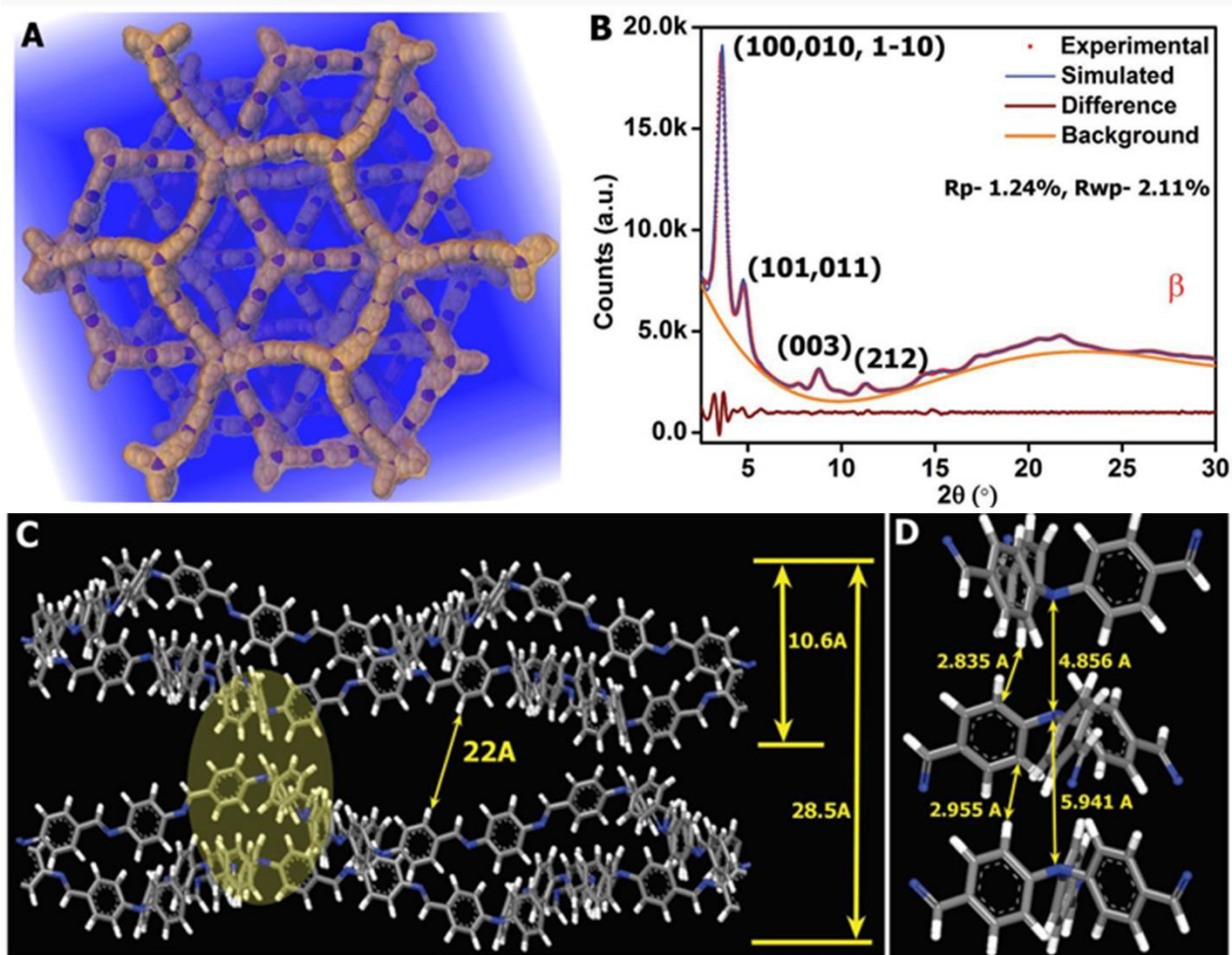


Figure 4.6. (A) Connolly representation of the structure of IISERP-COF2 β showing the presence of uniform triangular channels formed from with *ABAB...* stacking. This arrangement provides a pseudo-three dimensionality to the structure. (B) The Pawley fit for the IISERP-COF2 β . (C) Stacking of the pucker layers resulting in 22 Å cavities. The region highlighted in yellow is expanded in (D).

4.4. Results and Discussion

IISERP-COF2 was prepared by reacting tris(4-formylphenyl)-amine (1) and 1,4-diaminobenzene (2) in a mixture of ethanol and O-DBC at 120°C (Figure 4.1). The as-synthesized solvated form of COF is titled the α -phase (IISERP-COF2 α) that transforms irreversibly to a different structure upon activation/ desolvation is titled as β -phase (IISERP-COF2 β). The irreversibility of the α to β phase transformation was confirmed by PXRD and variable temperature VT-PXRD (Figure 4.7). Further thermogravimetric analysis (TGA) analysis shows IISERP-COF2 β remains thermally stable up to ~380°C, while in IISERP-COF2 α phase ~7 (wt%) of weight loss was observed at < 50°C indicating considerable amount of low-

boiling solvents (trapped during the COF wash) molecules were present in the pores, thus upon leaving the solvent the COF changes its framework structure (Figure 4.5, 4.6). All the adsorption measurements, microscopy studies (SEM and TEM), stability studies, the metal nanoparticle (Co/Ni) loading and electrochemical studies (OER) were carried out on the stable IISERP-COF2 β . Solid-state ^{13}C -NMR (500 MHz) spectra of both COFs displays eight different peaks

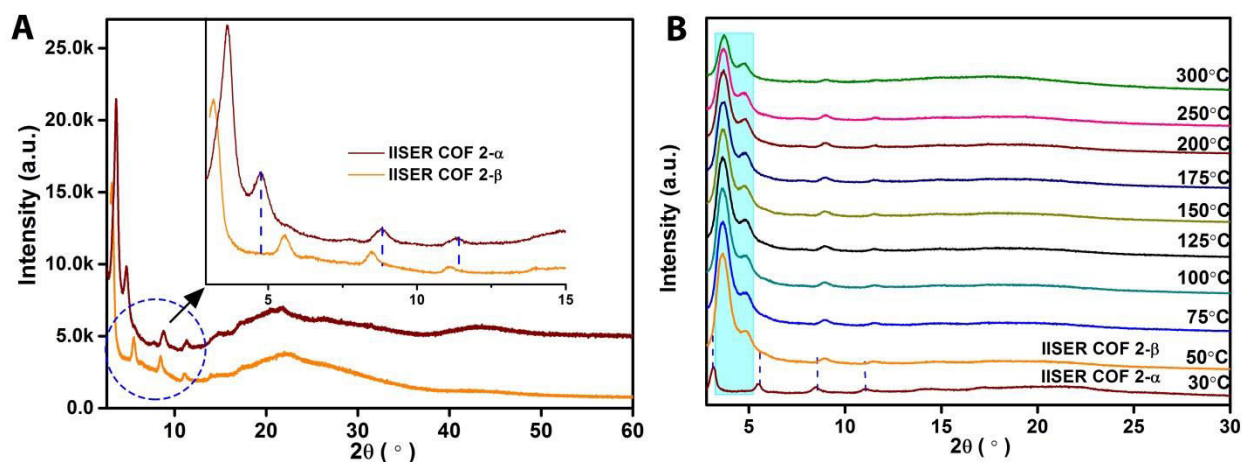


Figure 4.7. (A) Comparison of the powder X-ray diffraction patterns of the as-synthesized solvated phase, IISERP-COF2- α and the desolvated phase, (B) variable temperature PXRD analysis showing the transformation of α -phase to β -phase upon heating from 30 $^\circ\text{C}$ to 50 $^\circ\text{C}$. The dotted lines indicate the shrinking of the a-axis and expansion of the c-axis during this irreversible phase transformation.

between δ of 116 to 190 ppm and the signal observed at ~ 160 ppm indicates the formation of the imine (C=N) bond which propagates to form the IISERP-COF2 (Figure 4.2). while in IR spectroscopy the characteristic stretching bands observed at $\sim 1619\text{cm}^{-1}$ (C=N Schiff), $\sim 1167\text{cm}^{-1}$ (C-N sp 3 nitrogen) and $\sim 2800\text{cm}^{-1}$ (C-H, CHO unreacted terminal aldehyde) (Figure 4.8B). Both the ^{13}C -solid-state-NMR and IR spectra indicating IISERP-COF2 had an unreacted terminal aldehyde groups present.

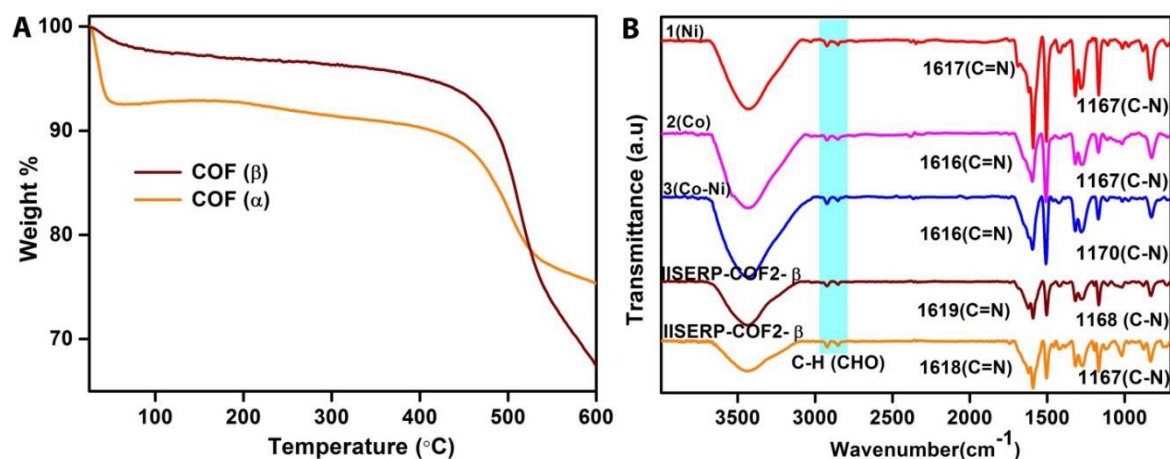


Figure 4.8. (A) TGA analysis of as-synthesized (α -phase) and desolvated (β -Phase) of IISERP-COF2. the initial weight loss in COF2- α is due to low boiling solvent and this is what appears to trigger the phase change to COF2- β . (B) IR spectra of as-made COFs (α and β -phase) and metal loaded COFs (1-3).

Both the FE-SEM and HR-TEM images of the IISERP-COF2 β displayed 2D hexagonal flakes morphology and these flakes are aggregate/stack into spherical bulky spheres (Figure 4.9). This hexagonal morphology is good in agreement with the theoretically modeled hexagonal structure (hexagonal $P6_3$ space group, Figure 4.5 and 4.6). A closer look under the HR-TEM of IISERP-COF2 β shows the stacking of these flakes extremely thin layers resembling layers of graphene (Appendix 4.2). The size of each hexagonal sheet is 400-500 nm in size with 20 nm edge, the darker regions at the edges indicating these thin layers that wrap inward. A 77K

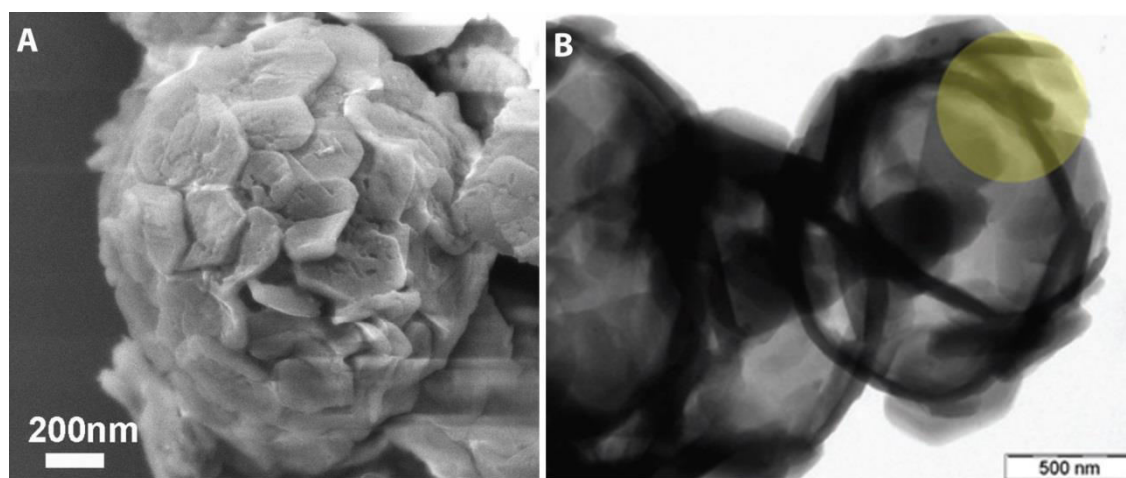


Figure 4.9. (A) A FE-SEM images of the IISERP-COF2 β grown as thin hexagonal flakes. (B) A TEM image showing the 2D-hexagonal sheets (\sim 500 nm), which are self-assembled into a sphere.

nitrogen adsorption isotherm of IISERP-COF2 β is shown in Figure 4.10 displays Type-1 microporous reversible isotherm. The Brunauer-Emmett-Teller (BET) surface area is found to be 557 m²/g and Langmuir surface areas found to be 866 m²/g. A DFT model fit to the N₂ isotherm (77K) yielded 19 and 21 Å bimodal pore are present in the IISERP-COF2 β (Figure 4.10).

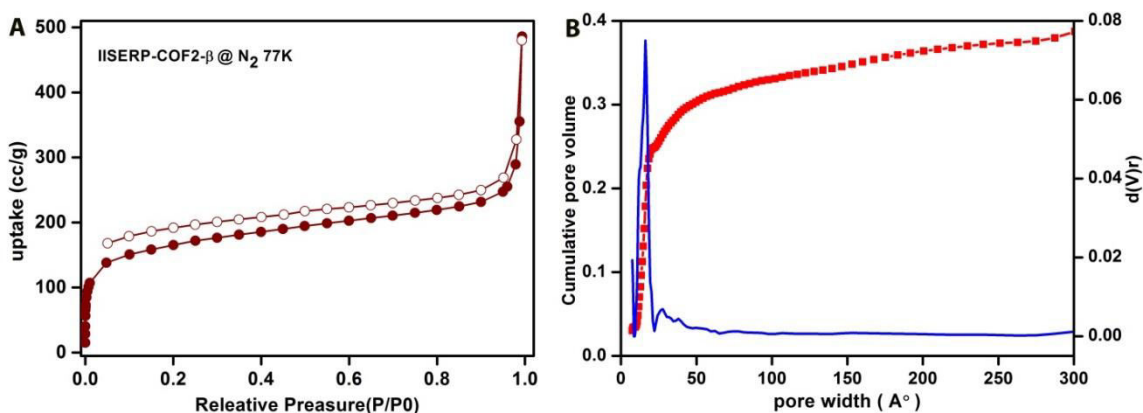


Figure 4.10. (A) A 77 K nitrogen adsorption isotherm of IISERP-COF2- β . (B) A DFT pore size distribution plot.

IISERP-COF2- β Nanocomposite (1-5)

The composite Co/Ni@IISERP-COF2 β electrocatalyst was made by growing the Co(OH)₂ and/or Ni(OH)₂ nanoparticles within the COF support via double solvent method (experimental section). Same technique was used for various ratios of Ni to Co nanoparticles synthesis: 16Ni@IISERP-COF2 [1], 16Co@IISERP-COF2 [2], 8Co:8Ni@IISERP-COF2 [3], 12Co:4Ni@IISERP-COF2 [4], and 4Co:12Ni@IISERP-COF2 [5], here the numbers in the compositions represent the weight % of metal/metal hydroxide nanoparticles present in the COFs, which was conformed from the ICP analysis. The PXRD of the Co/Ni nps loaded COFs showed no significant change of parent crystallinity (Figure 4.11) and few characteristic broad peaks were observed at higher angles corresponding to the cobalt and/or nickel (metals/metal hydroxides) (Figure 4.11). N₂ adsorption isotherms of the nanoparticles loaded COFs (1-5) shows > 70% reduction in the porosity and pore sizes were reduced to ~7Å from ~19Å (Figure 4.12 and Appendix 4.3). The BET surface areas fall in the range of ~25 m²/g from 557 m²/g and Langmuir surface areas in the range of ~100 m²/g from 866 m²/g. This huge drop in porosity and surface area indicate that majority

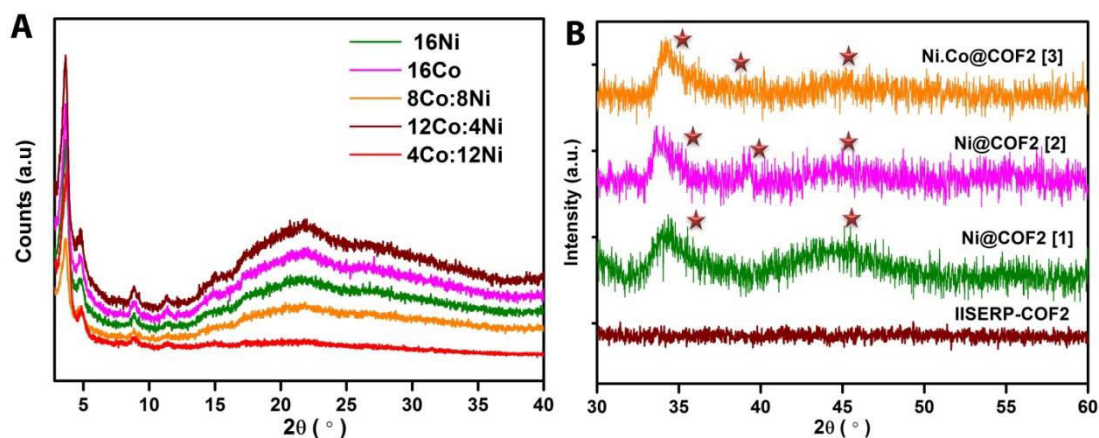


Figure 4.11. (A) PXRD of the metal loaded COFs (**1-5**). (B) Comparisons of as made and metal loaded (**1-3**) PXRDs at higher angles reflections. The broad peaks suggesting Co/Ni nanoparticles are small in size.

of the Co/Co(OH)₂ or Ni/Ni(OH)₂ nanoparticles are loaded in the COF pores. TGA measurement of nps loaded COFs (**1-5**) shows no considerable change in profile and displays thermal stability up to 400°C. (Figure 4.12B). Both in as-synthesized IISERP-COF2 β and its metal loaded composites **1-5**, the infrared spectra (IR) showed the presence of characteristic C=N bands and C-N bands. Their comparisons display no change in IR spectrum suggesting that the reduction procedure (double solvent method) is effective in selectively reducing the Co/Ni salts without affecting the COF's structure (Figure 4.8B).

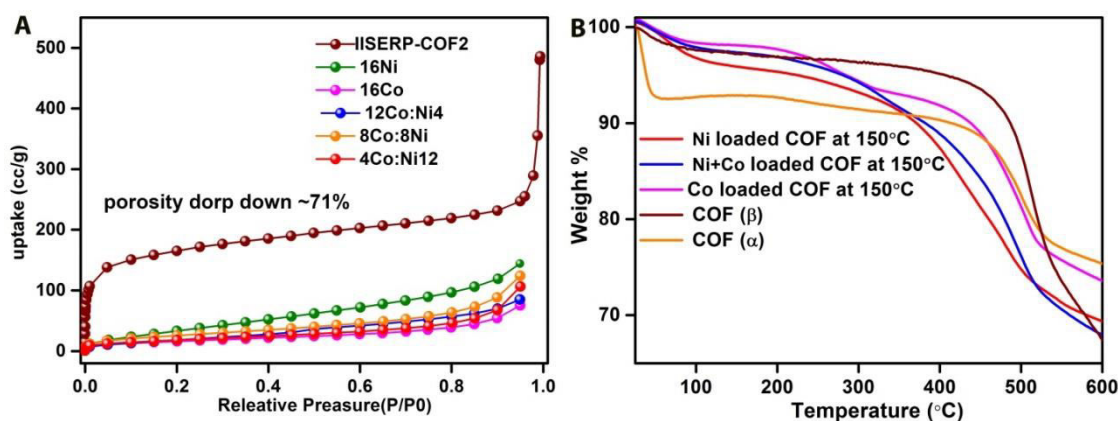


Figure 4.12. (A). Comparison of the N₂ isotherms of the IISERP-COF2 β and Co/Ni nanoparticles loaded IISERP-COF2 β (**1-5**) (B) TGA analysis of as-synthesized and Co/Ni nps loaded IISERP-COF2 β (**1-5**).

The FE-SEM of the Ni loaded IISERP-COF2 (**1**) shows no considerable change in pristine hexagonal morphology except very few additional bright spots /particles corresponding

to the Ni and/or Ni(OH)₂ nanoparticles (Figure 4.13A). Unlike our previous studies Pd@IISERP-COF1 (chapter 2), here the Ni nps do not lie on the surface and the same was observed in all the samples (1-5). The HR-TEM images of the Co+Ni (~4wt%+~12wt %)@COF (5) sample clearly shows the growth of metal hydroxide or metal on the surface of the COF and these metal nanocrystallites are uniformly distributed (Figure 4.13C and D). Further figure 4.13D shows these Ni nps are well blending (wrinkles) with the COF in extremely nano size, this could be emerging from the flexible nature of sp³ nitrogen-rich centers. A SAED pattern of the COF (5) shows the polycrystalline character and SEM-EDX elemental analysis displays these nanoparticles were homogeneously distributed all over the COFs (Figure 4.13E). The particle size distribution calculated from the HR-TEM images reveals that the majority of the nanoparticle are <2 nm in size and some (less than 5%) are >4 nm in size (Figure 4.13F).

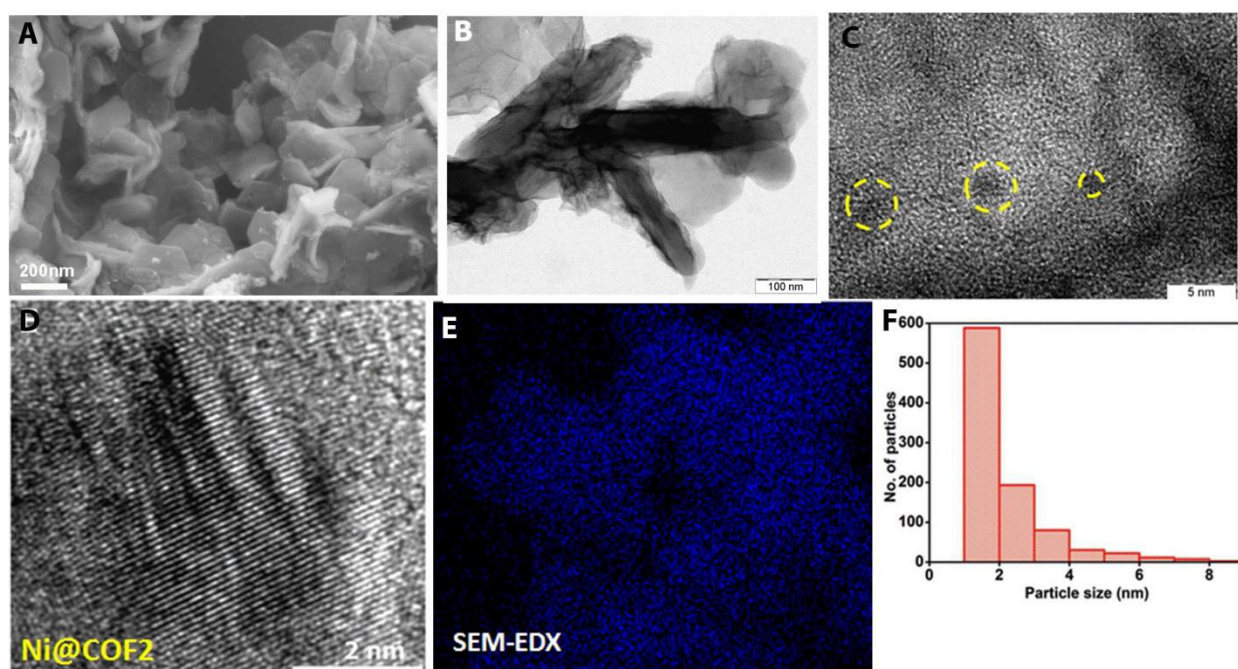


Figure 4.13. (A) FE-SEM image of Ni@IISERP-COF2 β (1) showing the hexagonal platy morphology. (B) HR-TEM image showing the Ni@IISERP-COF2 β appearing like thin nano-cloth morphology. (C) A magnified image of the nps loaded IISERP-COF2 displays the growth of metal nanoparticles (< 2-3nm). (D) The Ni nanocrystallites ($d = 0.21$ nm) growing along the wrinkles on the COF nanocloth. (E) SEM-EDX elemental mapping shown nps are homogeneously distributed across the sample. (F) Particle size distribution curve calculated from HR-TEM image of Appendix 4.4

The loading of the metal nanoparticles using the aqueous phase reduction is expected to result in the formation of metal oxide or hydroxide or neutral metal or oxy-hydroxide nanoparticles. However, from the PXRD analysis no unique signals were observed for metal oxide or hydroxide nanoparticles, except a broad peak at $2\theta = 44^\circ$ assigned to be (111) plane of the Ni metal. Further, substantial broad peaks at a higher angle indicating the nanocrystallites were very small in size (**1-3**). While in the X-ray photoelectron spectroscopy (XPS) analyses reveal the binding energies (B.E) corresponding to $2p_{5/2}$, $2p_{3/2}$ levels of β -Ni(OH)₂ and β -Co(OH)₂ (Figure 4.14D and E) and no peaks are observed corresponding to the metal oxide or neutral metal nanoparticles. These results are corroborating with lattice fringes obtained in the HR-TEM analysis (Ni(OH)₂ d-spacing of 0.24 nm (100) plane) and most of the TEM lattice fringes clearly displays the (100), (110), and (001) planes of the Ni(OH)₂ nanoparticles. Further, Cyclic Voltammograms (CV) of (**1-5**) showed the M^{2+}/M^{3+} redox couple of metal hydroxides and supporting both the TEM and XPS analysis results (Figure 4.13). Therefore all these techniques suggest that majority of the nanoparticles are hydroxides and few neutral metal nps also could be presented but their relative amounts could not be quantified. To get more

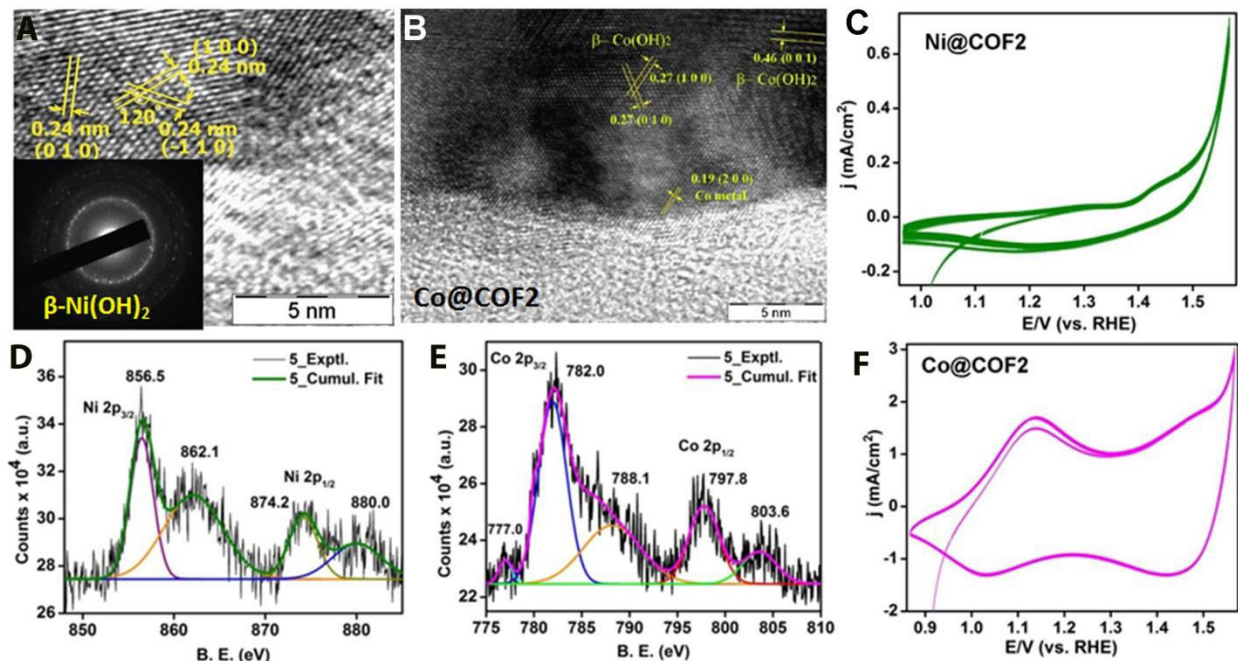


Figure 4.14. (A-B) Lattice fringes have been indexed with d-spacing of 0.24nm and assigned to be Ni(OH)₂. inset: SAED pattern displays polycrystallinity of β -Ni(OH)₂ nanoparticles. (D-E) XPS spectra of 4Co:12Ni-COF (**5**). The B.E. found to be β -Ni(OH)₂ and β -Co(OH)₂ (F) Cyclic Voltammograms (CV) of Co@IISERP-COF2 β and its redox couple (M^{2+}/M^{3+}).

understanding of metal–COF interactions we carried out an experiment under HR-TEM beam. When the electron beam was focused on the particular region it volatilized the top layers of M@COF in about 15 mins, underneath the volatilized layers, the presence of well-distributed metal nanoparticles (Appendix 4.5) could be observed. This result further supports the residence of the nps inside the pores.

4.5. Electrochemical Studies

For the electrochemical studies, a traditional three-electrode test cell with a Hg/HgO reference electrode and a platinum flag (Pt flag) counter electrode was used. The catalyst (**1-5**) coated glassy carbon electrode dried under an IR-lamp was used as the working electrode. The catalyst mass loading was maintained to be 20 μg for all the electrochemical studies. In all the cases, deaerated 0.1 M KOH solution was used as the electrolyte. Linear sweep voltammograms (LSVs) of **1-5** were investigated to examine the anodic reaction by scanning in a potential window of 1.1–1.7 V (vs (RHE)) at 1600 rotation per minute (rpm) of the working electrode. The peak at ~ 1.30 V, before the onset of OER, corresponding to the formation of Ni(III) or Ni(IV) species, is characteristics of the active nickel site¹⁵. This step is followed by a sharp increase in current due to the oxygen evolution (Figure 4.15A). The composites **1-5** have all shown the characteristic property of oxygen evolution (OER) at higher potential >1.41 V (vs RHE). Among them all (**1-5**), the **5** has the best OER characteristics with the lowest onset (1.430 V) and overpotential (258.0 mV at 10 mA/cm²) (figure 4.15A).

These onset potential and overpotential are considerably less compared to the best reported heterometallic Ni–Co-based electrocatalysts (Table S1,). The calculated overpotential for all the catalysts (**1-5**) follow the order of **5** (258.0 mV at 10 mA/cm²) < **3** (315.8 mV at 10 mA/cm²) < **4** (399.8 mV at 10 mA/cm²) < **1** (402.3 mV at 10 mA/cm²) < **2** (487.3 mV at 10 mA/cm²). As another important consideration, we observed that although the gas evolution at the catalyst-coated electrode during the electrolysis is very vigorous, gas bubbles dissipate rapidly into the solution with no bubble accumulation observed on the electrode surface. The kinetics associated with the mass transfer at the electrode-electrolyte contacts were examined using a Tafel plot (with 75% IR-compensation). The Tafel slope from a log I vs potential had a low value of 38.9 mV dec⁻¹ for the catalyst **5**, whereas, the **4**, **3**, **2**, and **1** had values of 86.3, 64.1,

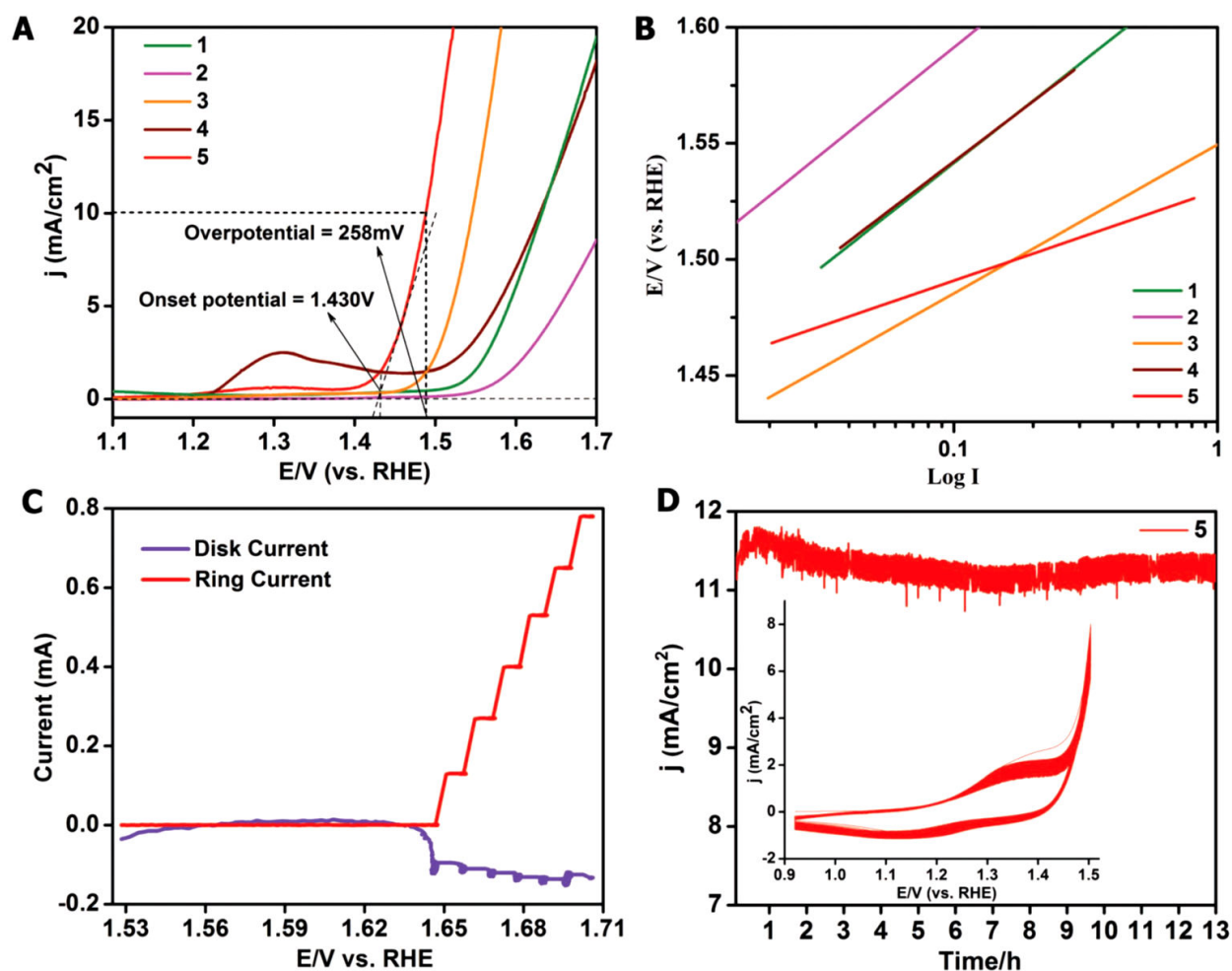


Figure 4.15. (A) LSV plots of all the metal loaded samples (**1-5**). (B) Comparison of the Tafel plots the composites (**1-5**) showing the most favorable charge transfer kinetics for the **5**. (C) Faradaic efficiency (0.9) measurements using RRDE experiment. (D) Chronoamperometry plot of **5** done at 1.5 V (vs RHE) showing the stability in the current outputs over 13 hrs. Inset CV shows the Ni(III)–Ni(IV) redox couple being stable over 500 CV cycles.

91.4, and 89.3 mV dec^{-1} , respectively. The Tafel slope of **5** is lower than any Co or Ni-based electrocatalyst reported in the literature (Table 4.1), although values lower than 38.9 mV dec^{-1} have been observed in Ni-Fe systems¹⁶. To evaluate the Faradaic efficiency of **1-5**, rotating ring-disk electrode (RRDE) experiment was carried out by applying the series of current density steps from 2 to 10 mA cm^{-2} (Figure 5C), Faradaic efficiency was calculated to be 0.9 (for the catalyst **5**) (Figure 4.15). The electrochemical activity of, **5**, was further investigated by determining its electrochemical surface area and roughness factor (RF). Accordingly, **5** has a double layer

capacitance of $3.98 \times 10^{-4} \text{ F cm}^{-2}$ and its electrocatalytic surface area was estimated to be 4.7 cm^2 .¹³ While the RF, representative of micro and macroscopic roughness, is found to be 66.

An important factor that quantifies the oxygen evolution (OER) is the turn over frequency (TOF), which for **5**, was estimated to be 0.186170 s^{-1} at an overpotential of 408 mV (assuming that all the metal sites are involved in OER), which is six-fold higher than that obtained with Ir/C [0.027 s^{-1}]¹⁷, and is comparable to some of the highest reported TOF (e.g., 0.21 s^{-1} for Ni-Fe and NiO nanostructures)¹⁸. Such high TOF have typically been associated with nanoparticles with sizes of 2-3 nm^{15, 17}. The chronoamperometry measurements on catalyst **5** indicated the stable current that could be generated over 13hrs (Figure 4.15D and Appendix 4.6). Further, the cyclic stability was confirmed by potential scanning for 500 cycles in the Faradaic region (~0.9-1.45 V, inset of Figure 4.15D). After the potential cycling, the current was found to be slightly enhanced (Appendix 4.6) which is likely due to the change in the electronic structure of the Ni-Co samples during the cycling. The change is most probably due to the increasing conversion of the metal nanoparticles, buried in the hydrophobic core of the IISERP-COF2 β (Appendix 4.8), into their hydroxides with time/cycling. In fact, all the catalysts (**1-5**) have displayed good stability with a minimal current loss, which suggests the IISERP-COF2 β backbone is aiding in this respect. The XPS analysis of the post OER samples showed retention of their pristine oxidation (M^{+2}) states of Nickel and Cobalt, other species like M^{+1} or M^0 (M=Co/Ni) were not observed (Appendix 4.10.). In order to verify the stability of the electrocatalyst under the operating conditions, we suspended the metal-loaded COFs (**1-5**) in a 0.1 M KOH solution for 24 hrs and subjected the dried solid extracted from the supernatant to an SEM-energy-dispersive X-ray analysis (EDAX). Absence of any metal (Co/Ni) components signal in the extract except for the potassium from the electrolyte, confirmed the lack of nanoparticle leaching (Appendix 4.9). The electrochemical stability was further substantiated from the highly reproducible redox activity of the catalyst even after 500 cycles and the onset and overpotential of the sample before and after such cycles remained unchanged (Appendix 4.6). These results confirm also the nonexistence of any kind of surface passivation.

4.6. Computational Modeling

To further investigate the nanoparticle-COF interactions, dispersion-corrected DFT modeling studies were carried out. Since microscopy studies (SEM and HR-TEM) suggested the existence of extremely thin hexagonal layers of metal nanoparticles, a 1.2 nm wide single hexagonal nano-sheet of Ni(OH)₂ was used as a model for the nanoparticles (Figure 4). The DFT-derived electrostatic potential fitted charges¹⁹ and Universal force field²⁰ were employed. The sheet was placed in different configurations within the IISERP-COF2 β (Figure 4.16). Three of the most stable optimized configurations were then fully optimized at the DFT level. Interestingly, the optimal configuration has the model nano-sheet sandwiched between the two adjacent sp³ nitrogen atoms of neighboring layers (Figure 4.16). Importantly, the lone pairs of the sp³ nitrogen (tripodal) centers are oriented toward the metal nano-sheets and it is possible that this interaction (sp³ N-Ni distance 3.96 Å) synergistically enhanced the electrocatalytic activity and durability of the metal nanoparticles during water-splitting reactions.

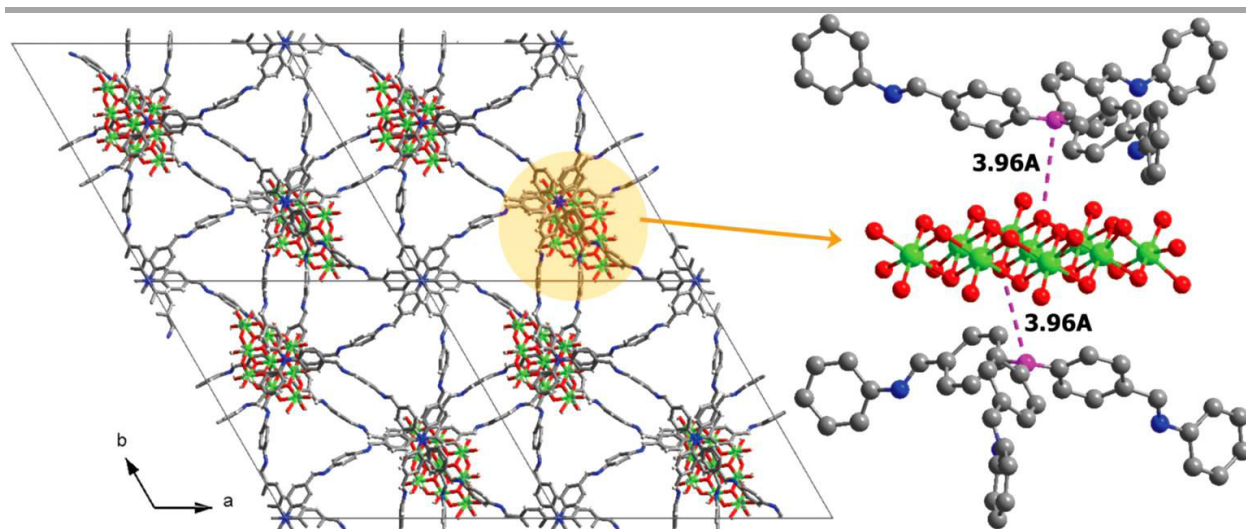


Figure 4.16. DFT geometry-optimized model structure of a Ni(OH)₂ sheet within IISERP-COF2. Left: View of the model looking onto the *ab*-plane. Right: Zoomed-in along the *bc*-plane.

4.7. Summary

Traditionally Schiff (C=N) base COFs have been made from rigid, planar aromatic building blocks that π -stack to form porous crystalline materials. In this work, we have shown that a COF composed of flexible (sp³ nitrogen rich) building blocks can act as a active support for noble-metal-free (Co/Ni) nanoparticles for electrocatalytic water splitting reactions.

Microscopy (HR-TEM and FE-SEM) studies revealed that the $\text{Co}_x\text{Ni}_y(\text{OH})_2$ nanoparticles are well dispersed within the framework composite with relatively few nanoparticles being found on the surface of the IISERP-COF2. Importantly, the growth of the nanoparticles within the IISERP-COF2 β is limited in size (2-3nm) with the majority of the nanoparticles being < 2 nm. The dispersion of the electrocatalyst as small-sized nanoparticles in the interlayer mesopores of the COF enables high access to the catalytic sites resulting in high performance characterized by a low overpotential ($\eta_{10} = 258$ V) with smooth kinetics (Tafel slope = 38.9 mV dec^{-1}) for the 4%Co:12%Ni@IISERP-COF2 β catalyst **5**. These values surpass most of the reported Ni/Co-based electrocatalyst in their supported as well as unsupported forms. Some of the composites involving highly conducting graphene as supports have a lower onset potential, but their overpotentials and kinetics are significantly poorer than the **5**. This is remarkable given that a four-probe measurement carried out on the pristine IISERP-COF2 β reveals that it is non-conducting in nature. This suggests that **5**'s exceptional electrocatalytic performance could be arising from some localized electronic interactions between the nanoparticles and the flexible sp^3 -nitrogen-rich COF framework. DFT modeling studies demonstrate the interaction between the hexagonal β -Ni(OH) $_2$ nanosheets and IISERP-COF2 β . The most favorable configuration of Ni(OH) $_2$ nanosheets are sandwiched between the tetrahedral sp^3 nitrogens of the adjacent IISERP-COF2 β layers, this filling is crucial to maximizing their synergistic interactions between np and COF for highly electrocatalytic activity.

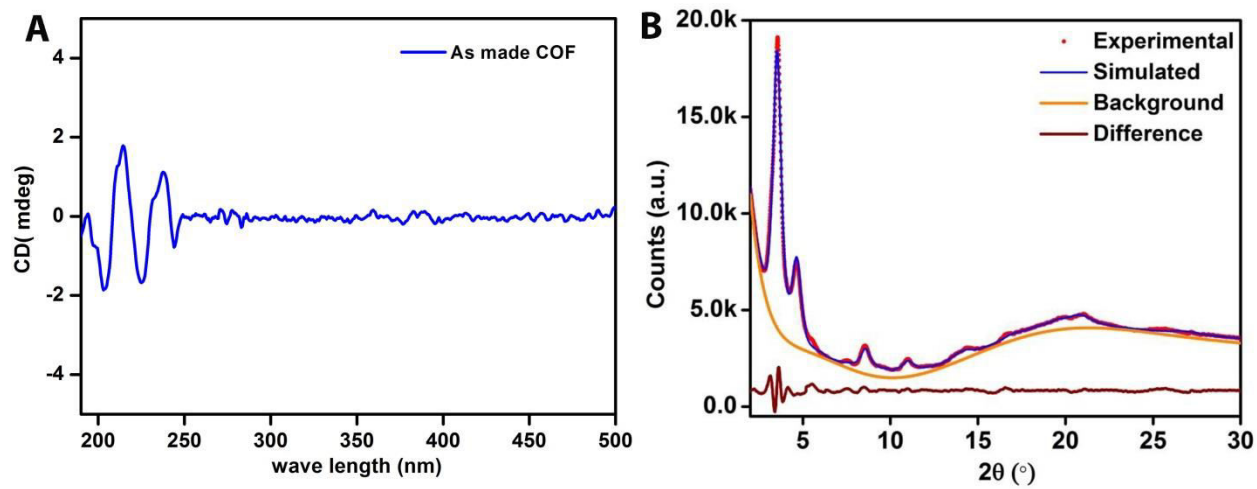
4.8. References

1. (a) Feng, X.; Ding, X.; Jiang, D. *Chem. Soc. Rev.* **2012**, *41*, 6010. (b) Feng, X.; Chen, L.; Honsho, Y.; Saengsawang, O.; Liu, L.; Wang, L.; Saeki, A.; Irle, S.; Seki, S.; Dong, Y.; Jiang, D. *Adv. Mater.* **2012**, *24*, 3026. (c) Colson, J. W.; Woll, A. R.; Mukherjee, A.; Levendorf, M. P.; Spitler, E. L.; Shields, V. B.; Spencer, M. G.; Park, J.; Dichtel, W. R. *Science* **2011**, *332*, 228. (d) Colson, J. W.; Dichtel, W. R. *Nat. Chem.* **2013**, *5*, 453. (e) Dalapati, S.; Jin, S.; Gao, J.; Xu, Y.; Nagai, A.; Jiang, D. *J. Am. Chem. Soc.* **2013**, *135*, 17310. (f) Dogru, M.; Bein, T. *Nat. Nanotechnol.* **2011**, *6*, 333. (g) Cote, A. P.; Benin, A. I.; Ockwig, N. W.; O'Keeffe, M.; Matzger, A. J.; Yaghi, O. M. *Science* **2005**, *310*, 1166. (h) Bertrand, G. H.; Michaelis, V. K.; Ong, T. C.; Griffin, R. G.; Dinca, M. *Proc. Natl. Acad. Sci. USA* **2013**, *110*, 4923. (i) Uribe-Romo, F. J.; Doonan, C. J.; Furukawa, H.;

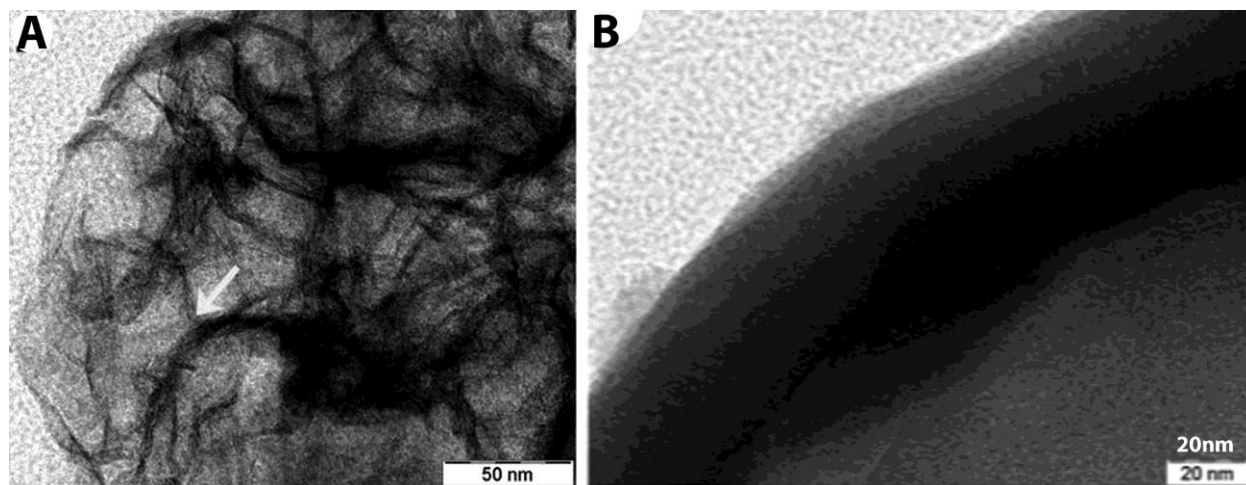
- Oisaki, K.; Yaghi, O. M. *J. Am. Chem. Soc.* **2011**, *133*, 11478. (j) Guo, J.; Xu, Y.; Jin, S.; Chen, L.; Kaji, T.; Honsho, Y.; Addicoat, M. A.; Kim, J.; Saeki, A.; Ihee, H.; Seki, S.; Irle, S.; Hiramoto, M.; Gao, J.; Jiang, D. *Nat. Commun.* **2013**, *4*, 2736. (k) Huang, N.; Krishna, R.; Jiang, D. *J. Am. Chem. Soc.* **2015**, *137*, 7079. (l) Dalapati, S.; Addicoat, M.; Jin, S.; Sakurai, T.; Gao, J.; Xu, H.; Irle, S.; Seki, S.; Jiang, D. *Nat. Commun.* **2015**, *6*, 7786. (m) Tilford, R. W.; Mugavero, S. J., 3rd; Pellechia, P. J.; Lavigne, J. J. *Adv. Mater.* **2008**, *20*, 2741. (n) Fang, Q.; Zhuang, Z.; Gu, S.; Kaspar, R. B.; Zheng, J.; Wang, J.; Qiu, S.; Yan, Y. *Nat. Commun.* **2014**, *5*, 4503. (o) Ben, T.; Ren, H.; Ma, S.; Cao, D.; Lan, J.; Jing, X.; Wang, W.; Xu, J.; Deng, F.; Simmons, J. M.; Qiu, S.; Zhu, G. *Angew. Chem. Int. Ed.* **2009**, *48*, 9457.
2. Kamiya, K.; Kamai, R.; Hashimoto, K.; Nakanishi, S. *Nat. Commun.* **2014**, *5*, 5040.
 3. Ding, X.; Guo, J.; Feng, X.; Honsho, Y.; Guo, J.; Seki, S.; Maitarad, P.; Saeki, A.; Nagase, S.; Jiang, D. *Angew. Chem. Int. Ed.* **2011**, *50*, 1289.
 4. Chandra, S.; Kundu, T.; Kandambeth, S.; Babarao, R.; Marathe, Y.; Kunjir, S. M.; Banerjee, R. *J. Am. Chem. Soc.* **2014**, *136*, 6570.
 5. Vyas, V. S.; Haase, F.; Stegbauer, L.; Savasci, G.; Podjaski, F.; Ochsenfeld, C.; Lotsch, B. V. *Nat. Commun.* **2015**, *6*, 9508
 6. Oh, H.; Kalidindi, S. B.; Um, Y.; Bureekaew, S.; Schmid, R.; Fischer, R. A.; Hirscher, M., A. *Angew. Chem. Int. Ed.* **2013**, *52*, 13219.
 7. Das, G.; Biswal, B. P.; Kandambeth, S.; Venkatesh, V.; Kaur, G.; Addicoat, M.; Heine, T.; Verma, S.; Banerjee, R. *Chem. Sci.* **2015**, *6*, 3931.
 8. Furukawa, H.; Yaghi, O. M. *J. Am. Chem. Soc.* **2009**, *131*, 8875.
 9. Ding, S. Y.; Gao, J.; Wang, Q.; Zhang, Y.; Song, W. G.; Su, C. Y.; Wang, W. *J. Am. Chem. Soc.* **2011**, *133*, 19816.
 10. Kalidindi, S. B.; Fischer, R. A. *Phys. Status Solidi B* **2013**, *250*, 1119. (a) Xu, F.; Jin, S.; Zhong, H.; Wu, D.; Yang, X.; Chen, X.; Wei, H.; Fu, R.; Jiang, D. *Sci. Rep.* **2015**, *5*, 8225. (b) Pachfule, P.; Kandambeth, S.; Diaz Diaz, D.; Banerjee, R. *Chem. Commun.* **2014**, *50*, 3169. (c) Chan-Thaw, C. E.; Villa, A.; Katekomol, P.; Su, D.; Thomas, A.; Prati, L. *Nano Lett.* **2010**, *10*, 537; (d) Mullangi, D.; Nandi, S.; Shalini, S.; Sreedhala, S.; Vinod, C. P.; Vaidhyanathan, R. *Sci. Rep.* **2015**, *5*, 10876

11. Smith, R. D.; Prevot, M. S.; Fagan, R. D.; Zhang, Z.; Sedach, P. A.; Siu, M. K.; Trudel, S.; Berlinguette, C. P. *Science* **2013**, *340*, 60.
12. Wang, G.; Zhang, X.; Geng, J.; Li, K.; Ding, D.; Pu, K-Y.; Cai, L.; Lai, Y-H.; Liu, B.; *Chem. Eur. J.* **2012**, *18*, 9705-9713.
13. Dhavale, V. M.; Gaikwad, S. S.; George, L.; Devi, R. N.; Kurungot, S. *Nanoscale* **2014**, *6*, 13179.
14. (a) Lu, X.; Zhao, C. *Nat. Commun.* **2015**, *6*, 6616. (b) Lee, J. S.; Park, G. S.; Kim, S. T.; Liu, M.; Cho, J. *Angew. Chem. Int. Ed.* **2013**, *52*, 1026.
15. Li, L.; Xu, J.; Lei, J.; Zhang, J.; McLarnon, F.; Wei, Z.; Lic, N. ; Pand, F. *J. Mater. Chem. A* **2015**, *3*, 1953.
16. Gong, M.; Li, Y.; Wang, H.; Liang, Y.; Wu, J. Z.; Zhou, J.; Wang, J.; Regier, T.; Wei, F.; Dai, H. *J. Am. Chem. Soc.* **2013**, *135*, 8452.
17. Fominykh, K.; Feckl, J. M.; Sicklinger, J.; Döblinger, M.; Böcklein, S.; Ziegler, J.; Peter, L.; Rathousky, J.; Scheidt, E.-W.; Bein, T.; Fattakhova-Rohlfing, D. *Adv. Funct. Mater.* **2014**, *24*, 3123.
18. Trotochaud, L.; Ranney, J. K.; Williams, K. N.; Boettcher, S. W. *J. Am. Chem. Soc.* **2012**, *134*, 17253.
19. Kresse, G.; Joubert, D. *Phys. Rev. B* **1999**, *59*, 1758.
20. Rappe, A. K.; Casewit, C. J.; Colwell, K. S.; Goddard, W. A.; Skiff, W. M. *J. Am. Chem. Soc.* **1992**, *114*, 10024.

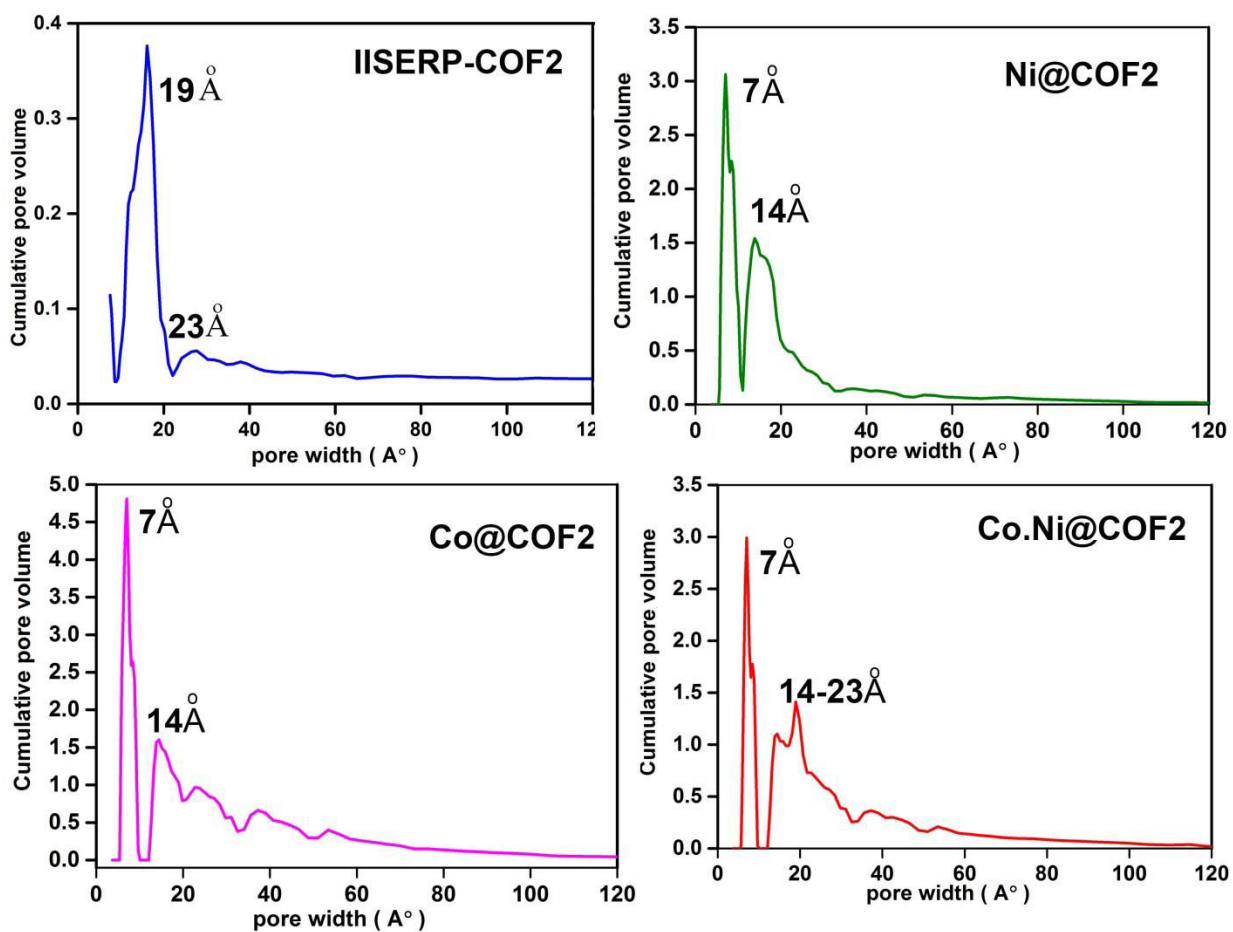
Chapter-4 Appendix



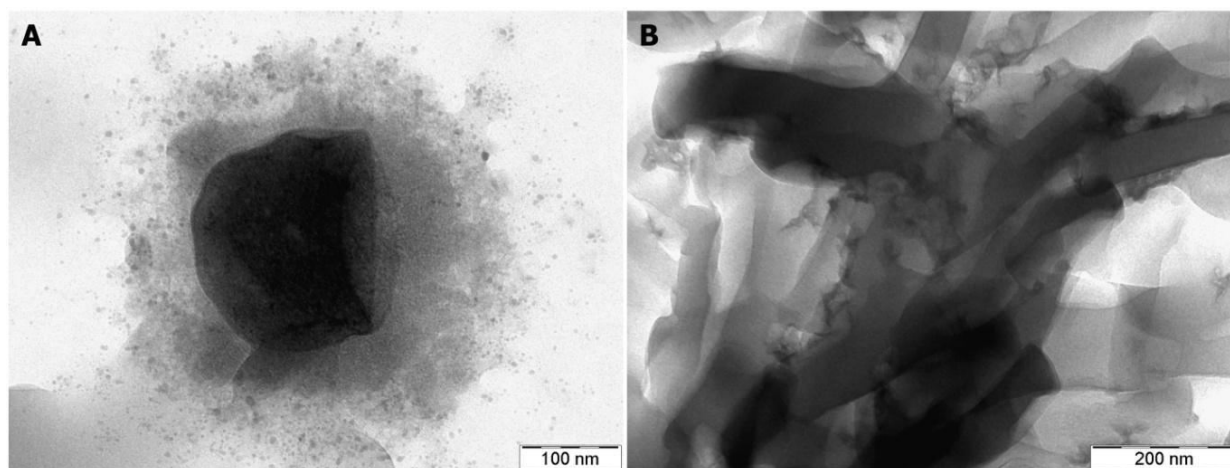
Appendix 4.1. (A) Circular dichroism (CD) spectra of IISERP-COF2 β recorded using a pelletized solid (B) IISERP-COF2 β Le bail fit obtained in P6₃ space group with unit cell $a = b = 29.17$ (21); $c = 29.31(17)$ Å, and GOF Rp = 0.0287, wRp = 0.0439, Dwd = 0.014, $\chi^2 = 1.372$.



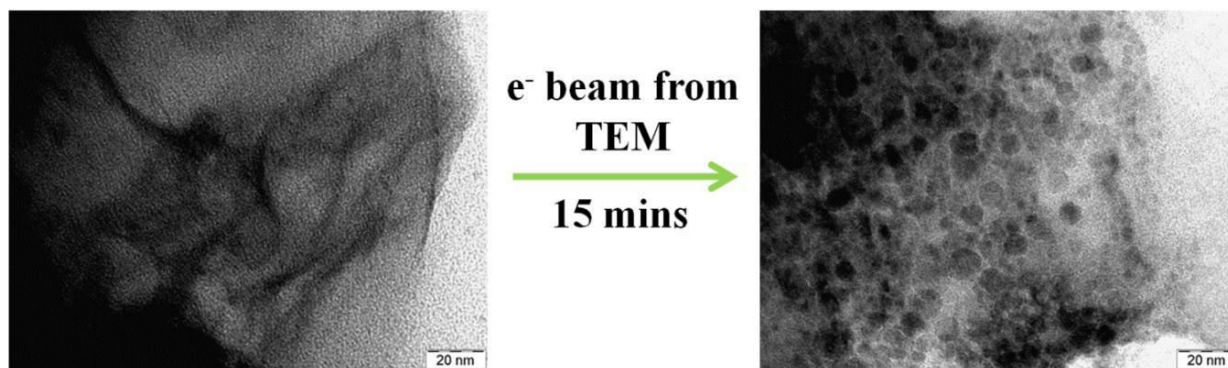
Appendix 4.2. (A) Graphene-like morphology (B) A zoom-in into the edges of the figure.2B (region circled yellow).



Appendix 4.3. Pore sizes distribution of metal loaded COFs(1-3) and as made IISERP-COF2.



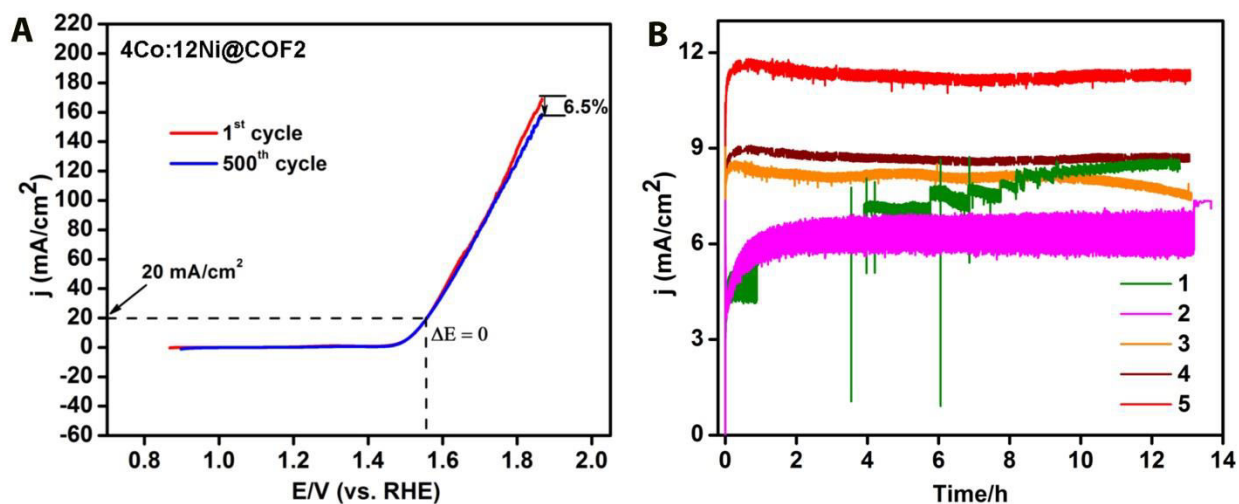
Appendix 4.4 HR-TEM images used for particle size calculation.



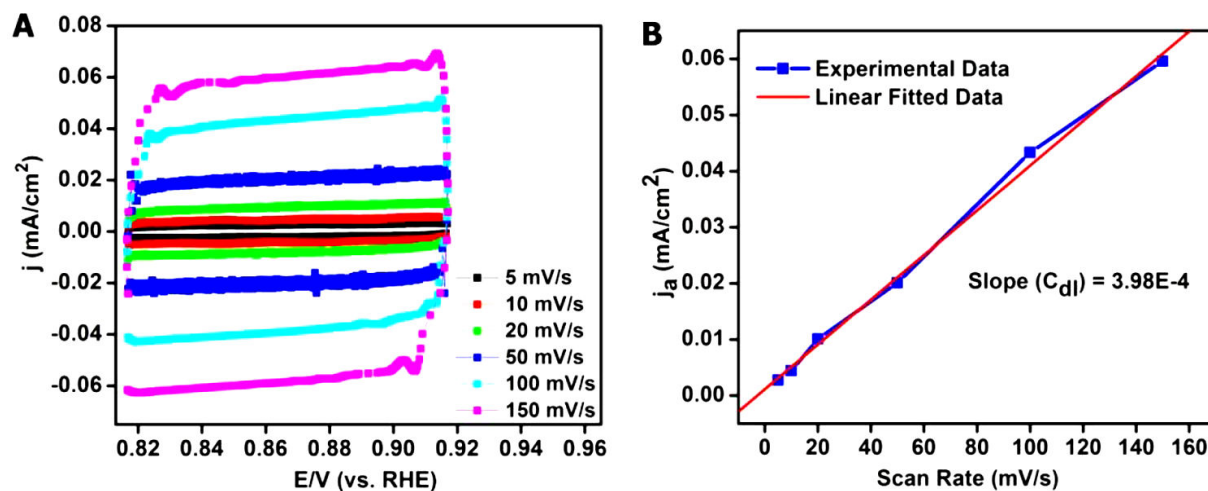
Appendix 4.5. HR-TEM image of metal loaded COF before and after annealing under TEM.

Electrocatalysts	Onset Potential [V] vs. RHE	Conc. of KOH [M]	Overpotential [mV] at 10 mA/cm ²	Tafel Slope [mV/dec]	Reference
16Ni-COF [1]	1.5463	0.1	402.3	89.3	Our work
16Co-COF [2]	1.5603	0.1	487.3	91.4	Our work
8Co:8Ni-COF [3]	1.5011	0.1	315.8	64.1	Our work
12Co:4Ni-COF [4]	1.4683	0.1	399.8	86.3	Our work
4Co:12Ni-COF [5]	1.430	0.1	258.0	38.9	Our work
Co(OH) ₂ nps	1.5	0.1	--	61	<i>ACS AMI</i> 2014 ,6,10172
Ni(OH) ₂ nps	1.54	0.1	444	111	<i>JACS</i> , 2014 ,136,707077
Ni-Co 3DNNCNTAs	1.5453	0.1	460	65	<i>AFM</i> 2014 ,24, 4698
Porous N-doped Graphene NiCo ₂ O ₄ [PNG-NiCo]	1.548	0.1	~438.3	156	<i>ACS Nano</i> 2013 , 7, 10190
NiCo ₂ S ₄ /Graphene	~1.5083	0.1	470	--	<i>ACS AMI</i> , 2013 ,5,5002
NiCo ₂ O ₄ /Graphene	1.6511	0.1	--	205	<i>JMCA</i> 2013 , 1, 4754 .
NiCo-oxide Hollow Nano Sponge	1.501	0.1	~362	64.4	<i>Chem. Comm.</i> , 2015 , 51, 7851.

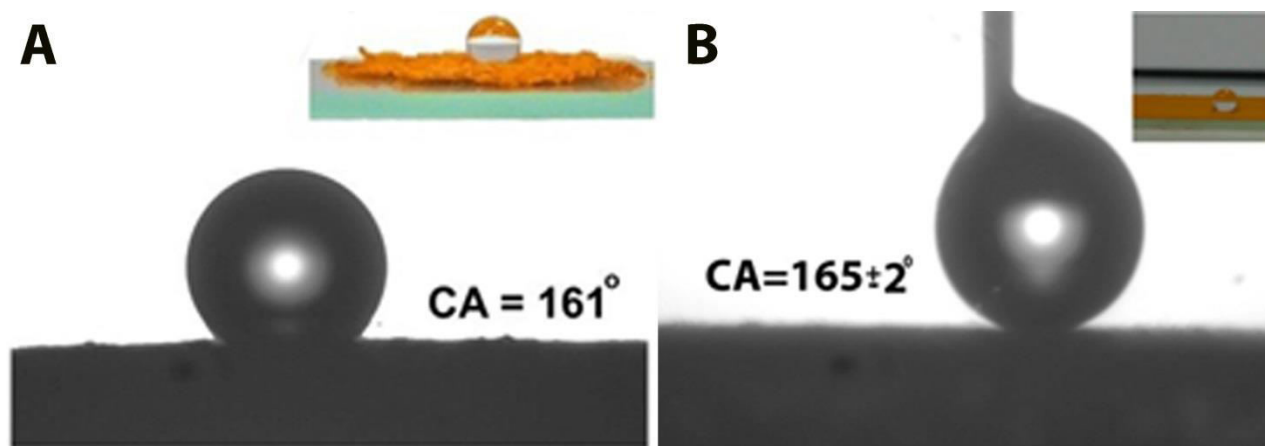
Table 4.1. Comparison of our Oxygen Evolution Reactions (OER) results with recent literature.



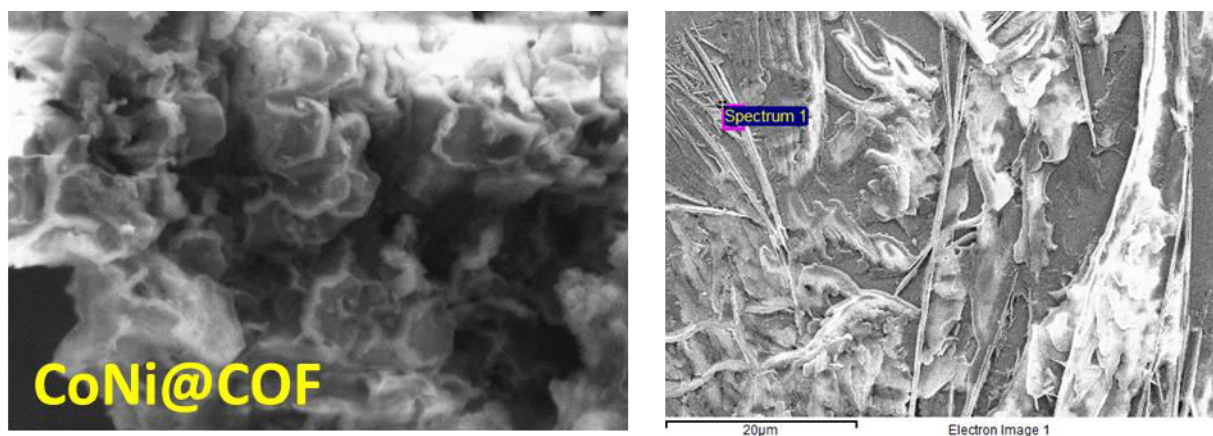
Appendix 4.6. (A) Oxygen evolution curve of **5** before and after 500 cycles (B) Chronoamperometry plots (recorded at 1600 rpm) for the all samples (**1-5**) showing their excellent stability in their current outputs over 13 hrs.



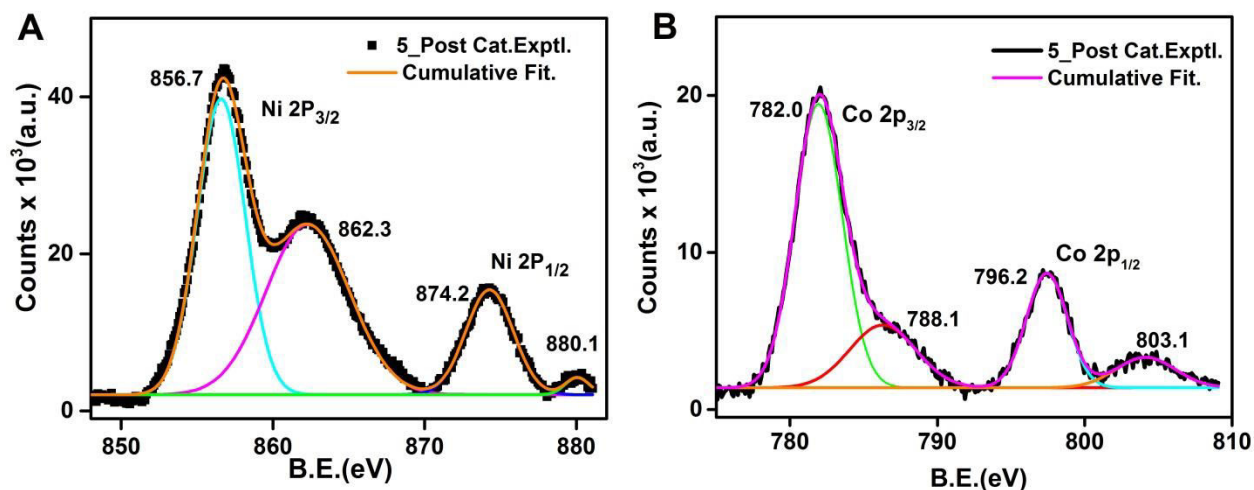
Appendix 4.7. (A) Non-Faradaic Cyclic voltammograms (CV) of **5**. (B) Anodic current density vs scan rate plotted from the non-Faradaic CV data.



Appendix 4.8. (A) Contact angle angle (B) Static Contact angle angles of IISERP-COF2 β .



Appendix 4.9. SEM-EDX images of supernatant solution of the post catalyst(5).



Appendix 4.10. XPS data of the post OER catalysis sample showing the retention of the pristine oxidation (M+2) states of Nickel and Cobalt in the sample 5.

Copyrights from the references used in the thesis

2/16/2019 Rightslink® by Copyright Clearance Center

Copyright Clearance Center
 ACS Publications
 Most Trusted. Most Cited. Most Read.

Title: Construction of Covalent Organic Framework for Catalysis: Pd/COF-LZU1 in Suzuki-Miyaura Coupling Reaction
Author: San-Yuan Ding, Jia Gao, Qiong Wang, et al
Publication: Journal of the American Chemical Society
Publisher: American Chemical Society
Date: Dec 1, 2011
 Copyright © 2011, American Chemical Society

LOGIN
 If you're a copyright.com user, you can login to Rightslink using your copyright.com credentials. Already a RightsLink user or want to learn more?

PERMISSION/LICENSE IS GRANTED FOR YOUR ORDER AT NO CHARGE
 This type of permission/license, instead of the standard Terms & Conditions, is sent to you because no fee is being charged for your order. Please note the following:

Ding, S. Y.; Gao, J.; Wang, Q.; Zhang, Y.; Song, W. G.; Su, C. Y.; Wang, W. *J. Am. Chem. Soc.* **2011**, *133*, 19816-22.

2/22/2019 Copyright Clearance Center

Welcome | Log in | Cart (0) | Manage Account | Feedback | Help | Live Help

Get Permission / Find Title
 Publication Title or ISBN/ISSN
 Advanced Search Options

Journal of materials chemistry. A, Materials for energy and sustainability
ISSN: 2050-7496
Publication year(s): 2013 - present
Author/Editor: Royal Society of Chemistry (Great Britain)
Publication type: e-Journal
Publisher: Royal Society of Chemistry
Rightsholder: ROYAL SOCIETY OF CHEMISTRY

Language: English
Country of publication: United Kingdom of Great Britain and Northern Ireland

Permission type selected: Republish or display content
Type of use selected: Thesis/Dissertation

Pachfule, P.; Panda, M. K.; Kandambeth, S.; Shivaprasad, S. M.; Díaz, D. D.; Banerjee, R. *J. Mater. Chem. A* **2014**, *2*, 7944-7952

2/22/2019 Rightslink® by Copyright Clearance Center

Copyright Clearance Center
 RightsLink®

Home Create Account Help

LOGIN
 If you're a copyright.com user, you can login to Rightslink using your copyright.com credentials. Already a RightsLink user or want to learn more?

Title: Catalysis and CO2 Capture by Palladium-Incorporated Covalent Organic Frameworks
Author: Dhananjayan Kaleeswaran, Rajendran Antony, Abhishek Sharma, et al
Publication: CHEMPLUSCHEM
Publisher: John Wiley and Sons
Date: Oct 9, 2017
 © WILEY-VCH Verlag GmbH & Co. KGaA, Weinheim



Kaleeswaran, D.; Antony, R.; Sharma, A.; Malani, A.; Murugavel, R. *ChemPlusChem* **2017**, *82*, 1253 – 1265.

Materials Chemistry Frontiers

ISSN: 2052-1537
Publication year(s): 2016 - present
Author/Editor: Royal Society of Chemistry (Great Britain) ; Zhongguo hua xue hui (Beijing, China)

Publication type: e-Journal
Publisher: Royal Society of Chemistry

Rightholder: ROYAL SOCIETY OF CHEMISTRY

Language: English
Country of publication: United Kingdom of Great Britain and Northern Ireland

Permission type selected: Republish or display content

Type of use selected: Thesis/Dissertation

Sun, Q.; Aguila, B.; Ma, S. *Mater. Chem. Front.*, **2017**, 1, 1310.

2/22/2019 Rightslink® by Copyright Clearance Center



Home Create Account Help

ACS Publications Title: Predesigned Metal-Anchored Building Block for In Situ Generation of Pd Nanoparticles in Porous Covalent Organic Framework: Application in Heterogeneous Tandem Catalysis

Author: Mohitosh Bhadra, Himadri Sekhar Sasmal, Arghya Basu, et al

Publication: Applied Materials

Publisher: American Chemical Society

Date: Apr 1, 2017

Copyright © 2017, American Chemical Society

LOGIN

If you're a [copyright.com](#) user, you can login to RightsLink using your [copyright.com](#) credentials. Already a [RightsLink user](#) or want to [learn more?](#)

PERMISSION/LICENSE IS GRANTED FOR YOUR ORDER AT NO CHARGE

This type of permission/license, instead of the standard Terms & Conditions, is sent to you because no fee is being charged for your order. Please note the following:

Bhadra, M.; Sasmal, H. S.; Basu, A.; Midya, S. P.; Kandambeth, S.; Pachfule, P.; Balaraman, E.; Banerjee, R. *ACS Appl. Mater. Interfaces* **2017**, 9, 13785-13792.

2/22/2019 Rightslink® by Copyright Clearance Center



Home Create Account Help

ACS Publications Title: Synthesis of Ultrafine and Highly Dispersed Metal Nanoparticles Confined in a Thioether-Containing Covalent Organic Framework and Their Catalytic Applications

Author: Shuanglong Lu, Yiming Hu, Shun Wan, et al

Publication: Journal of the American Chemical Society

Publisher: American Chemical Society

Date: Nov 1, 2017

Copyright © 2017, American Chemical Society

LOGIN

If you're a [copyright.com](#) user, you can login to RightsLink using your [copyright.com](#) credentials. Already a [RightsLink user](#) or want to [learn more?](#)

PERMISSION/LICENSE IS GRANTED FOR YOUR ORDER AT NO CHARGE

This type of permission/license, instead of the standard Terms & Conditions, is sent to you because no fee is being charged for your order. Please note the following:

Lu, S.; Hu, Y.; Wan, S.; McCaffrey, R.; Jin, Y.; Gu, H.; Zhang, W. *J. Am. Chem. Soc.* **2017**, 139, 17082-17088

2/22/2019 Copyright Clearance Center

Welcome | Log in | Cart (0) | Manage Account | Feedback | Help | Live Help

Get Permission / Find Title
 Publication Title or ISBN/ISSN Go
 Advanced Search Options

Journal of materials chemistry. A, Materials for energy and sustainability

ISSN:	2050-7496	Language:	English
Publication year(s):	2013 - present	Country of publication:	United Kingdom of Great Britain and Northern Ireland
Author/Editor:	Royal Society of Chemistry (Great Britain)		
Publication type:	e-Journal		
Publisher:	Royal Society of Chemistry		

Rightsholder: ROYAL SOCIETY OF CHEMISTRY

Permission type selected: Republish or display content
Type of use selected: Thesis/Dissertation

Pachfule, P.; Kandambeth, S.; Diaz, D.; Banerjee, R. *Chem. Comm.* **2014**, *50*, 3169-72.


Attribution 3.0 Unported (CC BY 3.0)

This is a human-readable summary of (and not a substitute for) the [license](#). [Disclaimer](#).

You are free to:

- Share** — copy and redistribute the material in any medium or format
- Adapt** — remix, transform, and build upon the material for any purpose, even commercially.

The licensor cannot revoke these freedoms as long as you follow the license terms.



Chen, L.; Zhang, L.; Chen, Z.; Liu, H.; Luque, R.; Li, Y. *Chem. Sci.* **2016**, *7*, 6015-6020

2/22/2019 Rightslink® by Copyright Clearance Center

Copyright Clearance Center **RightsLink®** Home Create Account Help



Title: Low Band Gap Benzimidazole COF Supported Ni3N as Highly Active OER Catalyst

Author: Shyamapada Nandi, Santosh Kumar Singh, Dinesh Mullangi, Rajith Illathvalappil, Leena George, Chathakudath P. Vinod, Sree Kumar Kurungot, Ramanathan Vaidhyanathan

Publication: Advanced Energy Materials
Publisher: John Wiley and Sons
Date: Aug 29, 2016
Copyright © 2016, John Wiley and Sons

LOGIN

If you're a [copyright.com](#) user, you can login to RightsLink using your [copyright.com](#) credentials. Already a [RightsLink user](#) or want to [learn more?](#)

Quick Price Estimate

Please review the credit line for the requested figure/table. If the figure/table you wish to reproduce is credited to a source other than the author of the publication (i.e third party material) you will need to obtain permission from that copyright holder, book or journal before making any use of the material. For the avoidance of doubt – any and all third party content is expressly excluded from this permission. Otherwise please proceed with your order.

John Wiley and Sons grants a license for all orders, including \$0 orders. Please select the Continue button and place an order for this reuse.

Nandi, S.; Singh, S. K.; Mullangi, D.; Illathvalappil, R.; George, L.; Vinod, C. P.; Kurungot, S.; Vaidhyanathan, R. *Adv. Energy Mater.* **2016**, *6*, 1601189.

2/22/2019

Rightslink® by Copyright Clearance Center



RightsLink®



Title: Low-Overpotential Electrocatalytic Water Splitting with Noble-Metal-Free Nanoparticles Supported in a sp³ N-Rich Flexible COF

Author: Dinesh Mullangi, Vishal Dhavale, Sorout Shalini, Shyamapada Nandi, Sean Collins, Tom Woo, Sreekumar Kurungot, Ramanathan Vaidhyanathan

Publication: Advanced Energy Materials

Publisher: John Wiley and Sons

Date: May 2, 2016

Copyright © 2016, John Wiley and Sons

LOGIN

If you're a copyright.com user, you can login to RightsLink using your copyright.com credentials. Already a RightsLink user or want to [learn more?](#)

Quick Price Estimate

John Wiley and Sons grants a license for all orders, including \$0 orders. Please select the Continue button and place an order for this reuse.

Mullangi, D.; Dhavale, V.; Shalini, S.; Nandi, S.; Collins, S.; Woo, T.; Kurungot, S.; Vaidhyanathan, R. *Adv. Energy Mater.* **2016**, *6*, 1600110

2/22/2019

Rightslink® by Copyright Clearance Center



RightsLink®



Title: Highly Stable COF-Supported Co/Co(OH)₂ Nanoparticles Heterogeneous Catalyst for Reduction of Nitrile/Nitro Compounds under Mild Conditions

Author: Dinesh Mullangi, Debanjan Chakraborty, Anu Pradeep, et al

Publication: Small

Publisher: John Wiley and Sons

Date: Jul 30, 2018

© WILEY-VCH Verlag GmbH & Co. KGaA, Weinheim

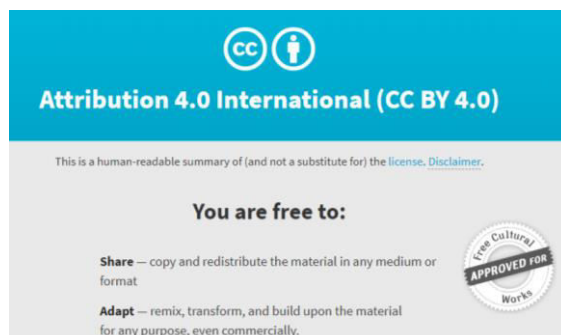
LOGIN

If you're a copyright.com user, you can login to RightsLink using your copyright.com credentials. Already a RightsLink user or want to [learn more?](#)

Quick Price Estimate

John Wiley and Sons grants a license for all orders, including \$0 orders. Please select the Continue button and place an order for this reuse.

Mullangi, D.; Chakraborty, D.; Pradeep, A.; Koshti, V.; Vinod, C. P.; Panja, S.; Nair, S.; Vaidhyanathan, R. *Small*, **2018**, 1801233.



Mullangi, D.; Nandi, S.; Shalini, S.; Sreedhala, S.; Vinod, C. P.; Vaidhyanathan, R. *Sci. Rep.* **2015**, *5*, 10876.